Dissertation
submitted to the
Combined Faculty of Natural Sciences and Mathematics
of Heidelberg University, Germany
for the degree of
Doctor of Natural Sciences

Put forward by
Anastasiia Filimonova
born in: Kyiv, Ukraine
Oral examination: 8.07.2020

Reviving the thermal dark matter paradigm with long-lived particles

Referees: Jun.-Prof. Dr. Susanne Westhoff
Prof. Dr. Joerg Jaeckel

Abstract

The nature of dark matter is one of the most crucial open questions of modern fundamental physics. In this thesis, we aim to address this problem, focusing on minimal dark sector models that can be falsified with current experimental techniques.

First, we study an effective theory of Higgs portal dark matter at the electroweak mass scale. We notice an almost unstudied mechanism of thermal dark matter production, the co-scattering mechanism, that is a general characteristic of models with extended dark sectors.

Second, we connect the viable thermal dark sector theories with the corresponding collider signatures. We find that such sectors feature compressed mass spectra, resulting in long-lived mediators at colliders. We perform a comprehensive study of possible displaced signatures in the singlet-triplet Higgs portal model and find a remarkable potential of displaced searches in testing dark matter theories where traditional techniques fail.

Finally, we extend our focus by exploring the prospects of long-lived particle searches at e^+e^- colliders. We predict the sensitivity of Belle II to displaced objects in rare meson decays, showing its ability to compete even with some of the long-baseline experiments.

Zusammenfassung

Die Natur dunkler Materie ist eine der wichtigsten ungelösten Fragen der modernen Grundlagenphysik. In dieser Thesis werden mögliche Erklaerungen für dieses Problem durch Modelle minimaler dunkler Sektoren aufgezeigt, welche mit aktuellen experimentellen Methoden getestet werden können.

Wir untersuchen zunächst eine effektive Theorie von dunkler Materie mit einem Higgsportal an der elektroschwachen Massenskala. Wir analysieren einen wenig erforschten Mechanismus für die thermische Produktion von dunkler Materie, den Co-Streuungsmechanismus, welcher eine generelle Eigenschaft von Modellen mit erweiterten dunklen Sektoren darstellt.

Desweiteren untersuchen wir die möglichen Signaturen von Theorien thermaler dunkler Sektoren an Beschleunigern. Wir stellen fest, dass solche Sektoren notwendingerweise komprimierte Massenspektren aufweisen, welche in langlebigen Austauschteilchen resultieren. Wir führen eine umfassende Untersuchung der Signaturen mit versetzten Zerfallspunkten im Singulett-Triplett Higgsportalmodell durch. Wir finden heraus, dass diese Signaturen dort ein bemerkenswertes Potential haben, Theorien dunkler Materie zu testen, wo traditionelle Suchen scheitern.

Schliesslich erweitern wir unsere Analyse auf die Untersuchung der Sensitivität von e+e-Beschleunigern fuer die Suche nach langlebigen Teilchen. Wir bestimmen die Sensitivität des Belle II Experiments auf Objekte mit versetzten Zerfallspunkten in seltenen Mesonzerfällen und zeigen, dass diese mit der Empfindlichkeit von Experimenten mit langen Basislinien konkurrieren kann.

Contents

Preface

The research presented in this thesis was conducted at the Institute for Theoretical Physics at Heidelberg University from August 2017 to May 2020. The contents of Chapters 4 and 5 are based on work in collaboration with other authors and have previously been published as

[1] A. Filimonova and S. Westhoff, "Long live the Higgs portal!" *JHEP*, vol. 02, p. 140, 2019. DOI: 10.1007/JHEP02(2019)140. arXiv: 1812.04628 [hep-ph].

[2] A. Filimonova, R. Schäfer, and S. Westhoff, "Probing dark sectors with long-lived particles at BELLE II," 2019. arXiv: 1911.03490 [hep-ph].

The author is also involved in ongoing research, which has not been published at the time of writing this thesis.

1. Introduction

The phenomenon of missing mass is already known in astronomy for over a century. It was discussed already in 1904 by Lord Kelvin [1] who estimated the number of dark bodies in the Milky Way based on the velocity dispersion of stars in our galaxy. The term "dark matter" was first introduced by Henri Poincaré in 1906 [2], and became commonly used after the Fritz Zwicky's discovery [3] of the missing mass needed to hold together the Coma Cluster. Since then, many indications of massive non-interacting with light matter were found. The distinct feature of this new type of matter is that it behaves as "collision-less fluid" at such a wide range of scales, that the description of all the observed effects at once becomes extremely challenging without adding a highly non-relativistic matter field – a new particle. On the other hand, the Standard Model of particle physics, being tested in a plethora of ways, describes experimental data with tremendous precision [4]. Therefore, a fundamental theory of dark matter, together with explanations of neutrino oscillations and baryon asymmetry of the Universe, is among the biggest mysteries of particle physics nowadays.

The overwhelming amount of astrophysical and cosmological indications of dark matter, combined with null results at all particle physics experiments that search for new states results in beautiful and terrifying diversity of proposed fundamental dark matter theories. After years of steadily excluding the most simple or aesthetically appealing of them, model builders are forced to look for sophisticated tricks to match the experimental outcome. The difficulty of probing the predicted individual signatures at colliders creates a necessity for a more comprehensive theoretical approach that operates not by individual theories, but by classes of models. This is the approach we follow in Chapters 4 and 5, working with simplified and effective field theories and predicting signatures that can be reinterpreted in a wide range of dark matter models.

The absence of experimental evidence of particles beyond the Standard Model may also be caused by the underlying physics assumptions of experimental setup when searching for new physics. In Chapter 3, we discuss such an issue in the context of thermal (or "WIMP-like") dark matter that is frequently considered to be ruled-out. We find that a huge and probably one of the most phenomenologically motivated classes of thermal dark matter models are undetectable with the strategies currently used in dark matter searches at the LHC.

1.1. Observational evidence of dark matter

Even though the necessity of introducing a new particle to explain all the observed missing mass phenomena is generally accepted, it is very important to emphasize the range of independent sources and scales at which non-luminous, or *dark matter* (DM), is observed. Thus, let us briefly discuss the main astrophysical and cosmological observations which, combined, lead to the current image of a "DM candidate".

Astrophysical observation of galaxy rotation curves

The Doppler shift of emission/absorption lines allows astronomers to detect the distribution of velocity along the line of sight in large enough objects [5]. Applying this method to very flat spiral galaxies allows resolving the full rotational speed $V(r)$ at a certain radius r from the galaxy center. From Newtonian gravity, the stars' motion inside galaxies should be defined solely by the galaxy mass enclosed within a sphere of the radius considered. This means that at the galaxy outskirts, where the enclosed mass is constant, the velocity dependence on the radius is

$$V(r) = \sqrt{\frac{GM}{r}}. \tag{1.1}$$

Here M is the enclosed mass and G is the Newton constant. The $V(r)$ dependence is also referred to as *the galaxy rotation curve*.

Most of the observed rotation curves, however, do not show a $1/\sqrt{r}$ dependence, many of them grow with radius and flatten at large r.

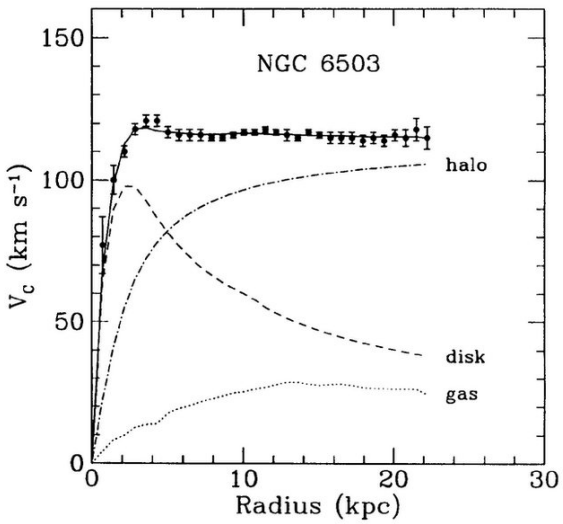

Figure 1.1: Galaxy rotation curve of the NGC 6503 galaxy: experimental data (error bars) matches the theory predictions if the contribution from gas, ordinary matter (marked as "disk") and DM (marked as "halo") are taken into account [6].

Such an effect may be caused by the presence in the galaxy of invisible ("dark") objects, distributed differently than the observed matter. For example, the flat profile of NGC 6503 galaxy shown in Figure 1.1, infers that the total mass of the galaxy behaves as $M(r) \propto r$. In

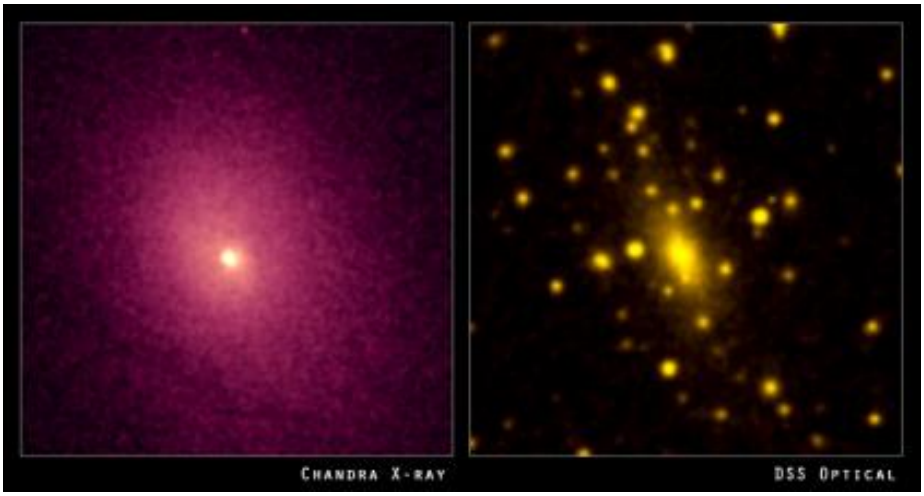

Figure 1.2: The Abell 2029 galaxy cluster in the X-ray (left) and optical (right) light. Credit: X-ray: NASA/CXC/UCI/A.Lewis et al. Optical: Pal.Obs. DSS

terms of the total density distribution, the corresponding dependence is[1] $\rho \propto 1/r^2$. Moreover, to explain the observed velocities, this additional component typically has to dominate the galaxy's mass and extend far beyond the observed matter. For example, the luminous mass (radius) of the Milky Way Galaxy is approximately $9 \times 10^{10} M_\odot$, whereas the total mass makes up $10^{12} M_\odot$ [7].

Astrophysical observation of the Milky Way's dwarf spheroidal satellites

Dwarf spheroidal satellites are the objects with the largest mass-to-light ratios known. The density profiles of such objects are inferred from the high-precision spectroscopic velocities of bright individual stars [8] and by applying Jeans analysis [9]. Since the full 3D velocities cannot be reconstructed and assumptions about the velocity anisotropy profile have to be made, the resulting density profiles come out with large uncertainties. Typically, the observed mass-to-light ratios of such objects are of the order of $M/L \sim 10[M/L]_\odot$, where L is the satellite's luminosity, reaching in some cases $M/L > 100[M/L]_\odot$ [10].

Astrophysical measurements of gas temperature

This evidence comes from the determination of gas temperature in astrophysical objects based on their X-ray thermal emission and is commonly applied to elliptic galaxies and the intergalactic medium of galaxy clusters (see Figure 1.2). Due to local thermal equilibrium, the temperature and the total mass distributions of matter inside these objects can be connected via hydrostatic equilibrium equation [11]. Together with the observed luminous mass distribution, they provide detailed information about the mass-to-light ratios of these objects, which result in up to 95% (85%) of DM component in some elliptic galaxies [11] (galaxy clusters [12, 13]).

[1] Here we simplified the calculations assuming spherically-symmetric DM halo.

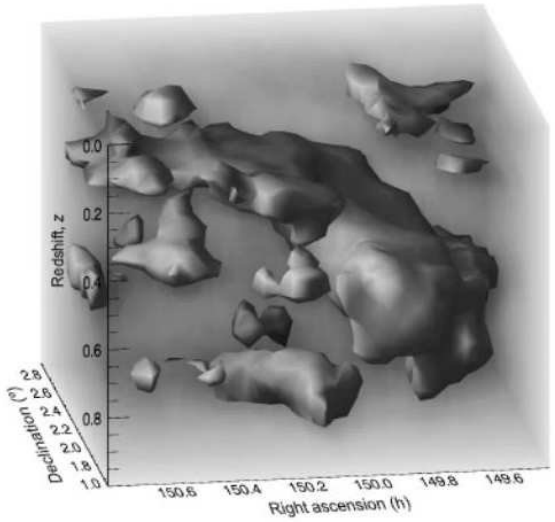

Figure 1.3: The 3D DM distribution obtained by the "redshift slicing" of sources using the Hubble Space Telescope data [14].

Astrophysical observation of gravitational lensing

When light, emitted by a distant source, passes by a massive object, it bends. Hence, the mass located between the source and the observer acts as a focus lens. Observations of the light from very bright distant objects (e.g. quasars), allows reconstructing matter distribution along the line of sight. Consequently, comparing it to the observed luminous matter allows finding the distribution of the non-visible matter. In some cases, it is even possible to reconstruct the 3D DM map by splitting the source galaxies into redshift bins, see Figure 1.3.

Depending on the strength of the lens, the light source can be seen as a slightly elongated object, an arch, an Einstein ring, or even as multiple images (as an example, see Figure 1.4). In the case of very weak lensing, the ellipticity change of individual objects is smaller than the typical variation between galaxies. The lensing effect, however, can still be extracted statistically. If the lensing is so strong that multiple images are formed, the observed objects are associated with the same initial source by comparing their spectra [14].

Figure 1.4: An example of a lensed picture of Abel 2218 galaxy cluster. Due to a large amount of mass concentrated, visible galaxies are become elongated or create arches.
Credit: Hubble Space Telescope & NASA

Astrophysical observation of galaxy clusters' collisions

As discussed above, galaxy clusters contain both visible and invisible matter which behave extremely differently in collision events, see Figure 1.5.

The effect of spatial separation of gravitational and visible matter in colliding systems speaks strongly in favor of the particle nature of DM (as opposed to modified gravity theories). Visible matter, composed mostly of gas and seen in X-rays, is slowed down in the region of collision due to friction forces. We can also observe shock waves caused by the collision. In contrast, the mass of these objects, deduced from gravitational lensing, is concentrated in two separate regions, distanced from the collision area. The observed picture indicates that the two DM halos passed through each other without significant interaction, pointing to the predominantly collisionless nature of DM[2].

Figure 1.5: The bullet cluster observed in the visible spectrum by Hubble (bright dots), X-ray emission by Chandra space telescope (pink) and calculated from gravitational lensing (blue). Credit: NASA

Cosmological observation of the CMB spectrum

Cosmic microwave background (CMB) captures the Universe at the time of last photon scattering, the borderline between ionized and electrically neutral, transparent Universe. This time indicates the end of the recombination epoch during which free protons and electrons formed neutral hydrogen atoms.

Relic photons form almost perfect black-body spectrum but its tiny temperature fluctuations ($\delta T/T \sim 10^{-5}$ [17]) provide an impressive amount of information about the Universe's composition. In the case of scalar perturbations (i.e. invariant under spatial rotations), the temperature fluctuations read [18]

$$\frac{\delta T}{T} = \frac{1}{4}\frac{\delta\rho_\gamma}{\rho_\gamma}(\mathbf{x}) + \Phi(\mathbf{x}) + \mathbf{n}\cdot\mathbf{v}_\gamma(\mathbf{x}) + \int_{t_r}^{t_0} dt\ (\dot{\Phi} - \dot{\Psi}), \tag{1.2}$$

where $\rho_\gamma(\mathbf{x})$ is the photons' density at last scattering, Φ and Ψ are the two gravitational potentials that characterize metric pertrubations, $\mathbf{v}_\gamma(\mathbf{x})$ is the average relative velocity of

[2] In this text, we do not touch the topic of self-interacting DM. For the recent constraints on such theories, see [15, 16].

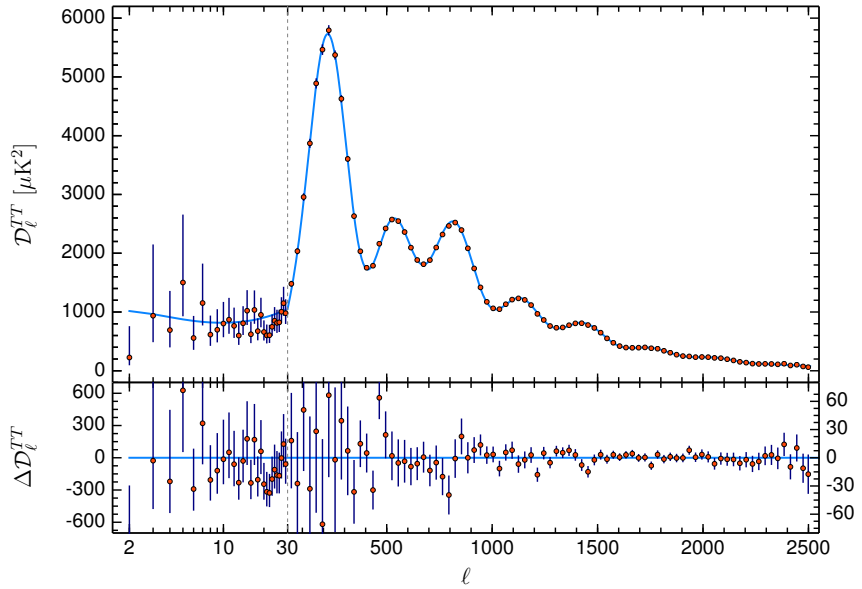

Figure 1.6: Temperature power spectrum measured by Planck 2018 (dots, with the $\pm 1\sigma$ error bars) and the best ΛCDM fit with parameters discussed in text (blue line). The lower panel shows the residuals with respect to this model [17].

baryons and photons and **n** is a normal vector. The expression is written in the conformal Newton gauge. The first term on the right-hand side describes the perturbations of the photon temperature at the moment of last scattering ($\delta\rho_\gamma/\rho_\gamma = 4\ \delta T_\gamma/T_\gamma$). The second term – redshifting (blueshifting) of the light when escaping potential wells (humps). These two terms account for the so-called Sachs-Wolfe effect. The third term describes the Doppler effect, and the last one – the redshifting (blueshifting) of the photons due to the time-dependent gravitational field (the integrated Sachs-Wolfe effect). DM affects the second term of Equation (1.2) extremely strongly, making the CMB measurement the most accurate in predicting the DM relic abundance in the Universe.

Accurate analysis of the CMB power spectrum (Figure 1.6) shows that the height of its third peak is most sensitive to the DM relative contribution to the total energy deposit, Ω_{DM}. This peak characterizes how strongly did matter clump relative to its repulsion governed by the pressure of baryonic matter[3].

The latest fit of the power spectrum with the ΛCDM model (or frequently called "the standard model of cosmology") by Planck Collaboration [17] shows that the Universe is spatially flat and its energy budget consists of only $\Omega_b = 4.9\%$ of the "usual" baryonic matter (i.e., stars, galaxies, etc.), $\Omega_{DM} = 26.8\%$ of the so-called *cold* DM (see Section 1.3 for definition) and $\Omega_\Lambda = 68.3\%$ of the least understood substance responsible for the accelerated expansion of the Universe, the so-called "dark energy".

[3]Here and below we use the jargon term "baryons", which in cosmology means "all the massive particles that interact electromagnetically".

Cosmological observation of structure formation

The fact that we observe extremely homogeneous Universe at the redshift $z_{\rm CMB} \simeq 1000$ and an extremely non-homogeneous Universe now (for example, overdensities of $\delta\rho/\rho \sim 1$ are needed for entering the non-linear regime of structure formation in which gravitational collapse takes place) is the apparent evidence of the existence of the additional matter component. This can be easily seen from the simplified picture of gravitational collapse. Let us assume the case of the matter-dominated Universe, a justified assumption since it is quite challenging for an overdensity to grow to the scales of observed structures during the radiation-dominated epoch[4]. The Friedmann equation then reads

$$H^2 = \frac{8\pi G}{3}\rho - \frac{k}{a^2}, \tag{1.3}$$

where a is the scale factor, $H = \dot{a}/a$ is the Hubble parameter, $\rho \simeq \rho_m$ is the matter's energy density, and k is the spatial curvature parameter. Let us now consider an area with a slightly higher density, $\rho' > \rho$, and write the Fridmann equation for it as well. Subtracting the two, we can find that the matter overdensities $\delta\rho = \rho' - \rho$ grow as

$$\frac{\delta\rho}{\rho} = -\frac{3k}{8\pi G a^2 \rho_m} \propto a, \tag{1.4}$$

where we used the relation $\rho = \rho_m \propto a^{-3}$. Estimating the relative growth of the scale factor $a_0/a_{\rm CMB} = z_{\rm CMB} + 1 \simeq 10^3$, we can conclude that without any new physics the maximum overdensities at present time are of the order of

$$\delta\rho_0/\rho_0 \simeq 10^3 \ \delta\rho_{\rm CMB}/\rho_{\rm CMB} = 10^3 \times 10^{-5} \simeq 10^{-2} \ . \tag{1.5}$$

Such small overdensities do not cause the gravitational collapse and thus fail to explain the observed structures. In contrast, adding the collisionless non-relativistic matter creates potential wells in which baryonic matter falls much more efficiently. Figure 1.7 illustrates the evolution of structures for different components. It demonstrates how the baryons follow the DM density distribution escaping the linear regime (rapid positive slope of the green curve), necessary for creation self-bound objects like galaxies, planetary systems, etc. at present time $t \sim t_\Lambda$.

In summary, the phenomenon called "dark matter" is evident from many *independent* observations on *extremely different* scales ranging from satellites of individual galaxies to the Universe as a whole. Explanation of this phenomenon *requires* new physics in the form of a new type (types) of matter, new physical processes (laws) or a combination of both.

[4]During this epoch, not only expansion but also pressure counteracts gravity.

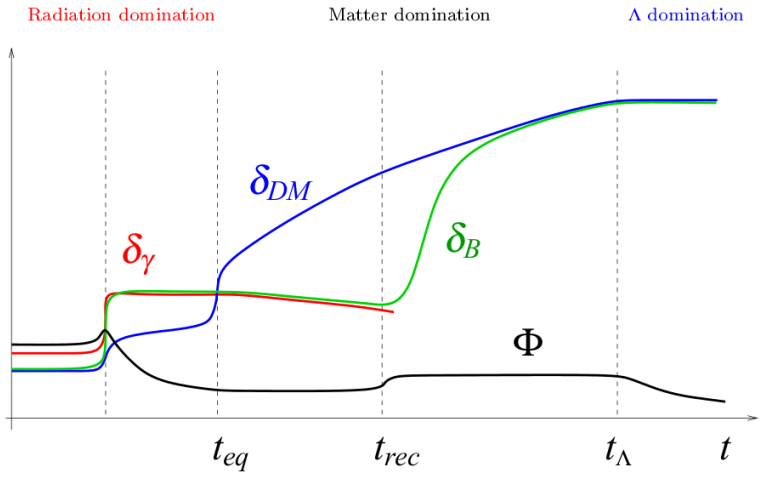

Figure 1.7: Schematic plot of the evolution of density pertrubations $\delta = \delta\rho/\rho$ for photons (red), baryonic matter (green) and DM (blue) [18]. The grid lines on the horizontal axis show the time of matter-radiation equality t_{eq}, recombination t_{rec} and Λ-domination t_λ. The black solid line shows the gravitational potential Φ.

1.2. Ways to tackle the dark matter problem

As discussed above, DM is a collection of gravitational phenomena that cannot be explained with the known tools in physics. Extension of our current picture of fundamental physics can be done in two ways: by keeping the number of building blocks and changing the laws they interact, or by adding new building blocks without modifying the known physics laws. Let us briefly discuss both paths here.

Dark matter without new particles

One of the ways to explain the obvious inconsistency between observed gravitational effects and our predictions is to assume that the well-tested theory of General Relativity (GR) is not valid at some scales/field strength. The class of models aiming to find the extended versions of GR are called *modified gravity theories*, the first version of which was the famous MOND theory (see, e.g. [20]). It was later generalized to the Lorentz-invariant form, an example of such theory is the TeVeS model [21]. However, in the framework of modified gravity it is extremely hard to explain *all* the phenomena discussed in Section 1.1 without effectively introducing new matter fields. These models are also in tension or provide worse fits to the new astrophysical, CMB and structure formation data than ΛCDM [22–24].

In principle, one can argue that since DM is a *collection* of phenomena, its astrophysical manifestations might have a completely different origin than the cosmological ones. One of the ways to address the first problem is to assume that the baryonic matter in astrophysical objects can clump, forming non-luminous or very dim compact objects, the so-called MACHOs (planets, faint dwarf stars and black holes) or neutral gas clouds. However, a combination of additional astrophysical observations shows that the mass fraction of these objects is *too small* to solely account for the effects listed in Section 1.1. In the case of MACHOs, the most

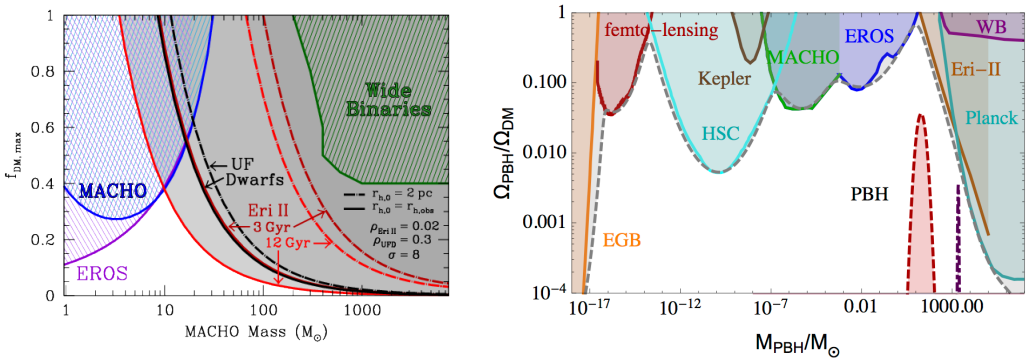

Figure 1.8: Combined observational on the MACHOs (left) and primordial black holes (right) as DM. According to studies presented, these object can account for only subdominant fraction of DM. For details, see [28, 29].

recent constraint comes from the microlensing observations which are seen as a periodic brightening of distant stars due to the Earth's motion with respect to the MACHO object (the lens) [25]. Even though this subject is still debatable and there are ways to relax some of the constraints, the current combined observations show that it is rather unlikely that MACHOs (including primordial black holes) can constitute the dominant fraction of DM (see Figure 1.8). Distribution of neutral gasses can be studied by their distinct emission lines (for example, in case of neutral hydrogen, the 21-cm line). Observations show that in most galaxies neutral gas comprises only 1% of mass [26] reaching up to 20% in some exceptional cases [27].

Finally, we can try to explain both cosmological and astrophysical manifestations of DM by elementary particles within the Standard Model (SM). The only stable and electrically neutral candidates are the three neutrinos. However, since neutrinos are fermions, there is a maximum phase space density they can occupy forming an object of mass M:

$$M/\left(\frac{4\pi}{3}r^3\frac{4\pi}{3}v^3\right) \leq \frac{2m_{\mathrm{DM}}^4}{(2\pi\hbar)^3}. \tag{1.6}$$

This estimate gives a lower bound on the DM mass m_{DM} that is usually referred to as *the Tremaine-Gunn bound* [30]. More recently, it was updated by considering dwarf galaxies and by taking their escape velocity $v = v_{\mathrm{inf}}$ as a crude estimate of the characteristic DM velocity in such objects. The lower mass limit of $m_{\mathrm{DM}} > 300 - 400$ eV was derived for the fermionic DM [31]. These results are, of course, in contradiction with the upper bound on the SM neutrino mass [32]. Moreover, these neutrinos would form the so-called "hot" DM, leading to a different large-scale structure picture (see Section 1.3).

We conclude that no theory can successfully explain all the evidence of DM described in Section 1.1 within the Standard Model of particle physics. Therefore, new particles must be added to the fundamental theory.

Dark matter explained by new particles

Since decades of searching for DM candidates withing the SM ended up in ruling out all the potential candidates (of course, the present bounds should be always reconsidered in case of doubts), the next logical step is to assume the existence of new particles beyond the Standard Model of particle physics (BSM). It is important to stress here that SM was tested in many different ways, showing excellent agreement between theory and experiment [4]. Therefore, it is crucial to respect the SM gauge symmetries, as well as mind all the experimental constraints when building a new theory. It is also important to mention that to date two more confirmed experimental observations require BSM physics. They are: the non-zero masses of standard model neutrinos and the observed baryon asymmetry of the Universe. The idea of solving all three problems at once is theoretically appealing, and there were several attempts to do so [33–35]. However, by now none of the candidates predicted by these models were found. Thus, here we will choose a more modest approach, focusing on explaining *DM origin only*, including however all its astrophysical and cosmological manifestations described in Section 1.1.

Combining the knowledge about the objects we want to describe, we can conclude on the following requirements to our new particle DM candidate:

- It should comprise 26.8% of the energy budget of the Universe.
- It should have a non-zero mass to be able to cluster.
- If it was ever relativistic, it should have slowed down early in the history of the Universe. In other terms, it should be almost perfectly cold when cosmological structures started to form (see Section 1.3).
- It should be electrically neutral[5].
- It should be stable on cosmological timescales.

Keeping these requirements in mind, let us discuss a bit more the kinematic properties of DM.

1.3. Coldness of dark matter

Depending on the kinematic regimes DM goes through at specific times during the Universe's evolution, DM candidates can be divided into three categories[37]:

- **Cold DM (CDM)**: particles were created/decoupled[6] non-relativistic.
- **Warm DM (WDM)**: particles were created/decoupled relativistic and became non-relativistic during the radiation-dominated epoch.

[5]For a discussion about the possibility of having millicharged DM, see [36].
[6]For the definition of "decoupling" see Chapter 3.

- **Hot DM (HDM)**: particles were created/decoupled relativistic and became non-relativistic during matter-dominated epoch.

This classification is useful when the structure formation subject is discussed. In the case of CDM, particles are very non-relativistic at the moment when structures start forming. The DM overdensities start to cluster on small scales first, forming larger clumps at later times. Thus, structures grow *from small scales to large scales*, resulting in the existence of objects on a large range of scales at present (see, e.g. [38]).

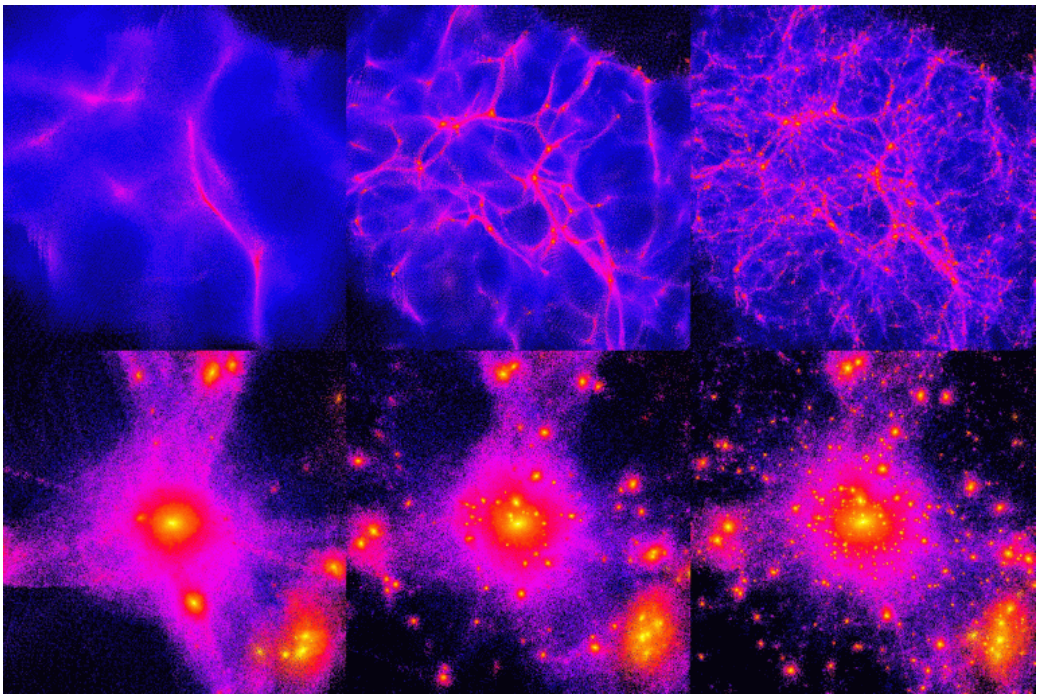

Figure 1.9: Large scale stucture simulations with CDM (e.g. WIMPs, left), WDM (e.g. sterile neutrinos, center) and HDM (e.g. active neutrinos, right). Bottom row corresponds to the zoomed-in pictures from the top row.
Credit: Ben Moore, University of Zürich.

If, on the contrary, DM has non-zero velocity at the moment of structure formation, particles tend to escape regions with small overdensities, preventing the collapse. Such balance holds until the overdensities gain some critical mass, and then collapse takes place. In this picture there is a *minimum scale* at which structures are formed and its size is related to the *free-streaming length* of the DM particle (defined in comoving coordinates):

$$\lambda_{FS}^{\mathrm{com}} = a(t) \int_0^t d\tau \frac{v(\tau)}{a(\tau)}, \tag{1.7}$$

where t is physical time, $a(t)$ is the scale factor and $v(t)$ is the typical velocity of DM particles.

Simulations of the large-scale structure of the Universe presented in Figure 1.9 shows the drastic difference between the three types of DM discussed above. In the case of HDM, $\lambda_{FS}^{\mathrm{com}}$ is very big, preventing the formation of most of the observed structures. Active

neutrinos discussed in Section 1.2 fall in this category and were historically ruled out for this exact reason. CDM is in a good agreement with structure formation observations on very large scales and was for a long time considered as a benchmark model in particle physics, astrophysics and cosmology communities. However, some observations show a potential lack of small structures (e.g. *the core-cusp problem*, *the missing satellites problem* and *the too big to fail problem*, see [39] for a review), making the WDM models an actively discussed topic. Since all these observations are made for objects with a large fraction of baryons, it is unclear whether they indicate the warm nature of DM, or speak for our lack of understanding of the complicated processes in baryonic matter. Various new ideas of how to distinguish between the CDM and WDM have appeared during last years (see, e.g. [40–43]). Hopefully, they will help to shed light on this question.

To date, there is no confirmed evidence of the necessity to introduce WDM. Hence, in this work, we focus on the CDM candidates. Many of the conclusions made here, however, can be extended to the WDM case.

2. Particle dark matter

In this chapter, we focus on the general procedure for building a new particle physics theory that includes DM from the bottom-up approach. We discuss the main idea of how to couple new fields to the SM in the *effective field theory* framework. We also show the lowest-dimension realization of these couplings, the so-called *portals*, paying the most attention to the Higgs portal which will be the subject of our interest in Chapter 4 and Chapter 5. We very briefly mention the mass range in which the existing DM models are predicted, specifying some models in the GeV-TeV range that we will be the scale of interest in the main part of this thesis. Finally, we discuss the principal ways the DM models of this mass range can be tested experimentally.

2.1. BSM theories from the bottom-up

The general procedure of formulating a new theory using Lagrangian formalism is:

- Define new fields (including their transformation properties with respect to the Lorentz group, SM gauge group, as well as potential new groups).
- Write down *all* the possible gauge- and Lorentz-invariant field operators up to a certain mass dimensionality that involve both SM and new fields and that are allowed by the symmetries.

The second step is due to a common principle that "everything that is not forbidden should be allowed". After a theory is formulated in such a way, it should be tested both for the internal consistency (e.g. the absence of gauge anomalies) and against existing experiments. These experiments put constraints on the masses of the new states and the new interactions, in some cases pinning them down to extremely fine-tuned values (see, e.g. discussions about strong CP [44] and flavor hierarchy [45] problems in the SM, as well as about the hierarchy problem in the presence of BSM states well above the electroweak scale [46]). The two main attitudes regarding such findings are: trying to find a deeper reason behind the observed fine-tuned patterns (usually related to some additional symmetries that are slightly broken) or by accepting that some fundamental values might be in contradiction with our idea of "naturalness". While both ways of thinking should be proceeded by the community since they can give drastically different insights, we will follow the latter approach putting aside the aesthetic aspect of the theory and focusing purely on the explanation of the observed experimental effects.

Finally, a theory should have clear predictions of experimental observables. Theories that fulfill all these requirements can be falsified. It is also important that they can be verified in the foreseen future, which in case of particle and astroparticle physics is related to some specific range of masses and coupling strengths accessible by current and upcoming experimental techniques.

Since experimental sensitivity is bounded from above in energy, there is always a problem of the potential existence of heavy and thus inaccessible states. There are two ways to address this problem. The first one is usually called the *top-down* approach. Its main idea lies in constructing the full theory that includes states at all energy scales and then predicting the low-scale spectra and related observables by integrating out heavy states. The second one, the *bottom-up* approach, consists in introducing only states at "low" energies and writing the Lagrangian terms in the form that assumes the heavy states to be already integrated out. It is usually done using the so-called *effective field theories (EFTs)*. Even though the first approach is more theoretically appealing, it requires a lot of effort invested in working out all the details of a particular model with only a subset of parameters being relevant experimentally. The bottom-up approach, on the other hand, allows to capture all the possible low-energy effects of a UV-complete theory without specifying the latter. Thus, in this work, we will adopt the EFT approach, trying to predict physics effects at currently available energy scales.

The EFT approach

This approach is based on the assumption that the full (UV-complete) theory is defined at some high energy scale Λ that is well separated from the scales we operate experimentally with. The famous historical example of an EFT in particle physics is Fermi's interaction, see [47] for a review. The corresponding UV-complete theory is the theory of W-mediated weak interactions, and it becomes relevant at the scale of the W boson mass, $\Lambda = m_W$.

Currently, experiments are sensitive to the energy scales up to a few TeV with the exception of some very high-energetic cosmic rays telescopes [48, 49], so we assume Λ to be at least in the high-TeV range. The Lagrangian $\mathcal{L}$ of an effective theory can be written as (see also [50, 51])

$$\mathcal{L} = \mathcal{L}_{SM} + \sum_i \lambda_i \frac{O_i^{(\delta_i)}}{\Lambda_i^{\delta_i - 4}}, \tag{2.1}$$

where λ_i are dimensionless effective coupling constants, Λ_i are scales of new physics and O_i are operators of mass dimension δ_i (such that $O_i \propto E^{\delta_i}$) that contain new physics states[1]. The power of Λ_i was deduced from the requirement that the action is dimensionless and that we work in 3+1 space-time dimensions.

Following the procedure described in Ref. [53], we can classify the operators O_i and the corresponding quantum field theories based on their dimension δ_i:

- If $\delta_i < 4$, O_i is called *relevant* and the theory is superrenormalizable.

[1] Some EFTs operate with the SM fields only. One of the famous examples is the SMEFT (see [52] for a review). Such options are, however, beyond the scope of the current discussion.

$B^Y_{\mu\nu}$	Vector portal (kinetic mixing)	d=2
$\bar{L}\tilde{H}$	Neutrino portal	d=5/2
$H^\dagger H$	Higgs (scalar) portal	d=2

Table 2.1: Singlet SM operators that play a role of portals to new physics. The third column describes the mass dimension of the corresponding operator.

- If $\delta_i = 4$, O_i is called *marginal* and the theory is strictly renormalizable.
- If $\delta_i > 4$, O_i is called *irrelevant* and the theory is nonrenormalizable.

The renormalization-group classification specifies whether the amplitudes of processes that include these operators diverge with the possibility of absorbing these divergences by a finite number of counterterms (superrenormalizable and renormalizable[2]) or diverge and an infinite number of counterterms is needed to remove the divergences (nonrenormalizable).

The new operators in Lagrangian in Equation (2.1) can thus be regrouped and written down in a more useful way (for simplicity we assume only one additional scale, i.e. $\Lambda_i = \Lambda$),

$$\mathcal{L} = \mathcal{L}_{SM} + \mathcal{L}^{\text{renorm}}_{BSM} + \sum_{i,n} \lambda_{in} \frac{O^{(i)}_{BSM} O^{(n+4-i)}_{SM}}{\Lambda^n} + \sum_{i,n} \lambda_n \frac{O^{(n+4)}_{BSM}}{\Lambda^n}, \tag{2.2}$$

where the second term stands for renormalizable operators that include new fields, the third term describes non-renormalizable interactions of these fields with the SM ones, and the last term represents non-renormalizable operators within the new sector. The last two sets of operators represent the low-energy limit of a theory defined at energies of the order of Λ. The EFT approach is useful since it allows to make predictions for whole classes of new theories that have the same low-energy structure. It is, however, important to keep in mind that even though the heavy states do not affect our experimental predictions, they might have an impact on the history of our Universe at very early times. Thus, for some UV-complete realizations of these EFTs, parts of the parameter space might be ruled out from cosmological observations.

The portals to new physics

Let us now take the third term of Equation (2.2). It describes how the BSM fields couple to the SM ones. Since we want to preserve the gauge symmetry of the SM, either the new operators O_{BSM} transform under this symmetry or O_{SM} have to be SM gauge invariants. Let us for simplicity focus on the second option. The SM singlet operators of the lowest dimension are usually referred to as *portals* (see also an overview of portals in [50, 54]). A list of them can be found in Table 2.1[3].

[2] The difference between the two cases is that only a finite number of Feynman diagrams diverge in superrenormalizable theories whether it happens at all orders in perturbation theory (but for a finite number of amplitudes) in renormalizable theories.

[3] Sometimes the so-called *axion portal* is added to this list. We do not discuss it here but refer the interested reader to [55].

Here $B^Y_{\mu\nu}$ is the hypercharge field strength tensor (since a gauge strength tensor is gauge-invariant only in the Abelian case), L is a lepton doublet and H is Higgs field ($\tilde{H} = i\sigma_2 H^*$, where σ_2 is the second Pauli matrix). The last column indicates the mass dimension of the corresponding operators.

If coupled to BSM operators of appropriate dimension, these portals allow the inclusion of new physics in a renormalizable way, i.e. such that $n \leq 0$ in the third term of Equation (2.2). However, in this text, we will refer to the Higgs portal independently of the value of n. Let us now briefly discuss the lowest-dimensional options to couple the above operators to new fields preserving Lorentz invariance.

Vector portal (kinetic mixing)

The most straightforward way to construct an interaction term with the first operator in Table 2.1 is by coupling it to a new strength field tensor $F'_{\mu\nu}$ of a dark $U(1)_D$ group via

$$\mathcal{L}_V \supset -\frac{\epsilon}{2} B^{\mu\nu} F'_{\mu\nu}, \tag{2.3}$$

where the coupling ϵ is usually called *the kinetic mixing parameter*. If $U(1)_D$ is spontaneously broken, the new gauge field A'_μ associated with $F'_{\mu\nu}$ acquires mass through, e.g. the Higgs mechanism, as well as a coupling to the electromagnetic current, $\propto \epsilon \times J^\mu_{EM} A'_\mu$, which is suppressed by the mixing parameter. Because of this suppression, A'_μ is usually called *the dark/hidden photon*. Models of dark photons are rich in phenomenology. For an extensive program devoted to their searches, see Ref. [56, 57] and references therein. More complicated versions of this model often involve gauging one of the global symmetries of the SM leading to yet different exciting consequences (see, e.g. [58]).

Neutrino portal

The only renormalizable interaction that includes the second operator from Table 2.1 involves right-handed SM singlet fermion field N_R and can be written as

$$\mathcal{L}_\nu \supset -F_{\alpha I} (\bar{L}^\alpha \tilde{H}) N^I_R. \tag{2.4}$$

Here $F_{\alpha I}$ is the Yukawa coupling, indices α and I numerate the lepton flavors and the new fields respectively. The interaction above has gotten a lot of attention in the recent decades since the new field N_R (which is often called *sterile neutrino* or *heavy neutral lepton (HNL)*) can generate Dirac masses of active neutrinos. In the context of the confirmed neutrino oscillations, right-handed neutral leptons become a must-have addition to the SM[4], triggering several ongoing and proposed searches [57, 60]. Through the interaction (2.4), sterile neutrinos mix with the active ones, consequently taking part in all the neutrino-involved processes, but with the rate suppressed by $F_{\alpha I}$.

Higgs (scalar) portal

[4]For a review on neutrino oscillations and necessity of sterile neutrinos for their explanation, see [59]

The lowest-dimension operators in this case include new scalar fields ϕ, singlets with respect to the SM gauge groups. The corresponding Higgs-ϕ mixing terms read

$$\mathcal{L}_H \supset -(\kappa\phi - \lambda\phi^2)H^\dagger H. \tag{2.5}$$

In general, the full Lagrangian includes also terms $\propto \phi,\ \phi^2,\ \phi^3,\ \phi^4$, some of which might be forbidden by a symmetry of the dark sector. After electroweak symmetry breaking (EWSB), the Higgs field acquires vacuum expectation value (VEV) v,

$$H = \begin{pmatrix} 0 \\ (v + h_0)/\sqrt{2} \end{pmatrix}, \tag{2.6}$$

where h_0 would have been the observed Higgs boson if there was no new scalar interactions with H. In our case, however, ϕ and H do not have defined masses in the used basis since they mix with each other. The mixing Lagrangian has a general form of

$$\mathcal{L}_{\text{mix}} = -\frac{1}{2}\left(\mu_{h_0} h_0^2 + 2\mu_{\text{mix}} h_0\phi + \mu_\phi \phi^2\right), \tag{2.7}$$

where the (dimensionfull) parameters μ_i can be calculated form a specific Lagrangian. The physical scalars S and h can be obtained by diagonalizing the above terms. In principle, the new scalar ϕ may acquire VEV as well, generating more mixing terms. The presented model (as well as its version with a new complex scalar) is of a great interest in the context of physics at the LHC after the Higgs discovery since it directly affects Higgs couplings that are currently being measured with increasing precision (see, e.g. [61–63]). Scalars also play an important role in cosmology. As an example, we refer to a study of the impact of a new scalar on the type of the electroweak phase transition, which is important for successful baryogenesis [64].

In the DM context, the model described by Lagrangian in Equation (2.5) is quite restricted if ϕ itself plays the role of DM (see Section 3.3). However, it can serve as a mediator between SM and DM, the scenario we will encounter in Chapter 5. We will also see a higher-dimensional fermionic realization of the Higgs portal in Chapter 4.

2.2. The ballpark of dark matter candidates

So far DM revealed itself through gravitational interactions only, there is a plethora of ways to build a particle physics model of it. A very important remark is that *there is no real reason* for DM to interact with the SM particles other than gravitationally. Unfortunately, if the latter is true, we have no chance to detect DM and learn about its nature. However, since so far *nothing forbids* other DM interactions, it makes sense to at least try to test such models experimentally.

The comprehensive overview of the existing DM candidates is a close-to-impossible task and is beyond the scope of this work. Instead, we would like to give the reader a feeling of

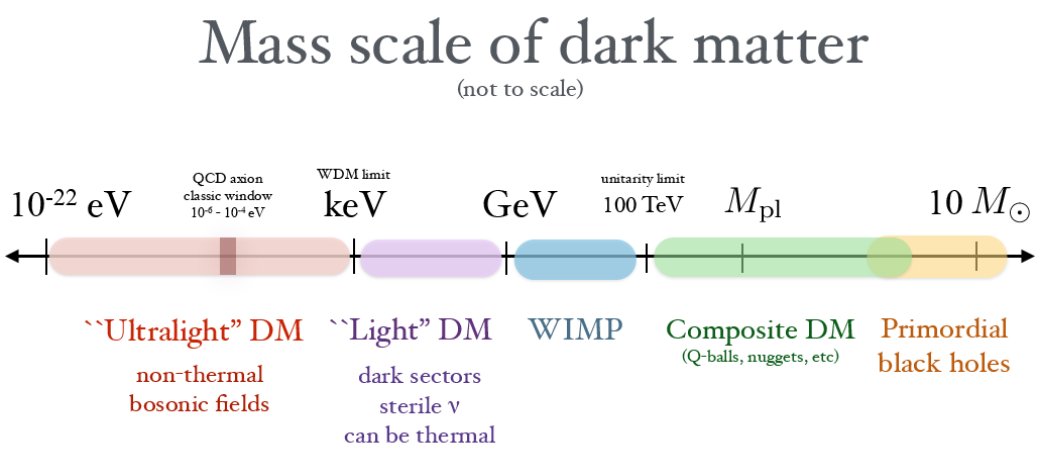

Figure 2.1: The (very roughly estimated) mass scale of the most popular DM candidates [65].

the mass scales at which DM theories operate. These are shown in Figure 2.1.

We see that masses below the limit of Equation (1.6) are possible. The bosonic DM below this mass limit, however, would have *never* been in thermal equilibrium with the standard model plasma. Very popular ultralight DM candidates are the axion-like particles. Being produced non-thermally, they still form CDM (see, e.g. [55, 66]). The absolute lower bound of $m_{\rm DM} > 10^{-22}$ eV is derived from the requirement of DM wavelength being comparable to the smallest structures observed, the DM candidates at the lower edge of Figure 2.1 are usually referred to as *fuzzy DM* [67].

DM in the range of keV-MeV can consist of both bosons and fermions. It can also be produced thermally, opening up a lot of possibilities for various proposed models. For example, several Supersymmetric (SUSY) candidates end up in the discussed range [68, 69]. Another candidate, sterile neutrino, become increasingly popular [70][5], especially in the light of the possible 3.5 KeV line signal [72].

The GeV scale was historically preferable for the so-called *weakly interacting massive particles* (WIMPS). By now, the simplest candidates of this type are highly constrained leading to more complicated WIMP-like particles of MeV-TeV mass and different spins being actively proposed. For more details on the most studied DM candidates in this mass range, see Ref. [73, 74], as well as the discussion in Chapter 3.

Abundant particles with $m_{\rm DM} > 100$ TeV face new problems, e.g. the danger of overclosing the Universe and the lack of testability. Superheavy fundamental particles are usually called *WIMPzillas*. They have to be lighter than the Planck mass and are frequently produced non-thermally during reheating [75, 76]. Above Planck mass composite objects like dark nuggets [77], nontopological solitons like Q-balls [78] and primordial black holes, discussed in Section 1.2, are the main players in the market.

[5] It has been shown that the most popular sterile neutrino with the mass $m_N \sim$ few KeV has to be resonantly (and non-thermally) produced in order to account for a sizeable fraction of DM [71].

In this thesis, we will focus on thermally produced elementary DM in the GeV-TeV range. Its production mechanism discussed in Chapter 3 requires a DM-SM interaction strength that is, in principle, testable at current colliders. Therefore, such models are very appealing experimentally.

2.3. Dark matter detection

In Section 1.1 we discussed the main evidence of DM. Here we will give a short summary of the ways to search for it. There are three types of searches, complementary to one another: indirect detection, direct detection and collider searches. Let us briefly explain the general principle of each of them.

Indirect detection

This search consists in the observation of SM particles that were created in DM annihilations, decays, or scatterings and that come towards Earth from astrophysical objects. Typical objects under observation are: dwarf spheroidal galaxies (dSph), galaxy clusters, large galaxies, and even the Sun. The observed signatures (frequently called *messengers*) are stable SM particles that can be either the annihilation/decay products themselves or the daughter products of unstable SM particles. Figure 2.2 illustrates the distance scales at which sources of the indirect detection signals are found and the searched messengers.

The main challenge for indirect detection searches is the large astrophysical background. The excess flux per solid angle $\Delta\Omega$ of a messenger X can be related to the corresponding DM annihilation cross section as (see for detail [7])

$$\frac{d\Phi}{dE_X} = \frac{1}{4\pi}\int_{\Delta\Omega} d\Omega \int dl \rho(l)^2 \frac{\langle\sigma_{\rm ann} v\rangle}{2m_{DM}^2}\frac{dN}{dE_X}, \tag{2.8}$$

where $\rho(l)$ is the distribution of DM inside the observed object (e.g. galaxy) depending on the coordinate l along the line-of-sight, $\langle\sigma_{\rm ann} v\rangle$ is the velocity-averaged annihilation cross section and dN/dE_X is the differential yield of X per annihilation.

The experiments that search for indirect detection signatures are primarily balloons or satellites which measure charged (anti)particles and photons in the X-ray and gamma-ray range, Cherenkov telescopes and large neutrino observatories. For more details on the indirect detection experimental techniques, see [79].

Indirect detection searches are more sensitive to rather high DM masses from the collider physics point of view (the strongest bounds are typically obtained for $m_{\rm DM} \sim 0.1 - 10$ TeV). In the case of cosmic ray observatories, the main reason is atmospheric shielding that prevents low-energy messengers from reaching ground-based detectors, as well as a smaller number of astrophysical sources of high-energetic particles. In the case of neutrino experiments, the growing-with-energy neutrino cross section leads to an increased sensitivity to high DM masses. In Figure 2.3 we show the combined bounds on the DM annihilation cross section in different mass windows. Interestingly, for low masses, measurements by Voyager1 spacecraft

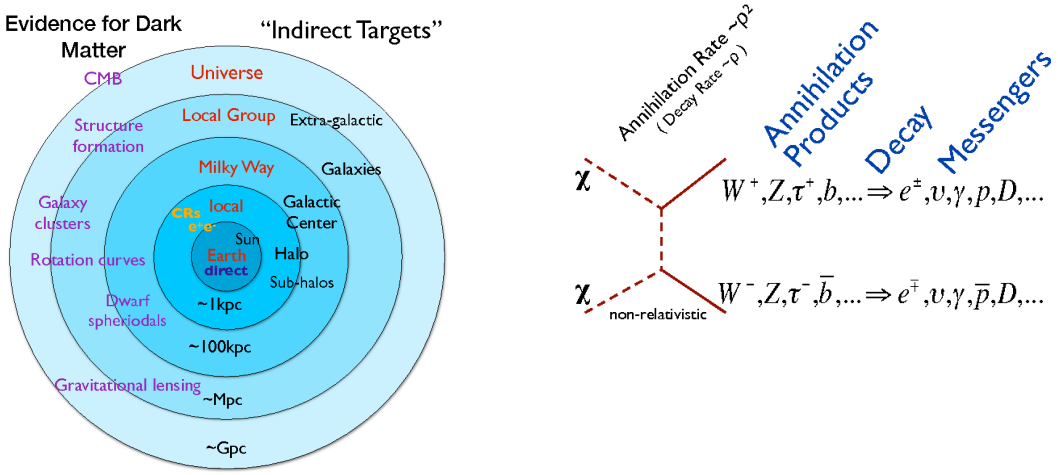

Figure 2.2: Sources and signatures of indirect detection. Left: distance scales at which DM evidence, as well as the indirect detection targets are observed. Right: possible annihilation channels and corresponding messengers [79].

are the strongest [80]. This is due to the absence of shielding of the incoming cosmic rays by the heliosphere. Similarly, the limits on the DM decays and scatterings can be obtained (see, e.g. [79] for an overview).

Direct detection

In this type of search, DM scatterings off SM particles (protons and electrons) are tested by measuring the recoil energy of the latter. The sensitivity of these searches is by design limited by the active neutrino scatterings. The corresponding lower testable values of the DM-SM cross-section is often called *the neutrino floor (neutrino background)* [82]. We will briefly discuss here the underlying physics, sending the reader for details to [7].

Let us focus on the nuclear scatterings. The differential rate of the recoiled particle per unit detector mass is

$$\frac{dR}{dE_R} = \frac{\rho_{\rm DM}}{m_{\rm DM} m_N} \int_{v_{\rm min}}^{v_{\rm max}} d^3v \; v \; f(\mathbf{v},t) \frac{d\sigma_{\rm scatt}}{dE}, \tag{2.9}$$

where $\rho_{\rm DM}$ is the DM energy density, $m_{\rm DM/N}$ is the DM/nucleon mass, $f(\mathbf{v},t)$ is the DM velocity distribution in the laboratory frame and $\sigma_{\rm scatt}$ is the DM-nucleon scattering cross section. The lower integral limit denotes the minimum velocity that can result in the recoil energy E_R. In the elastic scattering case, $v_{\rm min} = \sqrt{m_N E_R / 2\mu^2}$ and $\mu = m_{\rm DM} m_N / (m_{\rm DM} + m_N)$ is the DM-nucleon reduced mass. The upper limit is the escape velocity of the DM particle.

Direct detection signatures are usually divided in two categories: *spin-dependent (SD)* and *spin-independent (SI)* resembling the sensitivity of the corresponding cross section to

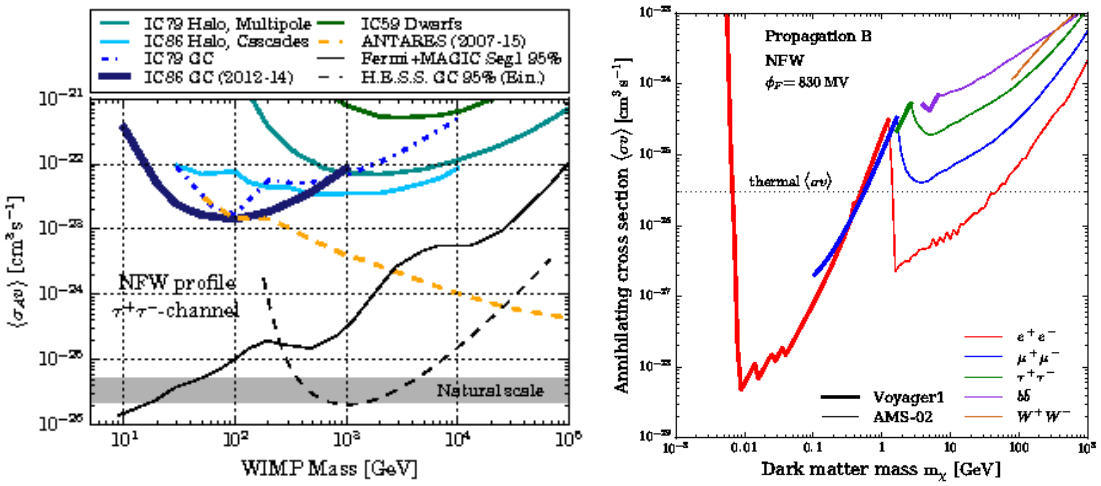

Figure 2.3: Indirect detection detection bounds on the DM annihilation cross section in the high-mass region (left) [81] and the low-mass region (right) [80].

the nucleon's spin. In general, a DM particle χ can couple to a SM quark Q through the following effective operator

$$\mathcal{L}^{\text{eff}}_{DD} \propto (\bar{\chi}\Gamma_\chi \chi)(\bar{Q}\Gamma_Q Q), \tag{2.10}$$

where $\Gamma_{\chi/Q} = I, \gamma_5, \gamma_\mu, \gamma_\mu\gamma_5, \sigma_{\mu\nu}$. Recalling the explicit form of the spin operator $\mathbf{s} = \gamma_5\gamma_0\boldsymbol{\gamma}$, one can show that in the case of the non-zero axial-vector, $\gamma_\mu\gamma_5$, or tensor, $\sigma_{\mu\nu}$, parts the DD cross section contains terms that depend on the nuclear spin.

The DM-nucleon cross section can be written in the form [83]

$$\text{SI:} \quad \frac{d\sigma_{\text{SI}}}{dE_R} = \frac{2m_N}{\pi v^2}[Zf_p + (A-Z)f_n]^2 F^2_{\text{SI}}(q), \tag{2.11}$$

$$\text{SD:} \quad \frac{d\sigma_{\text{SD}}}{dE_R} = \frac{16m_N}{\pi v^2} G_F^2 J(J+1)\left(\frac{a_p\langle S_p\rangle + a_n\langle S_n\rangle}{J^2}\right)^2 F^2_{SD}(q), \tag{2.12}$$

where Z and A are the nucleon's charge and mass number, f_p/f_n are the effective couplings of the DM to protons/neutrons, $F_{SI/SD}(q)$ is the nuclear form factor which depends on the momentum transfer $q = \sqrt{2E_R M_N}$, G_F is the Fermi constant, J is the nucleon's isospin, $\langle S_{p/n}\rangle$ are the proton/neutron average spin expectation values and the cross section 2.12 was calculated for the axial-vector current.

The bounds on the scattering cross sections are obtained from both indirect detection searches and the dedicated direct detection experiments. Among the latter, the currently most stringent bound in the high-mass region is provided by the XENON1T experiment [84]. There, the nuclei recoil energy is reconstructed from the measured ionized electrons, as well as from photons, emitted by the excited nuclei. At DM masses $m_{\text{DM}} \leq 10$ GeV, the sensitivity of the nuclei-based experiment is low due to the tiny recoils (however, recently a new way of analyzing the data was proposed to mitigate this problem [85]), and experiments measuring DM-electron scatterings take over. The detector material of the latter differs from neutral atoms or molecules to semiconductors, more proposals have recently come to the

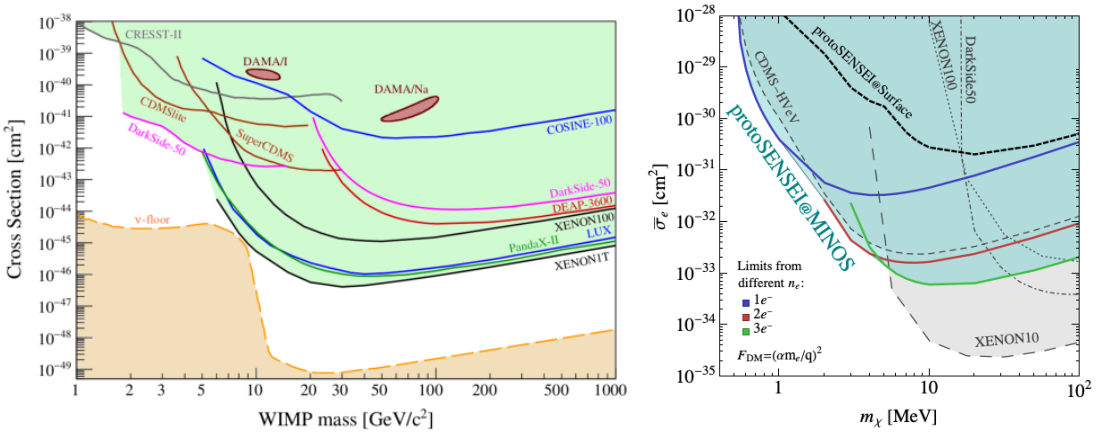

Figure 2.4: Direct detection upper limits on the SI DM-nucleon (left) [91] and DM-electron (right) [92] cross-sections.

market [86–89]. The detection products might be either excited electron themselves or the consequent products of their excitation, like photons or phonons. For the more comprehensive overview of new roads in DM detection (including searches beyond DM-SM scatterings), see [90]. For illustration, we present the latest combined result of nucleon- and electron-based direct detection experiments in Figure 2.4. We see that currently, nuclear-based direct detection experiments exclude smaller DM scattering cross sections than their electron-based versions. The typical sensitivity of these experiments peaks at a characteristic mass, losing sensitivity to lighter DM particles that cause too little recoil energy, and to very heavy DM due to lower abundance of such particles.

We conclude that direct detection puts the strongest constraints on DM-SM interactions in the mass range, considered in this work. Indirect detection bounds become crucial for DM masses $m_D \gtrsim$ few TeV.

Collider searches

The last type of DM search aims for detecting traces of dark particles in SM particle collisions. Of course, if DM is produced in such processes, its interactions with the known matter is negligible and it would freely escape the detector. Thus, traditionally the approach similar to the neutrino "detection" is used. The idea is to apply the energy-momentum conservation law to the visible objects (photons, leptons, jets, etc.). In case it is not conserved, we can conclude that more particles were emitted. The amount of energy disbalance in a process is usually quantified by the *missing energy*,

$$\mathbf{E}^{miss} = -\sum_i \mathbf{p}_i^{out}, \tag{2.13}$$

where $\mathbf{p}_i^{out}$ are the momenta vectors of the visible outgoing particles[6]. The corresponding

[6]Note that the quantity shown is, strictly speaking, the *missing momentum* of a process. The confusing name was historically given to this quantity since it was used for massless neutrinos first.

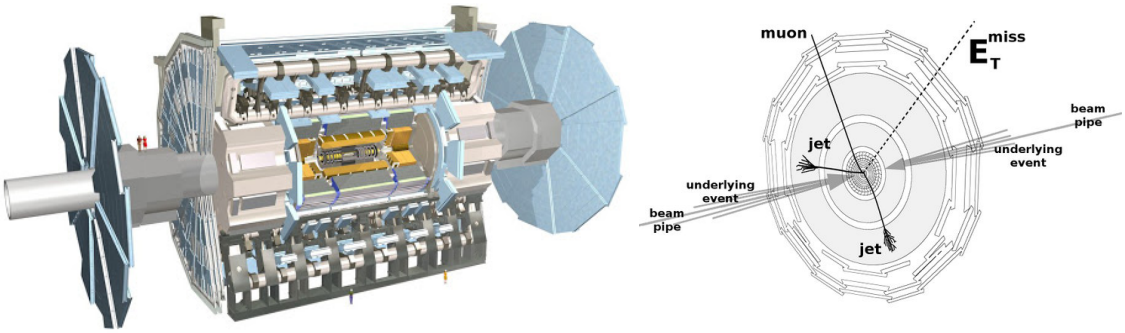

Figure 2.5: Left: ATLAS detector as an example of the typical cylindrically-shaped detectors at colliders. Right: the illustration of missing energy, $\mathbf{E}_T^{miss}$, reconstruction in the transverse plane by summing up vector momenta of the outgoing muon and jets.
Image credit: ATLAS Collaboration & Abdellah Tnourji

searches are referred to as *missing energy searches*.

A typical collider can be pictured as two oppositely-moving circular beams with a detector/detectors pierced on its beam pipe (see left panel of Figure 2.5 as an example). These detectors are placed in special points where the collider beams cross and where the collisions take place. Most of the initial particles do not meet any colliding partners from the opposite beam and proceed in the direction along the beamline (i.e. *forward direction*), whereas particles that come out of a collision, travel in various directions. In order to work with quantities that are independent of the colliding particles' boost, it is frequently useful to look at observables in the plane perpendicular to the beamline (i.e. *transverse plane*). The energy-conservation law requires that the transverse momentum, p_T, of the final state should be zero. The imbalance of p_T is called *the missing transverse energy (MET)* and is usually the focus of experimental analyses that search for DM (see right panel of Figure 2.5).

The main background sources for missing energy are the SM processes with neutrino final states or mismeasured events. They include:

- Neutrino-antineutrino pair produced via $Z^{(*)} \to \nu\bar{\nu}$ (irreducible background).
- Neutrino + lepton if the latter is not detected (in case of τ-lepton – if its hadronic decay products are missed).
- Jets that are mismeasured.

The missing energy analyses, being extremely sophisticated, control these backgrounds pretty well. The problem, however, becomes extremely challenging if the original signature has little MET, or if the processes' visible decay products are very low-energetic and thus are lost in the SM background. As we will discuss in Chapter 4 and Chapter 5, a relatively new (in the DM context) type of search that uses the displacement information of the detected objects circumvents the above issues quite successfully.

The above searches test DM couplings in different ways. However, in many models, these couplings are related to one another. In Section 3.2, we discuss the possible relations, as well as connections to the relic density of DM.

3. Thermally produced dark matter

In this chapter, we focus on DM produced in a freeze-out process, calculating its relic abundance. We discuss why the most minimalistic DM models either fail to explain the combination of observed effects, or are hardly testable at current colliders. We also list the most popular ways to "save" the thermal relic.

As mentioned in Chapter 2, based on their production mechanism, DM particles can be divided into two categories. DM from the first category is produced similarly to all the SM particles. The latter were in equilibrium after reheating and later on when the Universe has expanded and cooled down, departed from this equilibrium. In this case, we say that the particles were produced (i.e. their relic density was created) in the *freeze-out* process. A typical example of such particles is WIMPs, we will discuss the physics of their production later in this chapter. Alternatively, one can imagine new particles with such tiny couplings to the SM that they have *never* entered equilibrium with the SM plasma (however, they could have been in equilibrium with other states withing the dark sector). In this case, we say that DM was produced trough *freeze-in*. Inspired by the way the known particles were created, we focus in this work on the former production mechanism.

Let us first clarify what the term "equilibrium" means in this context.

Two types of equilibrium

- *Kinetic (thermal) equilibrium*: A *particle* is in kinetic (thermal) equilibrium if its momentum distribution function is of the equilibrium shape (i.e. Bose-Einstein/Fermi-Dirac in the case of bosons/fermions). Particles χ remain in kinetic equilibrium with particles f in the plasma as long as their average scattering rate off f is larger than the Hubble rate: $\Gamma_{scat} \gg H$ (see left panel of Figure 3.1 for illustration). In this case, χ and f share the same temperature T. At high energies all SM particles are in thermal equilibrium with one another. For temperatures $T \lesssim 3$ MeV, when active neutrinos have decoupled, the plasma's temperature is usually associated with the photons' temperature.

- *Chemical equilibrium*: A *process* is in chemical equilibrium when its rate is equal to the reverse one (see right panel of Figure 3.1). We will say that a *particle* is out of chemical equilibrium when there is no process in which it takes part and that is in chemical equilibrium.

Additionally, if not specified, we will say that a particle is *in equilibrium* when both kinetic and chemical equilibrium take place. We will call the moment of its departure from chemical equilibrium the *decoupling* moment.

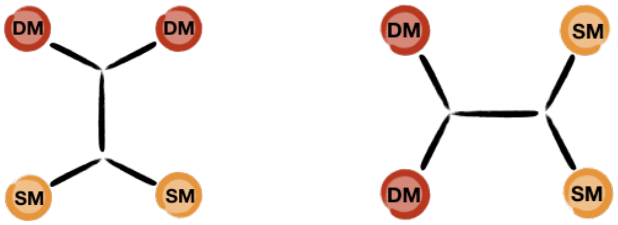

Figure 3.1: Processes that set equilibrium. Left: scatterings are responsible for kinetic (thermal) equilibrium. Right: annihilations as an example of the number-changing processes, responsible for chemical equilibrium.

If at the moment of decoupling $a_{\rm dec}$ (here we use the scale factor a as a measurement of time) kinetic equilibrium holds, DM distribution function is of the equilibrium shape. It is easy then to predict the evolution of its distribution function at later times $a > a_{\rm dec}$ (see [59] for derivation):

$$f(p,t) = f_{\rm dec}\left(\frac{a(t)}{a_{\rm dec}}p\right), \tag{3.1}$$

where p is the absolute value of DM three-momentum at $a = a_{\rm dec}$ and we assumed homogeneously and isotropically distributed DM. Note that this relation is correct in the assumption of instant DM decoupling. In reality, this process is stretched out in time since particles from the high-energetic tail of the distribution decouple later than the majority of DM particles. This results in distortions of the spectra of decoupled particles, a well-known effect in neutrino physics and lately discussed in the context of new physics [93]. However, this effect is negligible in the case of CDM, so we can safely use Expression 3.1 when predicting the DM relic abundance at present.

3.1. Relic density

Accurate prediction of the DM relic abundance is crucial for the verification of DM models. In this section, we go through the calculations and underlying physics assumptions the majority of publicly available DM codes use. We aim to draw a clear picture of freeze-out that will help a reader understanding the issues simple WIMP models face, as well as the "work-around" mechanisms of DM production, one of which will be the important finding of Chapter 4.

Let us start with collecting the assumptions about the DM candidate of our interest discussed in previous chapters:

Assumption 1. *DM interacts with the SM particles not only gravitationally.*

Assumption 2. *DM is a cold relic (CDM).*

Assumption 3. *DM used to be in equilibrium with the SM plasma but at some point it decoupled (freeze-out production). This process sets its relic abundance.*[1]

[1] In case DM re-entered equilibrium several times, we are interested only in the last process of decoupling since particles lose their memory of the evolution history once in equilibrium.

An intuitive picture of freeze-out

Let us first start from a qualitative picture of the freeze-out process by imagining a comoving volume with the side length $a(t)$ (where a is the scale factor), filled with DM particles in the expanding Universe. We will assume homogeneous and isotropic space-time working in the FLRW metric,

$$ds^2 = -dt^2 + a^2(t)d\Sigma^2, \tag{3.2}$$

where $d\Sigma^2$ is the spatial metric. If DM has no interactions, the total comoving number of DM particles does not change,

$$N = n(t)a(t)^3 = \text{const}, \tag{3.3}$$

where $n(t)$ is the particles' number density. If, on the contrary, DM particles interact, their number changes with time proportionally to the comoving interaction rate $\Gamma(t)^{\text{com}}$:

$$\frac{dN(t)}{dt} = -\Gamma(t)^{\text{com}}. \tag{3.4}$$

Factoring out the expansion-induced part on the right-hand side of this equation, $\Gamma(t)^{\text{com}} = \Gamma(t)\ a^3(t)$, we obtain

$$\frac{dn}{dt} + 3Hn = -\Gamma, \tag{3.5}$$

where we dropped the explicit time dependence of the variables. We see that the qualitative behavior of $n(t)$ is defined by whether the DM interaction rate is larger than the expansion rate H or vice versa:

1. If $\Gamma \gg H$, particles actively interact, maintaining equilibrium.

2. If $\Gamma \ll H$, the distance between particles increases so fast that they do not have enough time to find each other and thus, to interact. The particles are then out of equilibrium.

During the freeze-out, the system moves from the state 1 to the state 2. This is possible only if $\Gamma(t)$ decreases with time (increases with temperature) faster than $H(t)$. The moment at which $\Gamma(t) = H(t)$ is called the decoupling moment. In the case chemical and kinetic decouplings happen at different times, the rate of number changing processes, $\Gamma_{\#}(t)$, should be compared with the Hubble rate.

Boltzmann treatment

Let us now dive deeper into the calculations of the DM relic abundance by considering an annihilation process $1 + 2 \to 3 + 4$ with two DM particles, χ, in the initial state and two SM particles, f, in the final state. We rewrite the Equation (3.5) in a more convenient form,

$$\frac{1}{a^3}\frac{d(na^3)}{dt} = -\Gamma. \tag{3.6}$$

To find the explicit form of the interaction rate Γ, we would like to introduce the phase-space distribution function of particle i, $f_i(p,t)$, as

$$n_i(t) = \frac{g_i}{(2\pi)^3}\int d^3p_i f_i(p,t), \tag{3.7}$$

where g_i is the number of internal degrees of freedom (d.o.f) of particle i and p is the absolute value of its 3D momentum. The interaction rate is defined as (for details see [94] and the references therein)

$$\Gamma = \sum_{spins}\int d\Pi_1...\Pi_4(2\pi)^4\delta^4(p_1+p_2-p_3-p_4)[f_1f_2(1\pm f_3)(1\pm f_4)|\mathcal{M}_{12\to34}|^2 \\ - f_3f_4(1\pm f_1)(1\pm f_2)|\mathcal{M}_{34\to12}|^2], \tag{3.8}$$

where $|\mathcal{M}_{ij\to kl}|^2$ is the matrix element of the process $i+j\to k+l$, the $+$ $(-)$ signs in the statistical factors $(1\pm f_i)$ correspond to bosons (fermions), $d\Pi_i = d^3p_i/[(2\pi)^3 2E_i]$ is the Lorenz-invariant phase space measure and the sum goes over the spin states of both initial and final states. To simplify Equation (3.8), we will make futher assumptions:

Assumption 4. *The considered process is CP-invariant (i.e. T-invariant). Hence,* $\mathcal{M}_{12\to34} = \mathcal{M}_{34\to12} = \mathcal{M}$.

Assumption 5. *The SM particles are in equilibrium at the moment of DM decoupling, thus their distribution functions are known:* $f_3f_4 = f_3^{eq}f_4^{eq}$.

Assumption 6. *Detailed balance: when the considered process is in equilibrium, its rates in the forward and the backward directions are equal,* $\Gamma^{eq}_{12\to34}(T) = \Gamma^{eq}_{34\to12}(T)$. *This means that in equilibrium, at some fixed temperature T,* $f_1^{eq}f_2^{eq} = f_3^{eq}f_4^{eq}$.

With these assumptions we can rewrite Equation (3.8) as

$$\Gamma = \sum_{spins}\int d\Pi_1...\Pi_4(2\pi)^4\delta^4(p_1+p_2-p_3-p_4)|\mathcal{M}|^2[f_1f_2 - f_1^{eq}f_2^{eq}], \tag{3.9}$$

where we also used Assumption (2) to neglect the statistical factors which allowed us to factor-out the integration over the initial and final states. Let us define two more quantities, the cross section σ and the Møller velocity $v_{\text{Møll}}$,

$$\sigma : \sum_{spins}\int d\Pi_1\Pi_4(2\pi)^4\delta^4(p_1+p_2-p_3-p_4)|\mathcal{M}|^2 = 4g_1g_2\sigma\sqrt{(p_1p_2)^2 - m_1^2m_2^2}, \tag{3.10}$$

$$v_{\text{Møll}} = \frac{\sqrt{(p_1p_2)^2 - m_1^2m_2^2}}{E_1E_2}, \tag{3.11}$$

where E_i is the energy of particle i[2]. The interaction rate then becomes

$$\Gamma = \int \sigma v_{\text{M}\o\text{ll}} (dn_1 dn_2 - dn_1^{eq} dn_2^{eq}). \tag{3.12}$$

It is important to mention that the simplicity of the equation above strongly relies on the assumption of cold nature of DM. In general case, the factorization of integrals over initial an final states does not take place and the description of the system's evolution in terms of number densities n_i in meaningless. This might happen, for example, if DM particles have already departed form thermal equilibrium at the moment of chemical decoupling. In this cases, the nonintegrated Boltzmann equation for distribution function $f_{\text{DM}}(p,t)$ must be solved (see, e.g. [96, 97]). Putting this potential problem aside for now (we would bring this question back in Chapter 4), let us make one more assumption:

Assumption 7. *: $\sigma v_{M\o ll}$ does not depend strongly on $n_{1/2}$. Therefore, we can factor it out from the integral and replace by the average value*

$$\langle \sigma v_{M\o ll} \rangle = \frac{\int \sigma v_{M\o ll}\, dn_1^{eq} dn_2^{eq}}{\int dn_1^{eq} dn_2^{eq}}. \tag{3.13}$$

The DM number density evolution equation 3.6 then simplifies to

$$\frac{1}{a^3}\frac{d(na^3)}{dt} = -\langle \sigma v_{\text{M}\o\text{ll}} \rangle (n^2 - n_{eq}^2), \tag{3.14}$$

where we used the fact that the incoming particles are indistinguishable $n_1^{eq} = n_2^{eq} = n_{\text{eq}}$ and absorbed the corresponding symmetry factor in the definition of σ.

To analyze this equation, let us eliminate the dependence on the Universe's expansion by changing to comoving coordinates. To do so, we introduce the entropy of our system $S = \text{const}$ which is conserved since there is no heat flow from/to the system. The entropy density then behaves as $s = S/a^3$ (see [59] for derivation) so the fraction $Y = n/s$ does not depend on the scale factor a. Finally, we make the last assumption that is dictated by our will to create DM well before structure formation:

Assumption 8. *DM is created during the radiation domination epoch.*

We can then use the explicit expression for the Hubble parameter in terms of temperature,

$$H(t) = \frac{1}{2t} = \frac{T^2}{M_{\text{Pl}}^*}, \tag{3.15}$$

where $M_{\text{Pl}}^* = M_{\text{Pl}}/(1.66\sqrt{g^*})$, M_{Pl} is the Plank Mass and g^* is the effective number of relativistic degrees of freedom. Plugging it in Equation (3.14) and rewriting the latter in

[2]Note that $v_{\text{M}\o\text{ll}}$ has no physical meaning in general case, and it is not the relative velocity of particles 1 and 2. However, it is a dimension-less quantity defined such that $v_{\text{M}\o\text{ll}}\, n_1 n_2$ is Lorentz-invariant. It indeed coincides with the relative velocity in the rest frame of one of the colliding particles, $v_{\text{M}\o\text{ll}}\, n_1 n_2 = v_{\text{rel}}^{\text{rest}} n_1 n_2$, hence the confusion. For an exhaustive discussion, see [95].

the new coordinates, we obtain

$$\frac{dY}{dx} = -\frac{Y_{\rm eq}}{x}\frac{\Gamma_{eq}}{H}\left(\frac{Y^2}{Y_{eq}^2} - 1\right), \tag{3.16}$$

where $x = m_{\rm DM}/T$ and $\Gamma_{eq} = n_{\rm eq}\langle\sigma v\rangle$. This equation confirms the intuitive picture we drew at the beginning of this section. We see that at a given temperature we can judge whether DM is in equilibrium or not by comparing its equilibrium interaction rate with the Hubble rate:

$$\frac{\Gamma_{eq}}{H} \gg 1: \; Y = Y_{eq}, \tag{3.17}$$

$$\frac{\Gamma_{eq}}{H} \ll 1: \; Y = const. \tag{3.18}$$

The transition between these two regimes (i.e. decoupling) happens at

$$\frac{\Gamma_{eq}}{H} \sim \frac{x_{\rm dec}}{Y_{eq}} \sim x_{\rm dec}\frac{n_{eq}}{s_{eq}} \sim O(1)x_{\rm dec} \sim 20, \tag{3.19}$$

where we used the fact that $n_{eq} \propto s_{eq} \propto a^{-3}$ and took the typical value of the ratio x_{dec} at the moment of decoupling [98]. The energy density of DM is related to Y simply as

$$\Omega_{\rm DM} = m_{\rm DM} n_{\rm DM}. \tag{3.20}$$

In Figure 3.2, we show the evolution of $Y(x)$. We see that while being in equilibruim, Y decreases exponentially, reaching a constant value after decoupling. Due to the steepness of the exponential, $x_{\rm dec}$ is almost insensitive to the interactions strength $\langle\sigma v\rangle$. The situation is, hovewer, very different for Y: *the stronger the interaction, the longer DM is in equilibrium resulting in smaller values of DM relic abundance*[3].

We conclude that accurate measurement of $\Omega_{\rm DM}$ by Planck Collaboration [17] provides a very powerful tool for testing DM models with exponential sensitivity to the DM decoupling cross section.

3.2. Testability of dark matter models

In this section, we would like to give the reader an insight into how a typical thermal DM model can be tested. In Section 1.1 and Section 2.3 we discussed the cosmological and astrophysical evidence of DM and the ways to detect DM particles. To date, no new particles were found. The results can therefore be used to put (in many cases severe) constraints on the potential particle-physics models of DM.

[3] Interestingly, in the case of the freeze-in production mechanism, the opposite takes place: the larger the interaction strength, the more DM is produced [99].

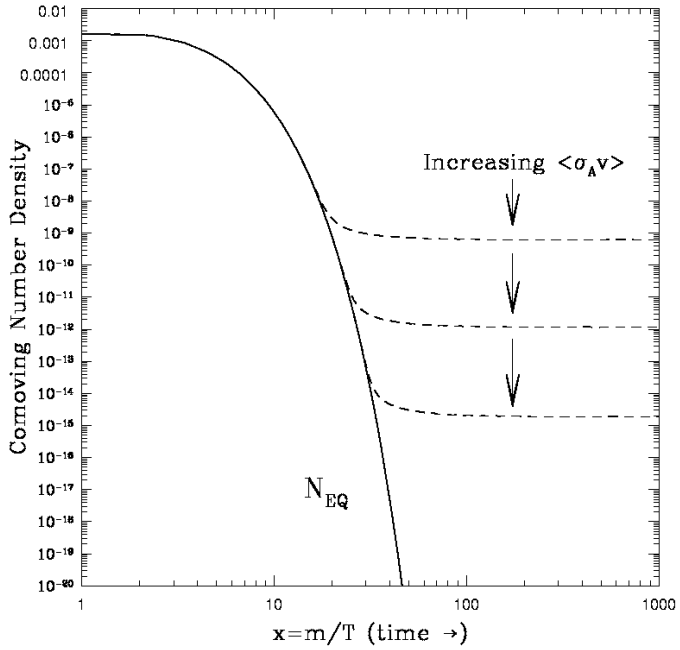

Figure 3.2: Evolution of the comoving number density Y of a DM particle during the freeze-out process with time (inverse temperature). In equilibrium, this quantity drops exponentially with x, $Y_{\rm eq} \propto \exp(-x)$. After freeze-out, it becomes constant. The net amount of DM density decreases with the increase of the annihilation cross section (labelled as $\langle \sigma_A v \rangle$).
Image credit: Dan Hooper, TASI 2008 Lectures on dark matter

In minimalistic[4] models, the processes responsible for DM production in the Early Universe are related to the ones tested at DM experiments at present (see Section 2.3). Let us give an extreme example of a model with only one new particle that couples to the SM through only one portal with the coupling strength α. In this case, all the experiments are testing this one coupling in the ways shown in Figure 3.3. Notice that in the case of only one new particle, indirect detection searches rely on the same annihilation processes that set the DM relic abundance (with the remark that in the former case we might be interested in a subset of all the possible annihilation reactions). In a more general case, different couplings might be responsible for different processes from Figure 3.3. However, frequently, the couplings are interconnected and/or correlated with the mass spectrum of the dark sector (see, e.g. Chapter 4), making the combination of the tests described here quite constraining for many minimal models. This leads to a common procedure for testing new DM models: they first should account for the correct relic density and evade the direct/indirect detection constraints, the remaining part of the parameter space (varying from a very small window to quite large areas depending on the model) can be tested at colliders. In the next section, we will discuss how this procedure leads to ruling out the simplest models, and which main directions in minimalistic model building are on the market.

[4]In this work, we would use the term "minimalistic" referring to models with a minimal number of new parameters/degrees of freedom.

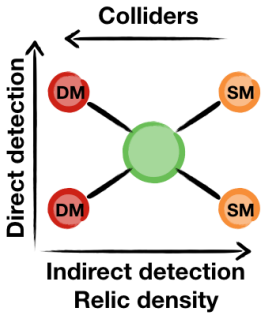

Figure 3.3: The ways simple DM models are tested. In minimalistic models, all the searches test the same DM-SM coupling.

3.3. Issues with simple WIMPs and ways out

It appears that the single-particle model described in the previous section is, in general, overconstrained. Let us assume that DM is much heavier than the other particles that take part in the annihilation process from Figure 3.3. From the dimension analysis, we can then estimate the DM annihilation cross section as

$$\langle \sigma v_{\text{Møll}} \rangle_{\text{ann}} \propto \frac{\alpha^2}{m_{\text{DM}}^2}. \tag{3.21}$$

Interestingly, by assuming a DM coupling of the order of the electroweak gauge couplings and $m_{\text{DM}} = O(200-1000)$ GeV, using Equation (3.20) we would arrive at a DM relic density of the order of the Planck measurements[5]. This phenomenon is called *the WIMP miracle* and in the past, it has triggered searches for BSM particles of the electroweak scale at the LHC (see [100] for a review). It turned out, however, that no traces of new physics at both collider and direct detection experiments restrict the parameter space of the most simple WIMP models such that they can not account for the correct DM relic abundance.

The reason is the interplay of direct detection and the relic density measurements. The former puts very strong *upper limits* on α, see Figure 2.4. However, very small couplings cause tiny interactions of DM in the Early Universe. Consequently, this leads to its decoupling at earlier times, and thus to the *overabundance* of DM, see Figure 3.2. This pattern is nicely illustrated in Figure 3.4 on the example of a simple scalar Higgs portal extension of the SM. We can see that small couplings are excluded due to DM overproduction, whether larger couplings are excluded by the direct detection experiments (LUX and XENON1T in this case). We observe a typical for the WIMP models picture when most of the parameter space is excluded, except for a small window around $m_S = m_h/2$ which is often referred to as *the Higgs resonance region*. It is characterized by a rapid enhancement of the s-channel Higgs-mediated cross sections which results in smaller couplings needed to provide the correct relic abundance. In addition to the scalar model, Ref. [101] studies vector and singlet fermionic extensions of the SM finding similar patterns (except for the fermionic case with

[5]Strictly speaking, at the lower edge of the mass range discussed $\langle \sigma v_{\text{Møll}} \rangle_{\text{ann}}$ gets sizeable corrections from the non-negligible masses of gauge bosons.

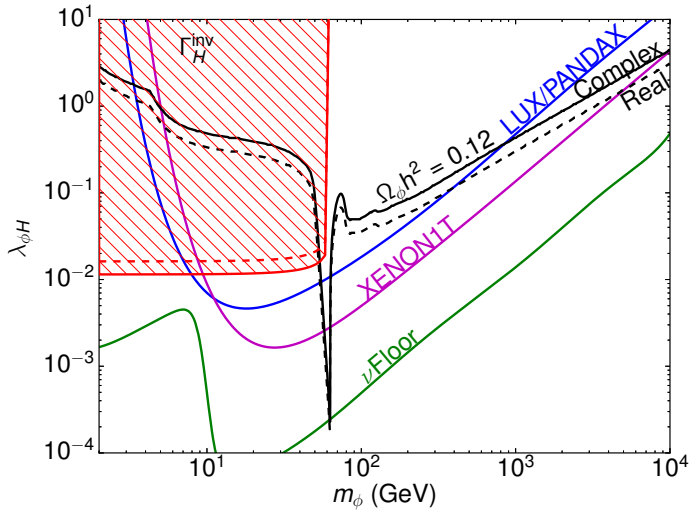

Figure 3.4: Constraints on the mass and coupling of the single-field scalar Higgs portal DM extension of the SM [101]. Exclusion limits are set by the DM overabundance (below the black lines), direct detection experiments (above the purple and blue lines) and invisible Higgs width (red hatched area). Solid (dashed) curves correspond to the complex (real) scalar.

the pseudoscalar DM-Higgs coupling, see also [102]).

In the case of pure higher fermionic electroweak multiplets, the correct relic density is achieved at DM masses above the TeV scale. The main constraint for such candidates comes from indirect detection searches. The allowed parameter space typically lies outside the current LHC reach. As an example, in the left panel of Figure 3.5, we provide the current constraints on the parameters of the BSM fermionic doublet and triplet DM candidates in the context of Supersymmetric models. We also demonstrate the importance of the Sommerfeld enhancement effect for relic abundance prediction in such models on the example of the fermionic quintuplet DM (see the right panel of Figure 3.5).

We conclude that simple WIMPs are either very constrained by direct detection measurements or are too massive to be produced at the LHC. However, some recipes allow for the thermal DM with the masses and couplings testable at current colliders.

In this section, we will discuss the most popular scenarios of this kind. In Chapter 4, we will introduce one more way to naturally obtain an experimentally appealing DM theory.

WIMPless miracle

This scenario relies on the observation that the DM relic density is not, in fact, set by the individual values of the DM mass and coupling, but rather by their ratio (see Equation (3.21)). This means that smaller couplings, required by the direct detection constraints, suggest smaller DM masses (as long as the estimate Equation (3.21) is valid). One example of such models was provided in [103]. The authors suggested a scenario in which DM lies in the hidden sector of a supersymmetric model. They suggested a symmetry-breaking mechanism

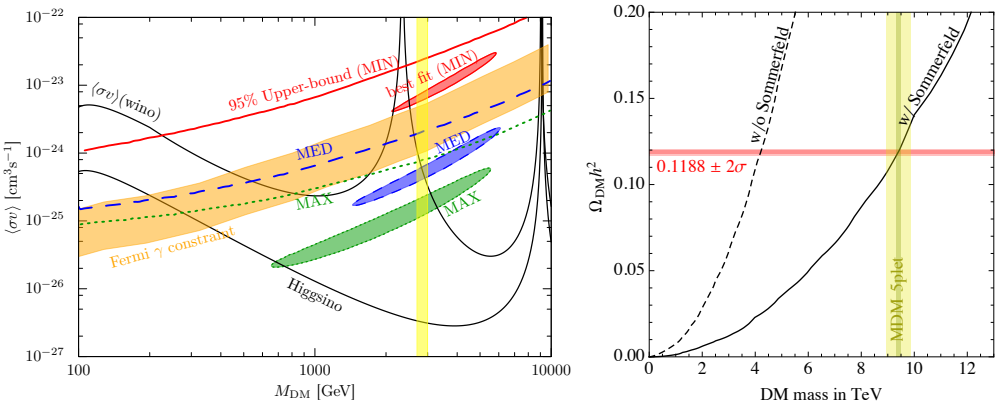

Figure 3.5: Left: correct relic abundance (black lines) and indirect detection constraints on the fermionic doublet (higgsino) and triplet (wino) SUSY DM candidates [105]. Right: Correct relic abundance calculated with and without the Sommerfeld effect for the quintuplet DM candidate [106].

that ensures the following relation

$$\frac{\alpha_{\rm DM}}{m_{\rm DM}} = \frac{\alpha_{\rm EW}}{m_{\rm EW}}. \tag{3.22}$$

and allows for DM masses different from the weak scale. Here $\alpha_{\rm DM\ (EW)}$ and $m_{\rm DM\ (EW)}$ are correspondingly the DM (electroweak) coupling and mass.

The next three scenarios are sometimes called "the three exceptions to thermal DM" following the name of the first paper [104] in which all they were brought together.

Forbidden dark matter

The main idea behind this scenario is that in the primordial plasma DM annihilations to heavier mediators ($m_{\rm DM} < m_{\rm M}$) are possible when the DM particles come from the high-energetic tail of the thermal distribution (see Figure 3.6, left panel). The resulting cross section is exponentially (or Boltzmann) suppressed, allowing for correct DM relic abundance at larger coupling/mass ratios. For example, in the case of fermionic DM and a dark photon acting as a mediator [107], the annihilation cross section at temperature T reads

$$\langle\sigma v_{\rm M\o ll}\rangle_{\rm ann} \sim \frac{\alpha_{\rm DM}^2}{m_{\rm DM}^2} e^{-2(m_{\rm M}-m_{\rm DM})/T}. \tag{3.23}$$

At a given DM mass, $\alpha_{\rm DM}$ can be large enough to cause DM self-interactions resulting in additional constraints on this model. However, this scenario opens up a feasible part of parameter space in the experimentally interesting region of moderate DM masses and couplings.

Resonant production

In this class of models, the DM annihilation cross section is resonantly enhanced due to DM mass being exactly half the mass of the s-channel mediator (see Figure 3.6, middle panel). This allows for the correct DM relic abundance at small DM couplings, therefore evading direct detection constraints [108]. Importantly, the allowed couplings may be so

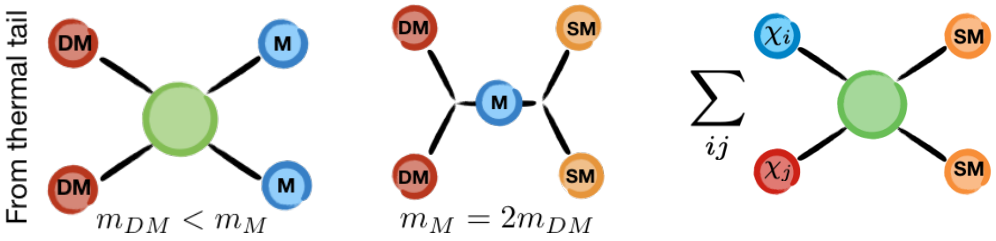

Figure 3.6: The three exceptions to the thermal dark matter: forbidden DM (left), resonant production (middle) and co-annihilation (right).

small that DM is not in thermal equilibrium at the moment of decoupling. This means that the procedure described in Section 3.1 should be reconsidered. Non-thermal effects are so strong that they lead to $\Omega_{\rm DM}$ being up to ten times larger than if thermal equilibrium is assumed [97].

Co-annihilation

Let us add one important comment to our relic density vs. direct detection discussion. The former observation tells us how actively DM was interacting *at the moment of decoupling*, whereas the latter gives information about its interactions *today*. The question arising is: is it possible to increase the effective DM interaction cross section $\sigma^{\rm eff}_{\rm DM}$ at early times without affecting its present values?

One of the most straightforward ways to do so is to increase the number of annihilation channels at the moment of decoupling by introducing more dark sector particles (see Figure 3.6, right panel). In addition to the discussed annihilation, the DM number density can be changed by the *co-annihilation* processes. The DM evolution equation Equation (3.14) then modifies to [104]

$$\frac{1}{a^3}\frac{d(na^3)}{dt} = -\sum_{i,j}\langle\sigma_{ij}v\rangle(n_i n_j - n_i^{\rm eq} n_j^{\rm eq}), \tag{3.24}$$

where σ_{ij} denotes the co-annihilation cross section of i and j dark states and $n = \sum n_i$ is the total number of the dark sector particles. In the above, we shortened our notation using $v_{\rm Møll} = v$. The present DM-SM interactions remain unchanged as long as all the heavier dark states have decayed to DM by the present time (or their density is negligible). Let us rewrite Equation (3.25) to extract the effective cross section:

$$\frac{1}{a^3}\frac{d(na^3)}{dt} = -\sum_{i,j}\langle\sigma_{\rm eff}v\rangle(n^2 - n_{\rm eq}^2), \tag{3.25}$$

where

$$\langle\sigma_{\rm eff}v\rangle = \sum_{ij}\sigma_{ij}\frac{g_i g_j}{g_{\rm eff}^2}(1+\Delta_i)^{3/2}(1+\Delta_j)^{3/2}e^{-x(\Delta_i+\Delta_j)} \tag{3.26}$$

and g_i is again the number of internal degrees of freedom of i particle, $\Delta_i = (m_i - m_{\rm DM})/m_{\rm DM}$ and $g_{\rm eff} = \sum g_i(1+\Delta_i)^{3/2}\exp(-x\Delta_i)$.

We will consider a model that features co-annihilation in Chapter 4. In addition, we will introduce yet another way of DM production – *the co-scattering mechanism*. The latter has not yet gotten much attention in the DM community. However, we argue that it is as general and phenomenologically important as the scenarios listed in this chapter.

4. Long-lived electroweak-scale dark sectors

Since all the SM particles were created thermally, we will proceed to explore this mechanism of particle production in the context of electroweak-scale DM. As discussed in Chapter 3, the combined results of existing DM searches suggest that thermal DM in the mass range accessible at current experiments was most likely produced through a complicated process that involved more than one BSM particle. We would also keep our model as minimal as possible in terms of new degrees of freedom. Our main goal is to predict new signatures that are testable at existing colliders, using the knowledge of the DM properties and taking into account combined constraints on new physics. Motivated by the extensive program of measuring the Higgs boson properties at the LHC [109], we focus here on the Higgs-portal DM scenarios. We also constrain ourselves to fermionic DM candidates.

The contents of this chapter and the related Appendices A and B is based on research in collaboration with Susanne Westhoff (Heidelberg University) and published in [110]. Most of the results as well as a significant part of the text are taken from the corresponding publication. The content of Section 4.7 is based on the work in progress with Abanti Ranadhir Sahasransu and Freya Blekman (Vrije Universiteit Brussel), Nishita Desai (TIFR, Mumbai) and Susanne Westhoff.

4.1. Introduction

Higgs-portal scenarios are on the DM market for a long time (see the introduction and a simple example of a Higgs portal model in Section 2.1). We already mentioned the challenges of single-field extensions of the SM in Section 3.3. The natural next step is to add a second dark field to the model in a renormalizable way, and thus, to disentangle DM production from its role in direct/indirect detection experiments. Such models where studied in the context of different electroweak n-plet field combinations with $n = [1, 4]$ [111–115]. We would like to add a "missing piece" to this list by considering the singlet-triplet scenario that has not been studied in great detail before[1]. It appears that this scenario has a very interesting phenomenology. In addition, it can serve as a toy model for various Early Universe processes, as well as for interesting collider signatures. Another appealing feature of this model is the naturally small DM-SM coupling, a necessary feature to survive the direct detection constraints (this argument is however purely aesthetical and should not serve as a guiding principle for model building).

We perform a comprehensive analysis of long-lived mediators at the LHC in the singlet-

[1] We will comment on the previous works, including the ones in the SUSY context, later in this chapter.

triplet model. Existing searches for disappearing charged tracks and displaced hard leptons already exclude tiny portal couplings that cannot be probed by current direct and indirect detection experiments. For larger portal couplings, we predict new signatures with displaced soft leptons, which are accessible with run-II data. Displaced searches are expected to probe mediators with masses up to the TeV scale, which is well beyond the sensitivity of prompt searches. Most of the conclusions of this chapter are not specific to our model and can be generalized to various thermal multiparticle dark sectors.

4.2. The singlet-triplet model

We extend the SM by two self-adjoint fermion fields with vector-like weak interactions,

$$\chi_S = \chi_S^0, \qquad \chi_T = \begin{pmatrix} \chi_T^0/\sqrt{2} & \chi^+ \\ \chi^- & -\chi_T^0/\sqrt{2} \end{pmatrix}. \tag{4.1}$$

Here χ_S is a Majorana singlet and χ_T transforms under the weak gauge group as a triplet with zero hypercharge[2]. We assume a discrete $\mathbb{Z}_2$ symmetry, under which χ_S and χ_T are odd and all standard-model particles are even. The lightest fermion state plays the role of DM. The Higgs portal interaction of the new fields can be realized only through nonrenormalizable interactions. At energies below a cutoff scale Λ, the scalar sector is described by the effective Lagrangian

$$\begin{aligned} \mathcal{L}_{\text{eff}} = \overline{\chi}_S i\partial\!\!\!/\, \chi_S + \text{Tr}[\overline{\chi}_T i\partial\!\!\!/\, \chi_T] - \Big(\frac{m_S}{2}\overline{\chi}_S\chi_S^c + \frac{m_T}{2}\text{Tr}[\overline{\chi}_T\chi_T^c] + h.c.\Big) \\ +\Big(\frac{\kappa_{ST}}{\Lambda}(H^\dagger\overline{\chi}_T H)\chi_S^c - \frac{\kappa_S}{\Lambda}H^\dagger H\,\overline{\chi}_S\chi_S^c - \frac{\kappa_T}{\Lambda}H^\dagger H\,\text{Tr}[\overline{\chi}_T\chi_T^c] + h.c.\Big) \\ +\Big[\frac{\kappa_T'}{\Lambda}\Big(H^\dagger\overline{\chi}_T\chi_T^c H - \text{Tr}[\overline{\chi}_T H H^\dagger\chi_T^c]\Big) + h.c.\Big], \end{aligned} \tag{4.2}$$

where $D_\mu = \partial_\mu - ig\,\tau^a W_\mu^a$ is the covariant derivative, τ^a are the generators of the weak SU(2) gauge group and $H = (h^+, (v+h+i\eta)/\sqrt{2})^\top$ is the Higgs boson. Here we use a chiral 4-component representation of the fermion fields (such that $\chi_{S/T} = (\chi_{S/T}^L, 0)^\top$, where $\chi_{S/T}^L$ is the 2-component spinor of left chirality) and $\chi_{S/T}^c$ denotes the charged conjugated fields. The singlet-triplet effective interaction is of mass dimension five and thus is naturally suppressed by the scale $\Lambda \gg M_W$. We neglect the higher-dimension operators assuming that they are even more suppressed by the cutoff scale. We also assume all parameters to be real in order to preserve CP invariance. The couplings κ_S, κ_T and κ_T' do not affect our phenomenological analysis so we neglect them by setting $\kappa_S = \kappa_T = \kappa_T' = 0$. We, however, refer an interested reader to the works that study the DM and collider phenomenology of these coupling [116–119].

[2]The main motivation for choosing Majorana fields is smaller direct detection signal due to absence of Z-mediated processes.

UV completions of the singlet-triplet Higgs portal

The scenario proposed is an example of EFTs discussed in Section 2.1. As mentioned above, our model assumes that the complete self-consistent and renormalizable theory is resolved at energies of the order of Λ. We do not specify any completions here since they would not affect the "low-energy" phenomenology of the model at the LHC scales [3]. However, it is instructive to verify the existence of such completions by providing examples.

One of the ways to build a renormalzable realization of the Lagrangian in Equation (4.2) is by introducing an additional electroweak fermion doublet χ_D. This construction is well known in context of supersymmetry (see, e.g. [120]). The singlet-triplet interaction then originates from

$$\mathcal{L}_{\rm UV} = -y_1 \overline{\chi}_D \chi_S^c H - y_2 \overline{\chi}_D \chi_T^c H + h.c., \tag{4.3}$$

where $y_{1/2}$ are dimensionless couplings. The original singlet-triplet mixing term can be obtained by integrating out the new doublet. The suppression scale Λ is hence associated with its mass m_D:

$$\frac{\kappa_{\rm ST}}{\Lambda} = -\frac{y_1 y_2}{2 m_D}. \tag{4.4}$$

Another UV completion of our theory involves an additional scalar triplet. In this case, however, only the couplings κ_S or κ_T can be generated, so we will not dive into the calculations. Such scenarios are widely discussed in the context of type-II seesaw models (see, e.g. [121]).

Going to mass basis

After EWSB, the scalar Lagrangian for the neutral states $\chi_S^0 \equiv \chi_S$ and χ_T^0 becomes

$$\begin{aligned} \mathcal{L}_{\rm S} = &-\frac{m_S}{2}\overline{\chi}_S^0 (\chi_S^0)^c - \frac{m_T}{2}\overline{\chi}_T^0 (\chi_T^0)^c \\ &- \frac{\mu}{2}\Big(1 + \frac{2h}{v} + \frac{h^2}{v^2}\Big)\left[\overline{\chi}_T^0 (\chi_S^0)^c + \overline{\chi}_S^0 (\chi_T^0)^c\right] + h.c., \end{aligned} \tag{4.5}$$

where $\mu = \kappa_{ST} v^2/(\sqrt{2}\Lambda)$. The charged states are not affected by the mixing and remain the same in the mass basis. For the neutral states, we define the mass Lagrangian as

$$\mathcal{L}_{\rm mass} = -\frac{1}{2} M_{ij} \overline{\Psi}_i \Psi_j^c + h.c., \quad M = \begin{pmatrix} m_S & \mu \\ \mu & m_T \end{pmatrix}, \quad \Psi = \begin{pmatrix} \chi_S^0 \\ \chi_T^0 \end{pmatrix}, \tag{4.6}$$

where M is the mass matrix. The physical eigenstates χ_ℓ and χ_h can be obtained by

[3] Of course, if Λ is close to the energies reached at experiments, the integrated-out states start affecting the observed physics (see [113] as an example of UV-complete models with relatively light mediators that affect dark sectors' collider phenomenology). The scale separation requirement determines the validity range of an effective theory.

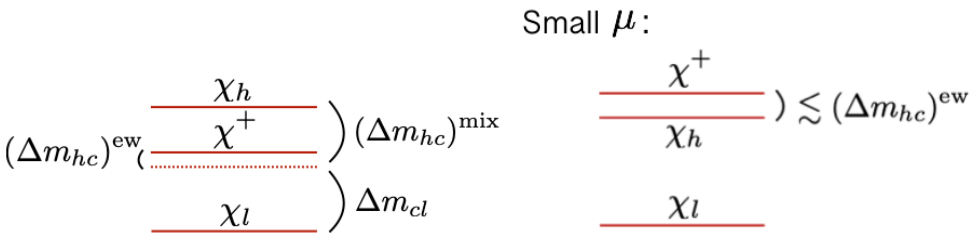

Figure 4.1: The mass spectrum of dark sector fermions in the singlet-triplet model. Left: "normal" mass hierarchy, realized at sizeable portal coupling. Right: "inverted" mass hierarchy that takes place at very small portal coupling.

diagolizing the matrix M with

$$\begin{pmatrix} \chi_\ell \\ \chi_h \end{pmatrix} = \begin{pmatrix} \cos\theta\,\chi_S^0 - \sin\theta\,\chi_T^0 \\ \sin\theta\,\chi_S^0 + \cos\theta\,\chi_T^0 \end{pmatrix}, \quad \tan(2\theta) = \frac{2\mu}{m_T - m_S}, \quad 0 < \theta < \frac{\pi}{4}. \tag{4.7}$$

The corresponding mass eigenvalues for the neutral states χ_ℓ, χ_h and the charged states $\chi^\pm$ are

$$m_{h,\ell} = \frac{1}{2}\Big(m_T + m_S \pm \Delta m_{h\ell}\Big), \quad \Delta m_{h\ell} = \sqrt{(m_T - m_S)^2 + 4\mu^2}, \quad m_c = m_T. \tag{4.8}$$

The light neutral state χ_l is the DM candidate. The mass spectrum of the dark sector is illustrated in Figure 4.1. The left panel shows the tree-level structure of Equation (4.8). The corresponding mass splittings are denoted as Δm_{cl} and $(\Delta m_{hc})^{\rm mix}$. In addition, loop corrections to the triplet eigenstates lead to a relative upper shift of the χ^+ mass $(\Delta m_{hc})^{\rm ew} \approx 160$ MeV [122]. This shift is independent of the singlet-triplet coupling, meaning that for very small values of μ it can offset the tree-level splitting between χ^+ and χ_h leading to the inverted spectrum (see the right panel of Figure 4.1).

Using the freedom of field definitions, we can always rotate $\chi_{S/T}$ in Equation (4.5) by appropriate complex phases to make m_T and μ positive. The sign of m_S remains a free parameter. Depending on the value of the latter, we can distinguish between two physical scenarios which we call *the scalar* and *the pseudo-scalar* scenarios. They are characterized by different diagonalization procedures that lead to positively defined mass eigenvalues. Consequently, the couplings of new physics to the SM bosons are different in the two cases. Below, we provide the final result of the diagonalization calculations, the details of which can be found in Appendix A.2.

Scalar scenario

For $m_S > \mu^2/m_T$, the mass m_ℓ of the lightest state is positive. The physical Lagrangian

then reads (neglecting interactions with two Higgs bosons)

$$\begin{aligned}\widehat{\mathcal{L}}_S =& -\frac{m_\ell}{2}\,\overline{\chi}_\ell(\chi_\ell)^c - \frac{m_h}{2}\,\overline{\chi}_h(\chi_h)^c + h.c \\ &- \frac{\mu}{v}h\Big[\cos(2\theta)\big(\overline{\chi}_\ell(\chi_h)^c + \overline{\chi}_h(\chi_\ell)^c\big) + \sin(2\theta)\big(-\overline{\chi}_\ell(\chi_\ell)^c + \overline{\chi}_h(\chi_h)^c\big)\Big] + h.c. \\ &+ g\,W^+_\mu\Big[-\sin\theta\left(\overline{\chi}_\ell\gamma^\mu\chi^- - \overline{\chi^+}\gamma^\mu\chi_\ell\right) + \cos\theta\left(\overline{\chi}_h\gamma^\mu\chi^- - \overline{\chi^+}\gamma^\mu\chi_h\right)\Big] + h.c. \\ &+ g\,(\cos\theta_w Z_\mu - \sin\theta_w A_\mu)\left[\overline{\chi^+}\gamma^\mu\chi^+ - \overline{\chi^-}\gamma^\mu\chi^-\right],\end{aligned} \tag{4.9}$$

where θ_w denotes the Weinberg angle. The DM candidate couples to the SM bosons through scalar/vector couplings. As mentioned above, due to the Majorana nature of new fermions, the interaction of χ_ℓ, χ_h with the Z-boson is absent. In the limit of small mixing, the lightest state is an almost pure singlet with suppressed couplings to the SM. This is precisely the limit of our interest since in the opposite case the triplet-like state is the lightest. It can be a viable DM candidate only in the mass region above the reach of the LHC (see, e.g [105]).

Pseudo-scalar scenario

A pseudo-scalar singlet-triplet Higgs portal can be obtained through a chiral rotation of the singlet fermion,

$$\chi_S \to \exp(i\gamma_5\pi/2)\,\chi_S. \tag{4.10}$$

By applying this transformation to the Lagrangian in Equation (4.5), we obtain

$$\begin{aligned}\mathcal{L}_{\rm P} =& \frac{m_S}{2}\overline{\chi}^0_S(\chi^0_S)^c - \frac{m_T}{2}\overline{\chi}^0_T(\chi^0_T)^c \\ &- \frac{\mu}{2}\Big(1 + \frac{2h}{v} + \frac{h^2}{v^2}\Big)\left[-\overline{\chi}^0_T i\gamma_5(\chi^0_S)^c + \overline{\chi}^0_S i\gamma_5(\chi^0_T)^c\right] + h.c.,\end{aligned} \tag{4.11}$$

In the case of $m_S < \mu^2/m_T$, in order to obtain positive m_ℓ, one needs to diagonalize the Lagrangian in Equation (4.6) by the following rotation (see Appendix A.2 for details)

$$\begin{pmatrix}\chi_\ell \\ \chi_h\end{pmatrix} = \begin{pmatrix}\cos\theta\,\chi^0_S + \sin\theta\,i\gamma_5\chi^0_T \\ \sin\theta\,i\gamma_5\chi^0_S + \cos\theta\,\chi^0_T\end{pmatrix}, \quad \tan(2\theta) = \frac{2\mu}{m_T - |m_S|} \tag{4.12}$$

where θ is defined as in Equation (4.7). The resulting physical Lagrangian reads

$$\begin{aligned}\widehat{\mathcal{L}}_P =& -\frac{m'_\ell}{2}\,\overline{\chi}_\ell(\chi_\ell)^c - \frac{m'_h}{2}\,\overline{\chi}_h(\chi_h)^c + h.c. \\ &- \frac{\mu}{v}h\Big[\cos(2\theta)\big(\overline{\chi}_\ell i\gamma_5(\chi_h)^c + \overline{\chi}_h i\gamma_5(\chi_\ell)^c\big) + \sin(2\theta)\big(\overline{\chi}_\ell(\chi_\ell)^c + \overline{\chi}_h(\chi_h)^c\big)\Big] + h.c. \\ &+ g\,W^+_\mu\Big[\sin\theta\left(\overline{\chi}_\ell\,i\gamma^\mu\gamma_5\chi^- + \overline{\chi^+}i\gamma^\mu\gamma_5\chi_\ell\right) + \cos\theta\left(\overline{\chi}_h\gamma^\mu\chi^- - \overline{\chi^+}\gamma^\mu\chi_h\right)\Big] + h.c. \\ &+ g\,(\cos\theta_w Z_\mu - \sin\theta_w A_\mu)\left[\overline{\chi^+}\gamma^\mu\chi^+ - \overline{\chi^-}\gamma^\mu\chi^-\right].\end{aligned} \tag{4.13}$$

In this case, χ_l couplings to the SM bosons have pseudo-scalar/axial-vector structure. The

mass eigenvalues in pseudoscalar scenario are

$$m'_{h,\ell} = \frac{1}{2}\Big(\Delta m'_{h\ell} \pm (m_T + m_S)\Big) = \pm\, m_{h,\ell}, \tag{4.14}$$

resulting in the the same spectra as in the scalar scenario, see Figure 4.1. Note that for the fixed m_T and μ the mixing angle θ is larger in the scalar case that in the pseudo-scalar one.

The chiral rotation flips the sign of the lightest mass eigenvalue in the spectrum and affects the DM couplings to Higgs/gauge bosons. The parameter space $m_S < \mu^2/m_T$ with negative mass $m_\ell < 0$ in the scalar Lagrangian $\widehat{\mathcal{L}}_S$ thus corresponds to positive mass $m'_\ell > 0$ in the pseudo-scalar Lagrangian $\widehat{\mathcal{L}}_P$.

We identify two physical scenarios,

$$\begin{aligned} \text{scalar scenario:} \quad & \widehat{\mathcal{L}}_S \text{ with } m_S > \mu^2/m_T \;\leftrightarrow\; m_\ell > 0, \\ \text{pseudo-scalar scenario:} \quad & \widehat{\mathcal{L}}_P \text{ with } m_S < \mu^2/m_T \;\leftrightarrow\; m'_\ell > 0. \end{aligned} \tag{4.15}$$

While aspects of the scalar scenario has been the focus of the majority of previous collider studies, both in context of SUSY (see, e.g. [120]) or as an effective theory (see, e.g. recent studies [123, 124]), the phenomenology of long-lived mediators in the pseudo-scalar case is still largely unexplored. In this work we perform a comprehensive study of both scenarios, pointing out numerous differences between them.

Relation to supersymmetry

The setup discussed here has been partially studied in a variety of SUSY works in the so-called *wino-bino* scenarios where bino and wino are the names of a supersymmetric fermionic triplet and singlet respectively. The UV-complete theory, in this case, is realized by adding a new fermion doublet, the higgsino, with the structure as in the Lagrangian in Equation (4.3). The singlet-triplet scenario is realized in the limit of heavy higgsinos. In the paper [110] we provide the relation between the parameters of our model and SUSY. We also highlight the parameter space of the latter that corresponds to scalar/pseudo-scalar scenarios.

The singlet-triplet model can be viewed as a generalized version of the wino-bino scenario in SUSY with completely free couplings (in SUSY, the couplings are related to one another so only the subspace of parameters is theoretically available). The scalar case of the wino-bino DM model was exhaustively discussed in the literature. The most up-to-date comprehensive study [125] states that the unexplored parameter space of the wino-bino model can only become accessible at future colliders. In our EFT approach, we find, however, interesting signatures, realizable with the current technologies at the LHC.

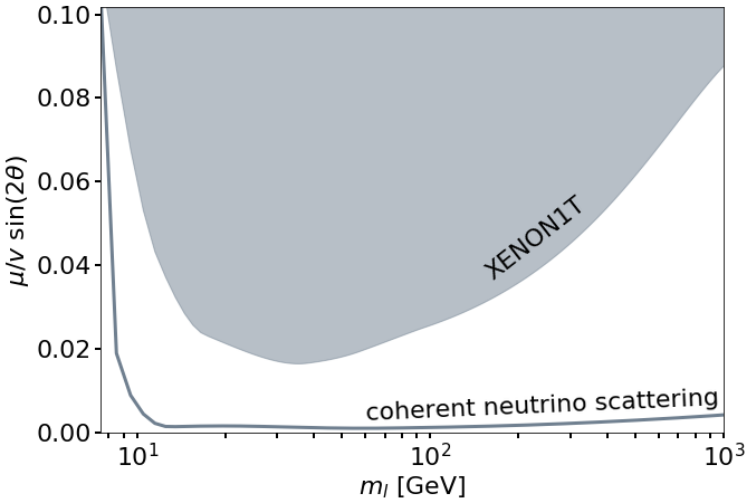

Figure 4.2: Bounds on the Higgs coupling to DM, as a function of the DM mass obtained from Xenon1T measurement [126] using `micrOMEGAs` [127]. The grey region is excluded at 90 % CL, the solid curve indicates the neutrino floor discussed in Section 2.3.

4.3. Direct detection

As discussed in Section 2.3, a DM model should be consistent with the direct detection observations. Due to Majorana nature, χ_l scatterings with atomic nuclei are mediated by the Higgs boson only, meaning that only the spin-independent part of the Lagrangian in Equation (2.10) is present,

$$\mathcal{L}_{\rm DD}^{eff} = -\,\mathcal{C}_h^q\,(\bar{\chi}_\ell \chi_\ell^c)\,(\bar{q}q) + h.c.\,, \quad \mathcal{C}_h^q = \sqrt{2}\,G_F \frac{m_q}{M_h^2}\,\mu \sin(2\theta), \tag{4.16}$$

where G_F is the Fermi constant and M_h is the Higgs mass. In Figure 4.2, we show the direct detection constraints on our model obtained from the Xenon1T measurements [126]. The calculations of direct detection signal in our model were done using `micrOMEGAs` [127]. We see that in the mass region of phenomenological interest the DM-SM coupling is tiny, thus it is useful to study the properties of our model in this limit.

Small-mixing limit

In the limit of small μ the mixing angle can be approximated as

$$\theta \approx \frac{\mu}{m_T - m_S} \ll \frac{\pi}{4}. \tag{4.17}$$

The most relevant DM couplings then read

$$W_\mu^+ \overline{\chi}_\ell\, \gamma^\mu (i\gamma_5) \chi^- \sim g\,\theta, \quad h\,\overline{\chi}_\ell \chi_\ell \sim \frac{\mu}{v}\theta, \quad h\,\overline{\chi}_\ell\,(i\gamma_5)\chi_h \sim \frac{\mu}{2v}. \tag{4.18}$$

As mentioned above, for fixed values of m_T and μ, the mixing θ in the pseudo-scalar scenario is smaller than in the scalar scenario, so are the gauge and diagonal Higgs couplings of χ_l.

The masses of the neutral fermions in this limit read

$$m_h = m'_h \approx m_T + \theta\mu, \quad m_\ell = -m'_\ell \approx m_S - \theta\mu. \tag{4.19}$$

Importantly, the mass splitting between the heavier states is the same in both scenarios and is equal to

$$\Delta m_{hc} = m_h - m_c = (\Delta m_{hc})^{\text{mix}} + (\Delta m_{hc})^{\text{ew}} \approx \frac{\mu^2}{m_T - m_S} - 160\,\text{MeV} \tag{4.20}$$

where we use the fixed value for $(\Delta m_{hc})^{\text{ew}} \approx 160$ MeV (see [122] for details). Let us compare Equation (4.20) with the coupling tested by direct detection. From Equation (4.16), we can derive that

$$\mathcal{C}_h^q \propto \mu \sin(2\theta) \simeq \frac{2\mu^2}{m_T - m_S}. \tag{4.21}$$

Thus, we conclude that direct detection requires also *small mass splitting* Δm_{hc}. The splitting between DM and the next-to-the-lightest state is fixed by the DM relic density measurements and will be discussed in detail in the next section. Here we provide the expression for $\Delta m_{cl}^{(\prime)}$ in the limit of small mixing,

$$\begin{aligned} \text{scalar scenario: } \Delta m_{c\ell} &= m_c - m_\ell \approx m_T - m_S + \frac{\mu^2}{m_T - m_S}, \\ \text{pseudo-scalar scenario: } \Delta m'_{c\ell} &= m_c - m'_\ell \approx m_T + m_S - \frac{\mu^2}{m_T - m_S}. \end{aligned} \tag{4.22}$$

4.4. Relic density and the role of co-scattering

Our model adds three new physical states to the primordial plasma: χ_l, χ^+ and χ_h. In Chapter 3, we discussed in detail the procedure of calculating the relic abundance of thermally produced DM. We also discussed the more complicated equations that arise if a larger number of dark states are involved in the decoupling process.

In Table 4.1, we list the processes that change the number of dark sector particles during freeze-out, we also indicate the scaling of the corresponding cross sections with the portal coupling μ/v and the singlet-triplet mixing angle θ. Since we aim to perform the scan over the parameter space of our theory, it is important to notice that depending on the value of μ/v and θ different processes dominate the DM production. Below we will go through the dominant processes with the *decrease* of μ/v.

Pair annihilation, co-annihilation and mediator annihilation

Let us first discuss the rather known mechanisms of DM production, referring to Figure 4.3. There, we illustrate the interplay of direct detection and relic density constraints in the plane of the DM mass m_l and mass splitting between χ_l and χ_C (as we will see below, the latter is an important quantity for co-annihilation/co-scattering). The solid curves show the correct DM relic abundance of $\Omega_\chi h^2 = 0.1199 \pm 0.0022$ measured by Planck Collaboration

	process	scaling
pair annihilation	$\chi_\ell\chi_\ell \to W^+W^-$	$(g\sin\theta)^4$
	$\chi_\ell\chi_\ell \to h^* \to f\bar{f}, VV$	$(\mu\sin(2\theta)/v)^2$
	$\chi_\ell\chi_\ell \to hh$	$(\mu\cos(2\theta)/v)^4$
co-annihilation	$\chi_\ell\chi^+ \to f\bar{f}', VV$	$(g\sin\theta)^2$
	$\chi_\ell\chi_h \to W^+W^-$	$(g\sin\theta)^2$
	$\chi_\ell\chi_h \to h^* \to f\bar{f}, VV$	$(\mu/v)^2$
mediator annihilation	$\chi_h\chi_h \to W^+W^-$	$(g\cos\theta)^2$
	$\chi_h\chi^+ \to f\bar{f}', VV$	$(g\cos\theta)^2$
	$\chi^+\chi^- \to f\bar{f}, VV$	g^2
mediator decays	$\chi^+ \to \chi_\ell f\bar{f}'$	$(g\sin\theta)^2$
	$\chi_h \to \chi_\ell f\bar{f}$	$(\mu/v)^2$
co-scattering	$\chi_\ell f \to \chi^+ f'$	$(g\sin\theta)^2$
	$\chi_\ell f \to \chi_h f$	$(\mu/v)^2$
scattering	$\chi_\ell f \to \chi_\ell f$	$(\mu\sin\theta/v)^2$

Table 4.1: Dark sector processes relevant at freezeout and their scaling with the Higgs-portal coupling μ/v and the singlet-triplet mixing angle θ. Here W and h are the W and Higgs bosons of the SM, f/f' and V stand for arbitrary SM fermions/vector bosons.

at 68 % CL [128]. The results were again obtained using `micrOMEGAs` [127]. The shaded regions of the same color show the corresponding parameter space excluded by XENON1T Collaboration at 90% CL [126]. The grey shaded regions are excluded by the LEP constraints on the BSM charged fermions [129].

The analysis given below is valid for both scalar and pseudo-scalar scenarios. Quantitatively, a given constraint on the mixing angle θ results in larger excluded values of μ/v for the pseudo-scalar case since θ itself is smaller in the latter scenario (see the discussion in Section 4.2). This feature makes the two scenarios *phenomenologically distinguishable*.

If μ/v is large, pair annihilation processes alone can account for the correct DM relic abundance. In this case, the main fraction of DM is produced at the temperature $T_{\rm dec}$ at which reactions of the type $\chi_\ell\chi_\ell \to$ SM depart from (chemical) equilibrium. Other processes listed in Table 4.1 decouple later on ($T < T_{\rm dec}$), having an exponentially small impact on the DM net density (see Figure 3.2). In this regime, the DM production does not rely on other dark sector particles making the model effectively equal to the pure singlet case. Therefore, as expected, such couplings are excluded from direct detection constraints. In Figure 4.3, we illustrate this regime for $\mu/v = 0.2$ where all the parameter space relevant at colliders is excluded in the scalar scenario. In the pseudo-scalar case, masses above $m_l \gtrsim 200$ GeV are allowed.

With the decrease of μ/v the annihilation processes scale as θ^4 and become incapable of setting the correct DM relic abundance. Therefore, interactions with other dark species become crucial. In this regime, the DM relic density is determined by the co-annihilation processes discussed in Section 3.1. The number densities of the dark sector particles are exponentially sensitive to their masses, $n_i \propto \exp(-m_i/T_{\rm dec})$. For co-annihilations to be active, all the interacting partners must be abundant at $T = T_{\rm dec}$ meaning that the dark spectrum has to be compressed. In our model, the mass difference of $\Delta m_{cl}/m_l \simeq \Delta m_{hl}/m_l \simeq 10\%$ is needed to prevent DM overabundance. This regime is illustrated in Figure 4.3 by $\mu/v = 0.08,\ 0.02$. In the former case, only a part of the parameter space is excluded by direct detection. For $\mu/v = 0.02$, XENON1T results are not shown since they are weaker than the LEP constraints. In this case, almost all parameter space in the region of interest is allowed.

With even further decrease of μ/v, the co-annihilation processes that scale as θ^2 become irrelevant as well. The DM relic abundance then relies on the (unsuppressed by the coupling) mediator annihilation processes with the consequent decays of the latter to χ_l[4]. To provide the correct relic abundance, mediators must not be much heavier than χ_l leading to the similarly compressed spectrum as in the co-annihilation case.

We will study the collider phenomenology of the co-annihilation and the mediator annihilation regimes in the next section. Here, we would like to describe a scenario that has not yet been fully explored.

Co-scattering

Let us compare the processes in Table 4.1 at very small couplings more accurately. At small μ/v (or θ) pair annihilations and co-annihilations are irrelevant and mediator annihilations are active. At some small values of μ/v, mediators whose decay rates scale as θ^2 become long-lived at decoupling. At the same time, the co-scattering processes, even though they scale as θ^2 as well, are not necessary irrelevant. The reason is an additional kinematic enhancement these processes gain since some of the participating SM particles are relativistic and thus very abundant at $T = T_{\rm eff}$. For illustration, let us compare the decoupling conditions of a co-annihilation and a co-scattering process (see Section 3.1 for the derivation of the decoupling condition),

$$\begin{aligned} \text{co-annihilation: } & n_M \langle \sigma v \rangle_{\rm eff} \sim H \\ \text{co-scattering: } & n_{SM} \langle \sigma v \rangle_{\rm eff} \sim H, \end{aligned} \tag{4.23}$$

where H is the Hubble parameter, n_M is the number density of the dark sector mediators (in our case, χ^+ and χ_h) and n_{SM} is the number density of the SM particles. Since the dark sector particles are non-relativistic, $n_M \ll n_{SM}$, meaning that even though both the co-annihilation and the co-scattering processes have the same scaling with μ (θ), the latter

[4] in principle, if mediator decays are forbidden (for a reason to be defined) or very suppressed, the mediators themselves can contribute to the (multi-component) DM. We do not focus on such scenarios since they would not allow for collider signatures that rely on finite mediator lifetime which are crucial in this study.

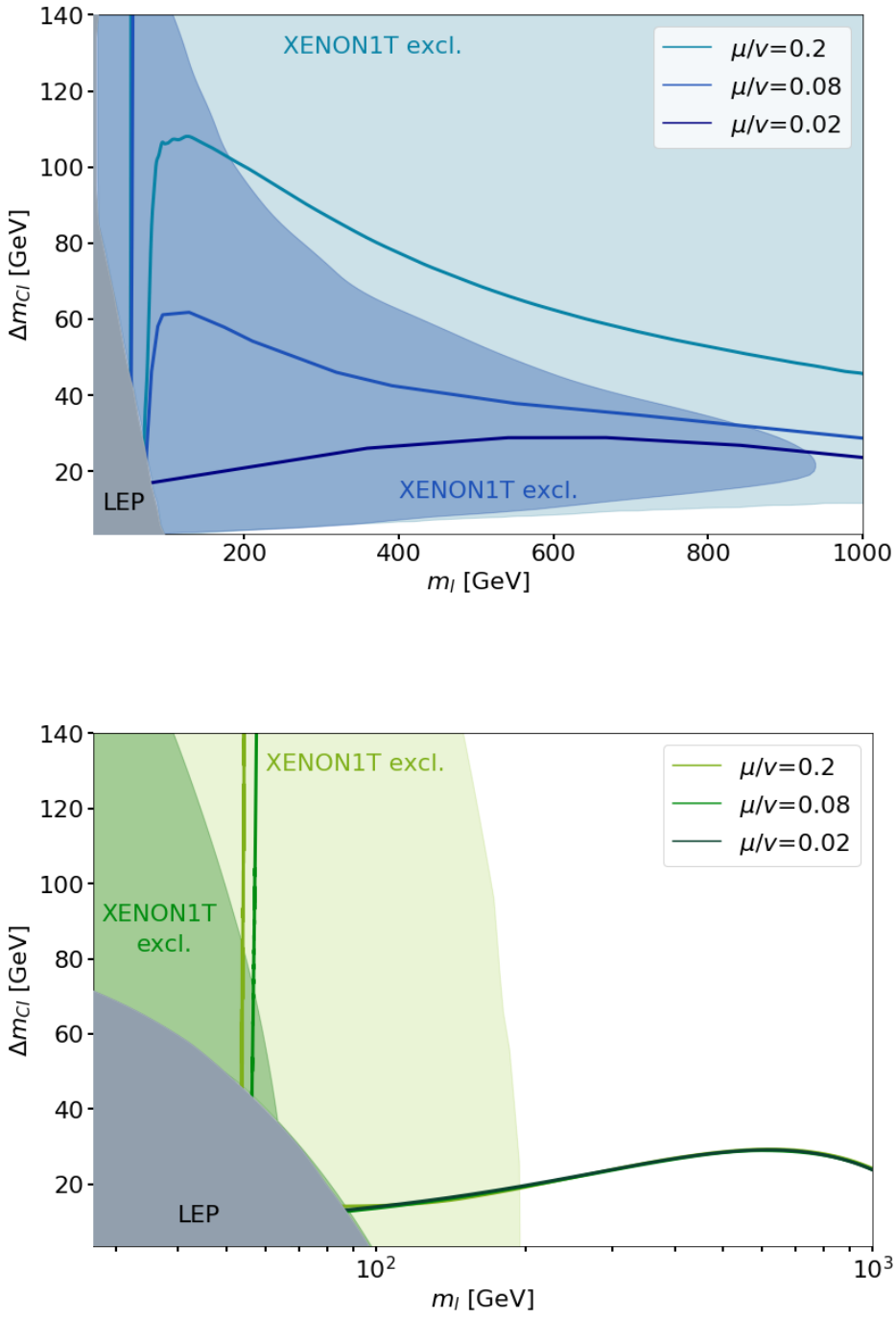

Figure 4.3: DM relic abundance and the corresponding direct detection constraints in the scalar (top) and pseudo-scalar (bottom) scenarios. Solid lines show the observed relic abundance of $\Omega_\chi h^2 = 0.12$ for fixed values of μ/v. Shaded regions are excluded by Xenon1T at 90% CL for the value of μ/v of the same color. The grey region is excluded by LEP.

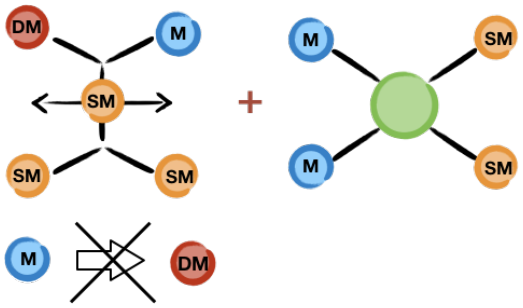

Figure 4.4: Schematic presentation of the co-scattering process. In our model $DM = \chi_l$, $M = \chi^+/\chi_h$, $SM = f/V$ (see Table 4.1).

is much more active at decoupling.

In the co-scattering regime, the DM number is changed through the chain of the following processes (see Figure 4.4 for illustration):

1. DM conversion to a heavier dark state(s) M.

2. M annihilates (or co-annihilates together with another heavy dark particle M$'$) to SM particles.

These processes set the dark sector relic abundance. Later on, M either decays to DM or contributes to the multi-component DM. The co-scattering regime is realized if the following takes place:

- Mediator annihilations are in chemical equilibrium.

- Mediator decays are slower than the mediators annihilations $\Gamma_{\rm dec} \ll \Gamma_{\rm m,ann}$.

These two requirements ensure that the particle M, created during the first stage of the co-scattering process, does not decay back to DM before meeting its (co-)annihilating partner.

Co-scattering: implementation and generality

Importantly, the co-scattering regime is not specific to our model. It must take place in many models with extended dark sectors at small couplings. However, there had been just a handful of studies that pointed out the presence of this regime at the time our work [110] was published. At the moment of writing this thesis, the list of models where the co-scattering (or sometimes called the "conversion-driven freezeout") regime was discovered has expanded, including DM models with masses ranging from MeV to above TeV [97, 123, 130–136].

Due to strong direct detection constraints, the viable theories of thermal DM are forced to lay in the multi-particle small-coupling limit in which co-scattering is very likely to be crucial. Thus, an accurate prediction of the DM relic abundance in this regime is essential for DM phenomenology. However, to date, co-scattering processes *are not included in public codes* that calculate the DM relic abundance.

The implementation of these processes in a general and model-independent way is a challenging task due to the following reasons:

- Co-scattering describes the conversion of particles within the dark sector. Hence, a system of Boltzmann equations that tracks individual number densities of each dark particle has to be solved. Currently, however, the most used public codes solve only one Boltzmann equation for the overall number density of all dark species (see Equation (3.25)). Inclusion of the co-scattering processes thus requires major changes in the Boltzmann solver codes.

- In many models, the co-scattering phase takes place when the *thermal* equilibrium for DM particles is lost. It is also true in the singlet-triplet model discussed here: from Table 4.1 we see that both co-scattering and DM-SM scattering processes gain the same relativistic enhancement described by Equation (4.23). The latter, however, is more suppressed by the portal coupling. This means that the DM particles no longer have an equilibrium distribution at the moment of decoupling and the procedure of Section 3.1 is not applicable. Strictly speaking, *a system of non-integrated Boltzmann equations* must be solved for an accurate prediction of the DM net abundance. However, since many models assume CDM, the non-thermal distortions are small and simplified calculations can be made (see the recent model-dependent calculations in the co-scattering regime [130], as well as a more general simplified treatment of out-of-equilibrium particles during freezeout [97]).

The co-scattering regime can be viewed as the "fourth exception to thermal DM" along with the processes discussed in Section 3.3. It takes place in models with co-annihilation DM production at very small couplings. Inclusion of this regime to the DM relic density Boltzmann codes is a challenging yet important for the DM phenomenology task.

Freezeout phases

In Figure 4.5, we display the freezeout phases of our model depending on the Higgs portal coupling μ/v for a benchmark point $m_l = 500$ GeV, $\Delta m_{cl} = 30$ GeV. The main features of the phase diagram are very similar for other DM masses. As discussed above, with the decrease of the coupling, the relic density is determined by annihilation, co-annihilation, mediators annihilation and co-scattering processes. The lower dashed line indicates the coupling at which the thermally averaged co-scattering rate becomes smaller than the (thermally averaged) mediator annihilation. However, this is not yet the moment of entering the co-scattering phase. The latter takes place only at $\mu/v \simeq 2\times10^{-7}$ (5×10^{-6}) in the scalar (pseudo-scalar) scenario, where charged mediator decays drop below the Hubble rate[5]. Since the fermion mixing is smaller in the pseudo-scalar case, each phase is reached at a larger coupling μ/v in this scenario. The different Lorentz structure of Higgs and gauge couplings in both scenarios (see Equation (4.18)) has only a subleading effect on the annihilation rates.

[5]Due to the smaller decay rate of χ_h (see Section 4.5 and Appendix B), they become long-lived already at $\mu/v \sim 10^{-4}$ (0.005). However, since processes involving χ_h contribute less than about 10 % to mediator annihilation in this region, we expect that the relic abundance can still be reliably obtained without including co-scattering in the Boltzmann equations.

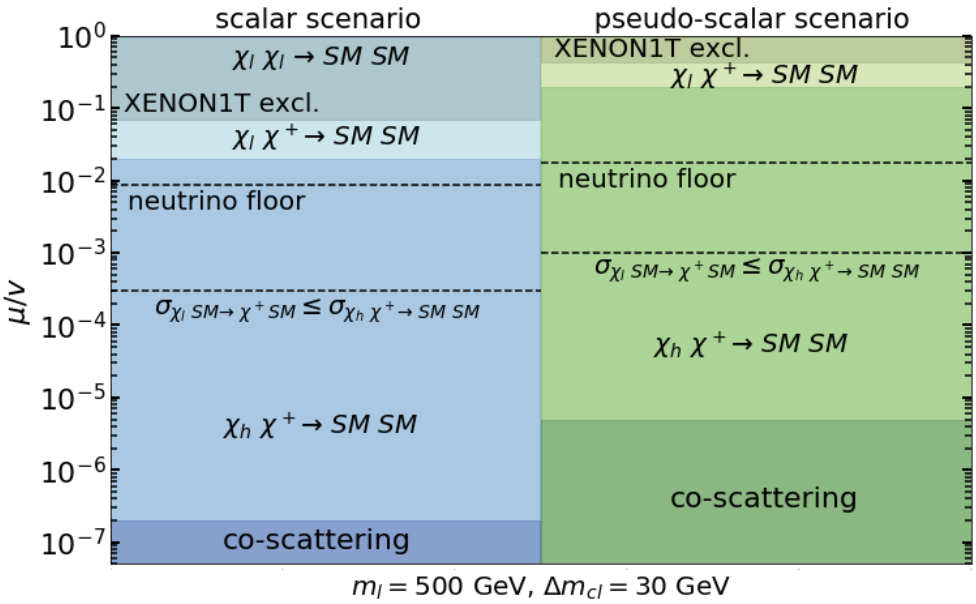

Figure 4.5: DM freezeout phases for small Higgs-portal couplings μ/v. The colored areas denote regions of pair annihilation, co-annihilation, mediator annihilation, and co-scattering, from top to bottom. Displayed processes dominate the relic abundance upon freezeout. "SM" refers to standard-model particles f, f', V.

In particular, all processes that dominate the DM abundance can proceed in an s-wave in either scenario (see also [137]).

As discussed above, direct detection rules out regions of DM pair annihilation. Interestingly, it can probe only the co-annihilation scenarios since the other phases are realized for couplings *below the neutrino floor* (upper dashed line). The collider searches discussed in the next section, on the other hand, are sensitive to these regions, providing a unique way to experimentally probe the mediator decays and the co-scattering scenarios at the moment.

4.5. Long-lived signatures at the LHC

In Section 2.3, we briefly discussed the canonical DM searches at colliders that we will call "the MET searches". They are, however, not successful when applied to co-annihilation/co-scattering scenarios. The reason is that the latter imply *compressed dark spectra* and do not feature substantial MET, making the collider signatures too soft for the standard methods (see the discussion about prompt soft leptons for detail).

Let us summarize the constraints derived in Sections 4.3 and 4.4 that direct detection and relic abundance measurements put on the mass splittings of our model. For every DM mass m_l, the former requires the portal coupling μ/v and the mass splitting between the heavy states to be small, Δm_{hc}, whereas the latter fixes the remaining splitting, Δm_{cl}. The parameter region of interest is thus

$$100\,\text{GeV} \lesssim m_c \lesssim 1\,\text{TeV},\ \Delta m_{hc} \lesssim \text{ few GeV},\ \Delta m_{c\ell} \approx 15 - 30\,\text{GeV},\ \mu/v < 0.2. \qquad (4.24)$$

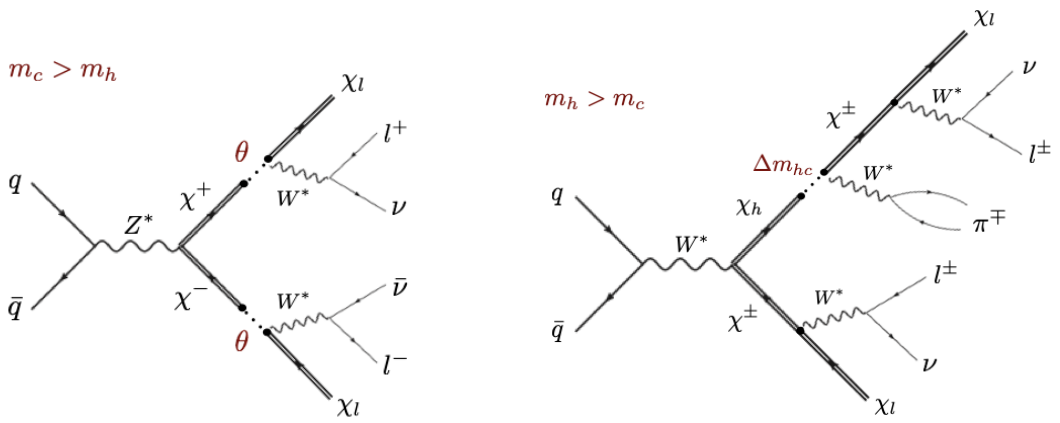

Figure 4.6: Proposed new signatures in the singlet-triplet model at the LHC. Left: a pair of displaced soft leptons. Right: one displaced and one prompt soft leptons.

The choice of the mass range is dictated by the LEP constraints on charged fermions (lower bound) and accessibility at the LHC at the high-luminosity phase (upper bound).

We propose to search for DM χ_l in decays of heavier states $\chi^+,\ \chi_h$. The latter are produced at the LHC in Drell-Yan-like processes. Their production rate depends predominantly on the invariant mass of the mediator pair (with the exception of the processes $pp \to \chi^+\chi_h$ that get a suppression factor of $(g\cos\theta)^2$ in case of large fermion mixing). The mediators' channels depend on the mass hierarchy (see Figure 4.1) and include

$$\chi^+ \to \chi_h\,\pi^+, \quad \chi^+ \to \chi_\ell\, l^+\nu, \quad \chi^+ \to \chi_\ell\,\text{hadrons}, \tag{4.25}$$

$$\chi_h \to \chi^+\,\pi^-, \quad \chi_h \to \chi_\ell\, b\bar{b}, \tag{4.26}$$

where $\pi,\ l,\ \nu$ and b stand for pions, charged leptons, neutrinos and b quarks. The corresponding collider signatures are shown in Figure 4.6. Before discussing them in detail, let us first work out the mediator decay rate at the LHC.

Mediator decay rates and corresponding signatures

In the limit of small coupling μ/v and mass splitting between the initial and final states ΔM, mediator decay width has the following form:

$$\Gamma \propto \left(\frac{\mu}{v}\right)^x (\Delta m)^y \times \text{PS}, \tag{4.27}$$

where PS is the phase-space factor, x and y depend on the type of decay process. If mediator decays to DM, the mass splitting $\Delta m_{c\ell} \approx \Delta m_{h\ell} \approx 15 - 30\,\text{GeV}$ is sizable but the decays are suppressed by the small portal coupling (see Equation (4.18)). If, on the other hand, mediators decay to one another (i.e. decays that lead to $\chi^+ \leftrightarrow \chi_h$), the corresponding widths are not suppressed by the coupling but by the phase-space factor (for example, for decays $\chi^+ \leftrightarrow \chi_h\pi^+$ this factor is $\text{PS} = \sqrt{1-(m_\pi/\Delta M)^2}$). For small couplings, this results in both decay types becoming displaced and the mediators becoming *long-lived at collider scales*. Interestingly, they become long-lived exactly at the couplings that lead to

the co-annihilation/co-scattering freeze-out phases.

Let us discuss, which decays are dominant at different portal couplings without going through detailed calculations. The derivation of all relevant decay widths can be found in Appendix B.

If μ/v is large enough, χ_h is the heaviest state (normal hierarchy). It decays predominantly via $\chi_h \to \chi^+\pi^-$, if kinematically allowed. If, on the contrary, the hierarchy is inverted or the mass splitting $\Delta m_{hc} < m_\pi$, decays via the off-shell Higgs boson, $\chi_h \to \chi_l\, h^*$, $h^* \to b\bar{b}$, become dominant (loop-induced decays like $\chi_h \to \chi_\ell\gamma$ feature an additional suppression by the small portal coupling and can be neglected [138]). This decay rate is suppressed both by the small coupling μ/v and the bottom Yukawa coupling, making χ_h long-lived. The former decay may result in emerging track signatures at colliders. Here, however, we focus on the latter channel. In the limit of $\Delta m_{h\ell} \ll m_h$, the corresponding decay rates in the scalar and the pseudo-scalar case read[6]

$$\begin{aligned}\Gamma_h^S &= \frac{G_F}{10\sqrt{2}\pi^3}\frac{m_b^2}{M_H^4}\left(\frac{\mu}{v}\right)^2\cos^2(2\theta)(\Delta m_{h\ell})^5 \sim \left(\frac{\mu}{v}\right)^2\left(\frac{m_b}{v}\right)^2\frac{(\Delta m_{h\ell})^5}{v^4},\\ \Gamma_h^P &= \frac{3G_F}{280\sqrt{2}\pi^3}\frac{m_b^2}{M_H^4}\left(\frac{\mu}{v}\right)^2\cos^2(2\theta)\frac{(\Delta m_{h\ell})^7}{m_h^2} \sim \left(\frac{\mu}{v}\right)^2\left(\frac{m_b}{v}\right)^2\frac{(\Delta m_{h\ell})^7}{v^4 m_h^2},\end{aligned} \tag{4.28}$$

where m_b and M_H are the bottom quark and the Higgs boson masses correspondingly. At small μ/v, these decays result in signatures with two displaced b-jets of an arbitrary displacement. Note the additional suppression of $(\Delta m_{hl}/m_h)^2$ of the pseudo-scalar rate. It originates from the p-wave emission of χ_l and the $b\bar{b}$ pair required by parity conservation.

In the normal hierarchy case, the charged state decays predominantly via $\chi^+ \to \chi_\ell\, l^+\nu$ and $\chi^+ \to \chi_\ell\,$hadrons[7]. Again, in the small-splitting limit $\Delta m_{c\ell} \ll M_W, m_c$, the partial widths of the leptonic decay $\chi^+ \to \chi_\ell\, \ell^+\nu$ read

$$\begin{aligned}\Gamma_W^S &= \frac{2G_F^2}{15\pi^3}\sin^2\theta(\Delta m_{c\ell})^5 \sim \left(\frac{\mu}{v}\right)^2\frac{(\Delta m_{c\ell})^3}{v^2},\\ \Gamma_W^P &= \frac{2G_F^2}{5\pi^3}\sin^2\theta(\Delta m'_{c\ell})^5 \sim \left(\frac{\mu}{v}\right)^2\frac{(\Delta m'_{c\ell})^5}{v^2(m_c+m'_\ell)^2}\end{aligned} \tag{4.29}$$

The decays are again smaller in the pseudo-scalar scenario due to the smaller mixing angles in this case. In the small-coupling limit, χ^+ becomes long-lived, providing signatures with displaced leptons/jets.

This statement does not, however, hold for arbitrarily small μ/v. Since for tiny portal couplings the inverted hierarchy takes place, another decay channel of χ^+ opens up. The 2-body decay $\chi^+ \to \chi_h\,\pi^+$ starts dominating over the leptonic and hadronic decay modes, providing us with the signature of disappearing charged tracks. The decay rate is almost the same in both scalar and peudoscalar scenario due to the very mild dependence on the portal

[6] This approximation is not always valid for the parameters considered in this work. For the numerical calculations we used the full decay rates provided in Appendix B.

[7] For the mass splittings of the order of $15 - 30$ GeV the spectator quark model is applicable. The relative impact of hadronic decays can thus be estimated from the relevant CKM elements and color factors.

coupling at such tiny mixings ($\cos\theta \approx 1$). The displacement in this case is controlled by the phase-space suppression due to the small mass splitting $\Delta m_{hc} \approx -160\,\text{MeV}$ (see Section 4.2). In the limit of $m_\pi < |\Delta m_{hc}| \ll m_c$, the decay width is given by

$$\Gamma_\pi = \frac{2G_F^2}{\pi}|V_{ud}|^2 f_\pi^2 \cos^2\theta\,|\Delta m_{hc}|^3\Big(1-\frac{m_\pi^2}{(\Delta m_{hc})^2}\Big)^{1/2}, \tag{4.30}$$

where $f_\pi \simeq 130\,\text{MeV}$ is the pion decay constant and V_{ud} is a CKM matrix element. The nominal decay length of the charged fermion for $|\Delta m_{hc}| \approx 160\,\text{GeV}$ is given by

$$c\,\tau_\chi \approx c/\Gamma_\pi = 7.1\,\text{cm} \times \left(\frac{160\,\text{MeV}}{|\Delta m_{hc}|}\right)^3 \left(1-0.76\,\frac{(160\,\text{MeV})^2}{(\Delta m_{hc})^2}\right)^{-1/2}, \tag{4.31}$$

where τ_χ is the proper lifetime of χ^+. This is the limit of $\mu/v \to 0$ which corresponds to the case of pure triplet decay (or pure wino in the context of SUSY).

Let us now discuss the relevant displaced collider signatures at different values of μ/v, going from smaller to larger couplings. We illustrate them in Figure 4.7 in the (m_c, μ/v)-plane. Here m_c sets the overall scale of the dark spectrum. As discussed above, the relative mass differences between the states are set by the direct detection and the relic density measurements. In every point of the parameter space displayed the correct DM relic abundance can be obtained via one of the mechanisms discussed in Section 4.4. Green areas are excluded by existing searches. In orange, we show the projected exclusion regions of the corresponding searches at the LHC in run-II and the high-luminosity (HL-LHC) phase. Red areas correspond to the displaced signatures proposed in this work (see Figure 4.6). The grey region is excluded from XENON1T measurements. Below the upper dashed line, the dark sector's spectrum is inverted. We also indicate the co-scattering region below the lower dashed line where the DM relic density predictions cannot be made accurately. In this region, we still rely on the calculations by `micrOMEGAs` since we expect no significant difference in collider signatures predictions in this region *for our model*. The reason is that disappearing charged track searches rely on the mass splitting between the heavy states, Δm_{hc}, whereas relic density fixes the other splitting, Δm_{cl}. In particular, we expect the green/orange areas, as well as the parameter space below the plot, to be excluded by the disappearing charged track searches.

Disappearing charged tracks

At tiny portal couplings, the charged states produced in the Drell-Yan-like processes, decay via $\chi^+ \to \chi_h\,\pi^+$ (see Figure 4.8, upper leg). In this region, the mass splitting Δm_{hc} decreases with the increase of μ/v. This decay is kinematically allowed as long as $\Delta m_{hc} > m_\pi$, corresponding to $\mu/v \lesssim 10^{-6}\,(10^{-5})$ in the scalar (pseudo-scalar) scenario[8]. Charged mediators with nominal decay length of few cm leave tracks in the innermost layers of the detector and decay before reaching the outer tracking layers [139–141]. The outgoing

[8] More rigorously, the upper edge is set by the requirement $\Gamma(\chi^+ \to \chi_h\,\pi^+) = \Gamma(\chi^+ \to \chi_\ell\,l^+\nu) + \Gamma(\chi^+ \to \chi_\ell + \text{hadrons})$. The larger values of μ/v obtained in pseudo-scalar scenario is due to the smaller three-body decay rates in this case (see Equation (4.30)).

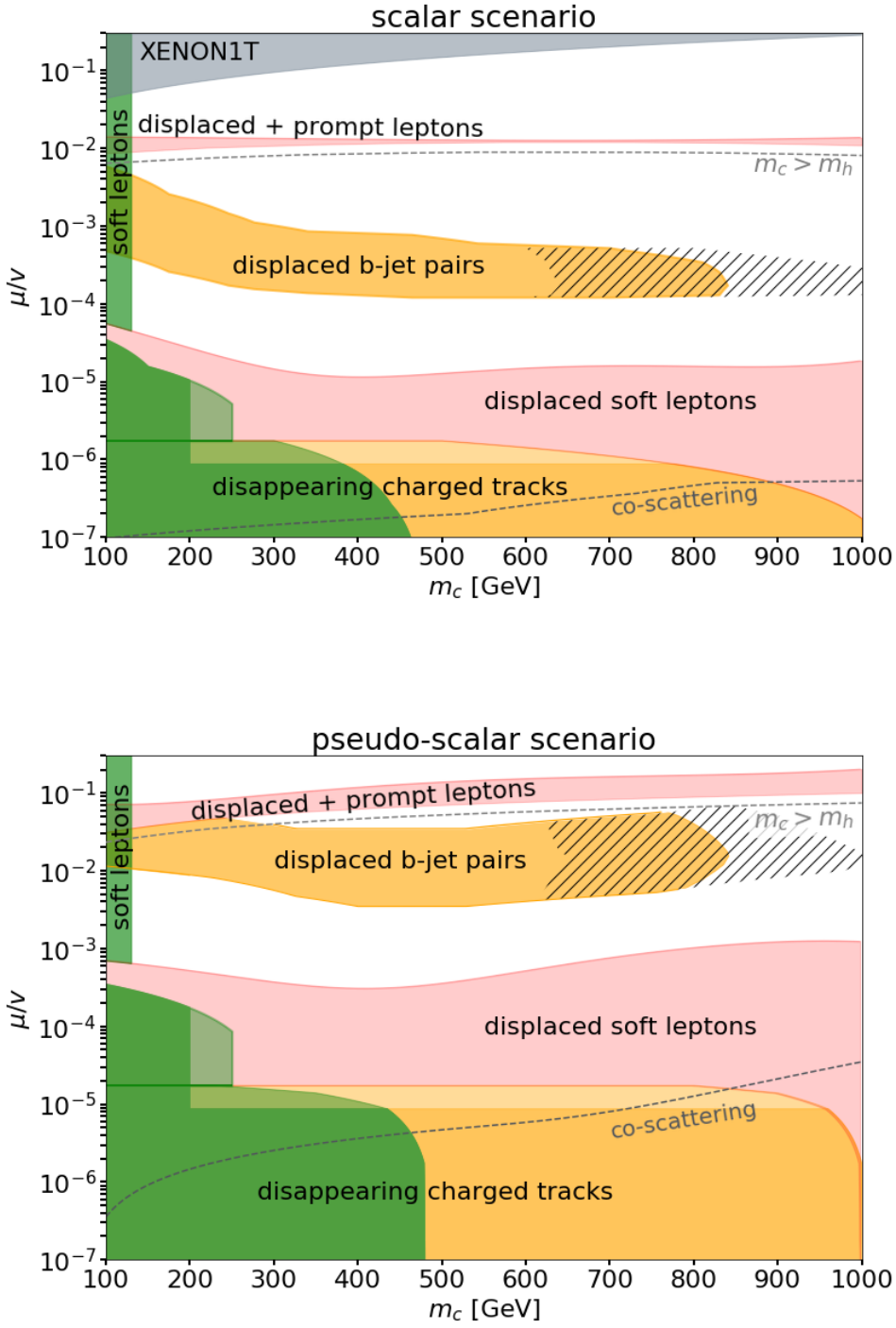

Figure 4.7: LHC signatures of singlet-triplet DM at small Higgs portal couplings in the scalar (top) and pseudo-scalar (bottom) scenarios. Green regions are excluded by existing searches. Orange regions show projections for the LHC after run II and for the HL-LHC. Red regions mark new signatures that have not been explored yet. The dashed region is due to the unknown detection efficiency of displaced b-jets. Below the lower dashed curve the relic abundance is set by the co-scattering processes.

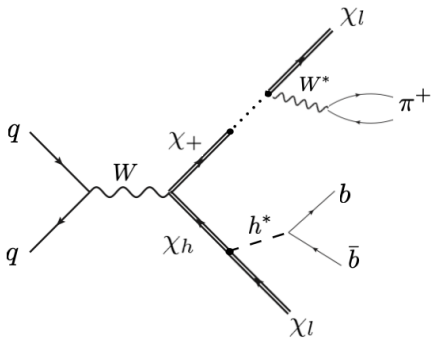

Figure 4.8: Diagrams that correspond to existing and proposed by other authors displaced searches at the LHC and reinterpreted in our work: disappearing charged tracks (upper leg) and displaced b-jets (lower leg).

pion is too soft and is not detected. The ATLAS Collaboration has performed a dedicated search for supersymmetric winos with similar decay length [142], which is directly applicable to our case.

By reinterpreting their results, we exclude charged mediator masses up to $m_c \approx 460\,(480)$ GeV. This search was later recast in [141] for higgsino DM. By rescaling the production rate obtained in this study to the triplet case, we obtained the HL-LHC predictions for the disappearing charged track search in our model. The resulting coverage reaches up to 1 TeV. For both green and orange areas, the lighter shades mark the regions where the branching ratio for $\chi^+ \to \chi_h \pi^+$ is less than 90 %, which may weaken the bounds derived assuming 100 % decays into pions.

The mass range accessible by the disappearing charged track searches indicates the great success of displaced searches, especially if compared to the prompt signatures discussed below.

Prompt and displaced soft leptons

At larger portal couplings, pion decay channel "shuts down" and χ^+ decays predominantly to soft leptons and jets via three-body decays $\chi^+ \to \chi_\ell f \bar{f}'$. The transverse momentum of the outgoing lepton defined by the mass splitting Δm_{cl}, ranges around $p_T^l \approx 15 - 40\,\text{GeV}$.

Searches for prompt soft leptons and missing energy at the LHC suffer from high backgrounds. Thus, they have to trigger on additional high-pT jets emitted from the initial state at the cost of the production cross section. The latter decreases also with the mediator mass. As a result, prompt searches exclude a wide range of couplings but only for light masses.

In Figure 4.7, we show the exclusion regions from the prompt soft lepton analysis done by the CMS Collaboration [143][9] and recast in [123]. The original analysis assumes a decay of 100 % via $\chi^+\chi_h \to \chi_\ell W^* \chi_\ell Z^* \to \chi_\ell l^+ \nu\, \chi_\ell l^+ l^-$. However, in our model $\chi_h \to \chi_\ell Z^* \to \chi_\ell l^+ l^-$ is loop- and mixing-suppressed and thus small compared to $\chi_h \to \chi_\ell h^* \to \chi_\ell b\bar{b}$. In the recast study, limits under the assumption of pure $\chi^+\chi^-$ production for a singlet-

[9] Searches for pairs of prompt soft leptons have been also performed by ATLAS Collaboration [144].

triplet DM model were derived. Prompt soft searches exclude masses of $m_c \lesssim 130\,\text{GeV}$ for $5 \times 10^{-5} < \mu/v < 0.02$ in the scalar scenario and $7 \times 10^{-4} < \mu/v < 0.07$ in the pseudo-scalar scenario. The lower μ/v values correspond to $c\tau_{\chi^+} < 200\ \mu\text{m}$ since larger decay length fall into the category of displaced searches. These bounds can be slightly improved by adding the production mode $pp \to \chi^+\chi_h$. In the case of normal hierarchy which takes place for $\mu/v \gtrsim 0.02$ (0.07) in the scalar (pseudo-scalar) scenario, χ_h decays into a soft lepton, see the right panel of Figure 4.6. We expect, however, no significant increase of sensitivity since this signature results in two soft leptons in our model, contrary to the three leptons requested in the experimental analysis. Optimizing the search to exactly two leptons in the final state might increase the sensitivity even further. Nevertheless, high backgrounds would still limit the reach of prompt soft searches.

At portal couplings $\mu/v < 5 \times 10^{-5}$ in the scalar and $\mu/v < 7 \times 10^{-4}$ in the pseudo-scalar scenario, χ^+ decays predominantly via $\chi^+ \to \chi_\ell f \bar{f}'$ with a sizable displacement (this is the region of inverted hierarchy). The lifetime of the charged state is larger than the vertex resolution of the detector [145], $c\tau_{\chi^+} > 200\ \mu\text{m}$. Even though hadron modes dominate the decay width, we focus on much cleaner lepton decay channels. The proposed signature is a pair of oppositely charged displaced soft leptons, shown in the left panel of Figure 4.6. The longest decay length of χ^+ at which lepton decays still dominate over the two-body pion mode, is $c\tau_{\chi^+} = 1.5\,\text{cm}$ (4 cm) in the scalar (pseudo-scalar) scenario.

Usage of the displacement information is very helpful for background rejection, allowing to probe much softer final states. However, existing soft lepton searches put high transverse momentum cuts on the outgoing leptons. These analyses, although non-optimized for our model, nevertheless show promising results. CMS Collaboration performed two searches with displaced leptons at 8 TeV with a lepton momentum cut of $p_T^l > 25\,\text{GeV}$ [146] and at 13 TeV with the cut of $p_T^l > 40\,\text{GeV}$ [145]. While the momentum cut of the 13-TeV analysis is too strong for our model, a fraction of events with displaced soft leptons falls into the signal region of the 8-TeV analysis. Authors of [123] recast this analysis for quintuplet DM, which leads to the same final state of displaced soft lepton pairs through a decay chain of doubly-charged fermions. We rescale the quintuplet event rates by a factor of 1/4 and derive the bounds for our model, requiring that the decay length of χ^+ is equal to the decay length of the doubly-charged quintuplet fermion. The resulting 95 % CL exclusion bound is shown as a green area in Fig. 4.7. Even for such high p_T^l cuts mediators with masses up to $m_c \approx 200\,\text{GeV}$ were excluded.

We conclude that displaced lepton searches are indeed very powerful in testing models that result in soft final-state objects at colliders. We propose to extend the long-lived particle searches to smaller transverse momenta p_T^l of the final-state leptons. This will drastically increase the experimental sensitivity to a broad class of dark matter models with compressed spectra. In our model, we show the potential reach of such searches in red in Figure 4.7.

Displaced b-jet pairs

Regions, where χ_c is short-lived, can still be tested with displaced searches by considering decays of the heavy neutral state, χ_h. Produced via $pp \to \chi^+\chi_h$ they decay mainly to a pair of b-quarks (see Figure 4.8, lower leg), resulting in a signature of two displaced soft b-jets.

Authors of [138] analyzed this signature in the context of wino-bino scenario in SUSY. They derived projections for the LHC at 14 TeV, assuming an integrated luminosity of $300\,\text{fb}^{-1}$ and taking the detection criteria for displaced vertices from the ATLAS search [147] based on 8 TeV data. We reinterpreted their analysis and derived the bounds indicated in orange in Figure 4.7. The dedicated analysis of 14 TeV data is expected to probe mediator masses up to $m_h \approx 800\,\text{GeV}$.

The predicted detection efficiency is promising for a decay length in the range $1\,\text{cm} \lesssim c\tau_{\chi_h} \lesssim 1\,\text{m}$, with a peak around $c\tau_{\chi_h} \approx 10\,\text{cm}$. The lower edge of this area corresponds to the largest length at which mediators still decay within the detector. Regions of smaller μ/v might be covered by the proposed surface detectors [148]. The upper edge is set either by the sensitivity limit $c\tau_{\chi_h} = 1\,\text{cm}$ or, at small m_c in the pseudo-scalar scenario, by the requirement that $m_h = m_c + m_\pi$. The latter indicates the point at which the spectrum is inverted and χ_h decays dominantly via $\chi_h \to \chi^+\pi^-$. The hatched area shows the large uncertainties on the displaced vertex reconstruction [138].

One displaced and one prompt lepton

Finally, a signature with two soft leptons with different topologies is possible in case of normal hierarchy. In this region, mediators produced via $pp \to \chi^+\chi_h$ decay to one prompt lepton, $\chi^+ \to \chi_\ell\, l^+\nu$, and one displaced lepton, $\chi_h \to \pi^-/f\bar{f}'(\chi^+ \to \chi_\ell\, l^+\nu)$. The latter chain is suppressed by the mass splitting Δm_{hc}. The observed signature is one displaced and one prompt soft lepton (either of the same or the opposite charge) and sizable missing energy, see Figure 4.6. Similarly to the search for disappearing charged tracks, we assume the outgoing pion to be undetectable. We indicate the potential reach of such search in red in Figure 4.7. The upper edge of the area is determined by requiring a minimal nominal decay length of $c\tau_{\chi_h} \gtrsim 200\,\mu\text{m}$. Above this line, the mass splitting Δm_{hc} is large enough for prompt decays. The lower edge is set by the kinematic threshold for a two-body decay, $m_h = m_c + m_\pi$. Below this threshold, heavy neutral fermions decay mostly via $\chi_h \to \chi_\ell b\bar{b}$.

4.6. Discussion

Displaced searches at ATLAS and CMS are relatively new. However, they may be the leading tool in exploring extended thermal dark sectors and are complementary to missing energy searches. In particular, they can be used to tackle the problem of *soft objects at the LHC which naturally arise in scenarios with co-annihilation and co-scattering.*

The main reason is that these processes are very sensitive to the mass difference of the dark sector particles involved in the decoupling process. In the singlet-triplet scenario,

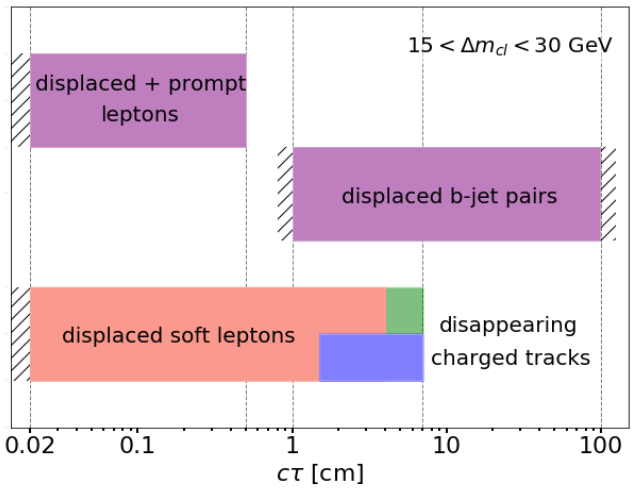

Figure 4.9: Sensitivity regions for displaced signatures at the LHC. Shown are the ranges of nominal decay lengths of χ^+ (salmon) or χ_h (purple) that can be tested by ATLAS and CMS. Green and blue areas have already been excluded by searches for disappearing charged tracks. The mass difference $\Delta m_{c\ell}$ is varied within the range that is compatible with the observed DM abundance.

the mass splitting between the lightest and the next-to-the-lightest state is $\Delta m_{cl} \simeq \Delta m_{hl} \simeq 15 - 30$ GeV. In models with other combinations of electroweak multiplets, the typical splitting ranges around $\Delta m \simeq 5 - 50$ GeV (see, e.g. [113, 123]). These numbers define the necessary p_T-cuts at the LHC that make the detection of such dark sectors possible

Displaced searches at CMS and ATLAS can probe small and intermediate mediator lifetimes, larger displacement should be searched for at long-baseline experiments (see [57] for a review). In Figure 4.9, we summarize the mediator decay lengths to which LHC is sensitive. They are classified according to the nominal decay length of the mediator χ^+ (salmon) or χ_h (purple) in both scenarios. Colored areas correspond to regions accessible by ATLAS and CMS detectors. Hatched regions could be probed with extended sensitivity. All other edges are theory bounds (see text). Disappearing charged track searches have already excluded the blue and green parameter regions in the scalar and pseudo-scalar scenarios respectively. We see that our model predicts signatures with different final states in basically all accessible layers of the LHC detectors. Therefore, it can serve as a relatively simple toy-model for the discussed collider signatures. The search for DM from a small Higgs portal is thus most efficiently done by gathering all these signatures in a combined interpretation.

In the next chapter, we will study displaced dark sectors at e^+e^--colliders in the context of the few-GeV-scale dark scalars. Such experiments are characterized by smaller center-of-mass energies compared to the LHC, but also by much less background. The setup thus allows for clean signatures for (soft) light objects.

4.7. Outlook: soft displaced lepton pair at the LHC

In this section, I would like to dig a little bit deeper into the properties of the signature, shown in the left panel of Figure 4.6. I would like to branch out from the DM paradigm and discuss the possibility of performing an analysis of this signature in an as model-independent way as possible. The parameter space of the singlet-triplet model can be parametrized by three parameters,

$$m_c,\ \Delta m_{cl},\ \mu/v. \tag{4.32}$$

For each value of m_c, the DM interpretation fixes the mass splitting Δm_{cl} and the Higgs coupling μ/v by the combination of direct detection and relic density observations. If, however, the DM condition is relaxed, the discussed parameters can vary. When performing an analysis, it is important to explore its full potential, without restricting the search region to specific models. We will therefore try to estimate, which range of parameters may be accessible by the displaced search for soft leptons.

At colliders, the production rate $pp \to \chi^+\chi^-$ is set by m_c[10] and one of the most important kinematic variables, the transverse momentum p_T^l of the outgoing lepton, is mostly determined by Δm_c. We will discuss these variables in more detail later on in this section.

Another distinct feature of our model is the sizable displacement of final-state leptons which is usually characterized by their transverse impact parameters, d_0. The impact parameter, d, of a lepton is defined as the distance from the point of closest approach of the lepton's track and the primary vertex, see Figure 4.10. Its projection to the plane perpendicular to the beamline is d_0. This variable depends on the distance that the mother particle χ_c flies before decaying,

$$d_c = (\beta\gamma)_c c\tau_c, \tag{4.33}$$

where $(\beta\gamma)_c$ is the Lorentz boost of χ_c, as well as from the angle at which the lepton is emitted.

For a decent precision of the lepton displacement detection, the outgoing leptons have to leave at least one hit in the inner tracking system of the LHC detectors. The corresponding impact parameters need to satisfy $d_0 \lesssim 12$ cm for ATLAS and $d_0 \lesssim 10$ cm for CMS. In addition, the displacement needs to be larger than the primary vertex resolution which is $d_0 \simeq 200\,\mu$m for both detectors. The main SM processes that mimic the symmetric lepton signal with such displacements are the semi-leptonic decays of B hadrons produced in the multijet events with heavy flavor jets. The proper decay length of B hadrons is of the order of $200\,\mu$m resulting in the displacements inside the search region.

The experimentally accessible parameter space is characterized by large enough mass splittings Δm_{cl} (such that the final-state leptons have detectable transverse momenta p_T^l), compromised values of μ/v and not-too-high masses m_c. Large couplings are challenging due to high backgrounds, whereas very small values of μ/v result in the suppressed cross section

[10] Note that this process can be mediated by both Z^* and γ^*.

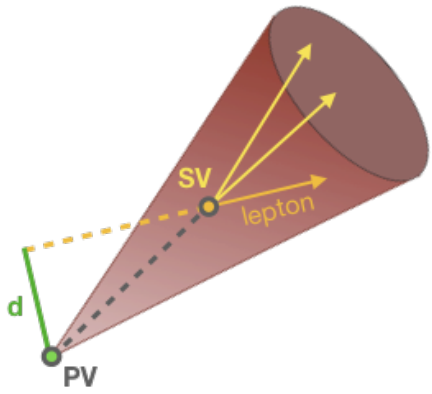

Figure 4.10: Impact parameter d of a lepton, for the definition see text. A long-lived particle, produced at the primary vertex (PV), decays with a displacement creating a secondary vertex (SV).

of the process of interest[11]. Lighter mediator masses are easier to detect due to higher production rates. We illustrate the rather steep dependence of the mediator production cross section, σ_c, in the left panel of Figure 4.11. On the other hand, the transverse impact parameter slightly decreases at small m_c: lighter, and thus more boosted mediators tend to move more into the forward direction, as opposed to the very heavy states which are more likely to be produced in an arbitrary direction. Consequently, leptons, inheriting the mediator's boost, are produced with smaller transverse impact parameters d_0 if the mediators are light. This effect is even more pronounced for the very boosted B hadrons from the background.

In the regions of interest, the charged mediators' production cross section varies in the range $\sigma_c \sim 0.1 - 10$ pb, see left panel of Figure 4.11. The total cross section of the full chain can be estimated as

$$\sigma_{\rm tot} \sim \sigma_c \, \mathcal{B}^2({\rm lept}), \tag{4.34}$$

where $\mathcal{B}({\rm lept})$ is the branching ratio of $\chi^\pm \to l^\pm X$ with X being any SM or dark particle. Focusing on the decays to only one lepton flavor combination, the latter can be estimated as

$$\mathcal{B}({\rm lept}) \sim \frac{\Gamma_W}{3\Gamma_W + 2N_c\Gamma_W + \Gamma_\pi}, \tag{4.35}$$

where the first term in the denominator corresponds to the decays to three lepton flavors (see Equation (4.29)), the second term – to decays into light quark pairs ($N_c = 3$ is the color factor and for simplicity we set the CKM elements $V_{ud} \simeq V_{cs} \simeq 1$) and the latter term – to the pion decay rate (see Equation (4.30)). For example, for $\Gamma_W = 9\ \Gamma_\pi$ (lower lepton branching ratios of χ_c would be hard detect expermentally), $\mathcal{B}({\rm lept}) \sim 10\%$, resulting in $\sigma_{\rm tot} \sim 10^{-2}\sigma_c$. This cross section grows with the increase of Γ_W only mildly. Importantly, the number of background events is orders of magnitude higher [145] so sophisticated selection of the most

[11] We remind the reader that apart from the leptonic/hadronic channels, χ_ℓ can also decay via the mixing-insensitive mode, $\chi^+ \to \chi_h \pi^+$ (see Equation (4.30)).

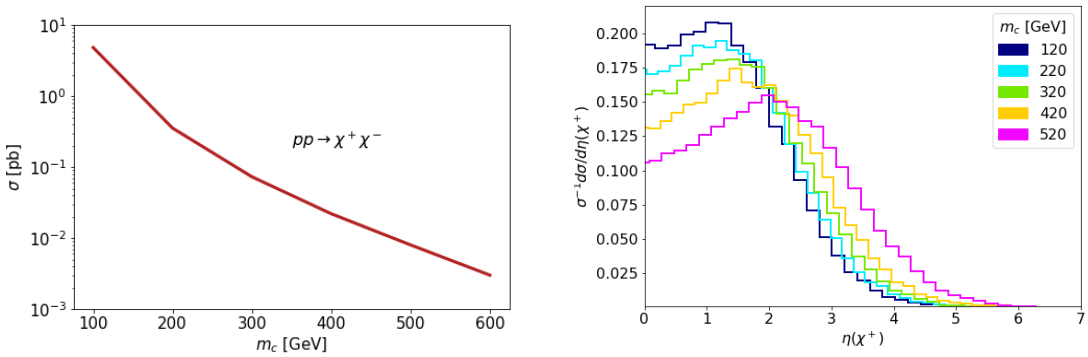

Figure 4.11: Features of the charged mediators at the LHC depending on the m_c: production cross section at $\sqrt{s} = 13$ TeV (left) and the normalized pseudorapidity distribution (right).

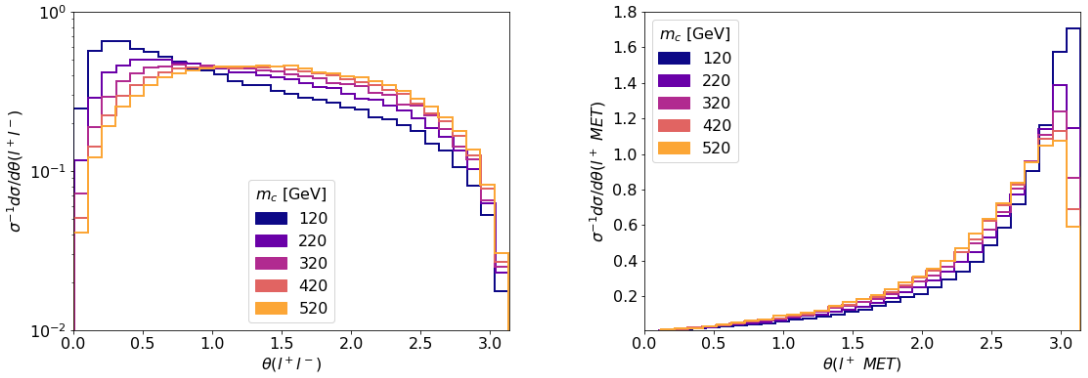

Figure 4.12: Lepton kinematic distributions for different mediator masses: 3D angles between the leptons (left) and between one lepton and MET (right). Other parameters are set to $\Delta m_{cl} = 20$, $\mu/v = 10^{-5}$.

discriminating phase-space regions, preferably made using neural network techniques, are necessary for a successful analysis.

Let us, therefore, discuss the main kinematic features of the signal model. The pseudorapidity distribution of the charged mediator, illustrated in the right panel of Figure 4.11, confirms the tension of heavier mediators to be produced closer to the beamline. Varying the mediator's mass also affects angular distributions of the outgoing leptons. From the left panel of Figure 4.12, we conclude that light mediators are more likely to be produced collinearly, resulting in small angular separation between the daughter leptons. Similarly, the collimated production of light mediators leads to the back-to-back configuration of leptons and MET shown in the right panel of Figure 4.12. Some other experimentally important values are almost insensitive to m_c. They include lepton transverse momentum, MET and the azimuthal angle between the lepton and MET.

The mass splitting between χ_l and χ_c controls the p_T of the outgoing lepton, as well as the amount of produced MET, see Figure 4.13. The increase of the latter for large mass splittings is due to more energy released into the active neutrinos. Note that for all the mass splittings considered our model does not predict significant MET. In the right panel of Figure 4.13

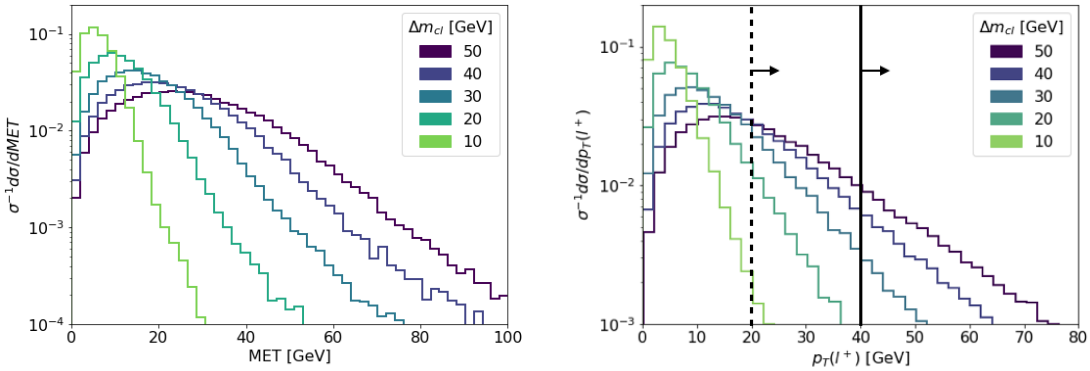

Figure 4.13: Lepton kinematic distributions for different mass splittings Δm_{cl}: MET (left) and transverse momentum of the lepton (right). Other parameters are set to $m_c = 320$ GeV, $\mu/v = 10^{-5}$. Vertical grid lines in the right panel show the momentum cut that is currently used in the CMS displaced lepton analysis [145] (solid line) and the one proposed in this text (dashed line).

we show the p_T^l distributions of the outgoing leptons for different mass splittings. We also indicate the momentum cut of $p_T^l = 40$ GeV currently used in the displaced lepton analysis by the CMS Collaboration [145]. We see that most of the signal is lost due to this cut. For example, the point $\Delta m_{cl} = 22$ GeV in this plot at which the correct DM relic density is achieved for χ_ℓ would most probably be undetectable.

Therefore, we are currently designing a new analysis together with Susanne Westhoff and Nishita Desai, as well as with our colleagues from CMS, Abanti Ranadhir Sahasransu and Freya Blekman, who perform dedicated background study and use neural-network techniques to enhance the signal/background discrimination. Our work is intended to serve as a showcase of an analysis that allows probing lepton transverse momenta down to $p_T^l = 20$ GeV by relying on the significant displacements of the leptons and distinct kinematic features of the signal model. Making such search experimentally possible will imply designing new triggers that allow for a lower p_T^l threshold.

5. Long-lived light dark sectors

In the previous chapter, we saw that long-lived particle (LLP) searches at colliders are very powerful at testing Higgs portals at the electroweak scale. Here we would like to present the prospectives for the LLP signatures at GeV scales. The content of this chapter and the related Appendix C is based on work done in collaboration with Ruth Schäfer and Susanne Westhoff (Heidelberg University) and published in [149]. Most of the results as well as a significant part of the text are taken from the corresponding publication. The credit for the analysis of the missing energy signatures discussed in Section 5.2 is entirely entitled to Ruth Schäfer and Susanne Westhoff.

5.1. GeV-scale dark particles through the Higgs portal

As discussed in Section 2.1, new scalars can couple to SM through the renormalizable Higgs portal. In this section, we show an example of such a theory with the new scalar playing the role of mediator between the SM and the DM. We show how displaced searches at existing colliders can explore large parts of such models, extending the current exclusion limits and even competing with some future long-baseline experiments.

Dark scalars are simple and thus appealing extension of the SM [150, 151]. They can play role of mediators to dark sectors [152][1], force the first-order electroweak phase transition needed for successful baryogenesis [154–156] and play a role of the inflaton [157, 158]. In this chapter, we mainly address the DM problem. However, due to the model independence of the analysis, the results obtained can be used in all the above theories.

Let us now introduce a new real scalar, ϕ, and a Dirac fermion, χ, both of which are singlets under the SM symmetries but charged under a discrete $\mathbb{Z}_2$ symmetry. The latter insures the stability of the fermion preventing its mixing with neutrinos. The Lagrangian of our model reads

$$\mathcal{L} = \mathcal{L}_{\rm SM} - \frac{1}{2}m_\phi^2\phi^2 - \mu\,|H|^2\phi - y_\chi\bar{\chi}\chi\phi - \tfrac{1}{2}m_\chi\bar{\chi}\chi - \lambda\phi^2|H|^2 - \lambda_3\phi^3 - \lambda_4\phi^4, \qquad (5.1)$$

where $\mathcal{L}_{\rm SM}$ is the SM Lagrangian. Couplings $\lambda_{3/4}$ do not affect the phenomenology discussed in this study so for simplicity we set them to zero. Similarly, we assume $\lambda = 0$. Restoring its nonzero value changes the way the effective couplings are expressed in terms of fundamental parameters but does not change the physics conclusions of this chapter[2]. After the EWSB,

[1] In Section 3.3 we discussed the challenges that models where the scalars themselves play the role of DM face, see also discussion in [152, 153].

[2] Note, however, that the neglected couplings should be considered in a general analysis of our model since they may affect other collider signatures, as well as cosmological processes.

the hew scalar ϕ mixes with the Higgs field h_0 through

$$\mathcal{L}_{\text{mass}} = -\frac{1}{2} M_{ij} \Phi_i^\dagger \Phi_j, \quad M = \begin{pmatrix} m_\phi^2 + \lambda v^2 & \mu v \\ \mu v & m_{h_0}^2 \end{pmatrix}, \quad \Phi = \begin{pmatrix} \phi \\ h_0 \end{pmatrix}, \tag{5.2}$$

where the mass term $m_{h_0} h_0^2/2$ originates from the SM part of the Lagrangian in Equation (5.1).

The physical masses of the new scalar S and the Higgs boson h are obtained by diagolizing the matrix M with

$$\begin{pmatrix} S \\ h \end{pmatrix} = \begin{pmatrix} c_\theta\, \phi + s_\theta\, h_0 \\ -s_\theta\, \phi + c_\theta\, h_0 \end{pmatrix}; \qquad \begin{aligned} \sin^2\theta &= \tfrac{1}{2}\left(1 + \tfrac{m_\phi^2 - m_{h_0}^2}{\Delta m^2}\right), \\ (\Delta m^2)^2 &= 4v^2\mu^2 + \left(m_\phi^2 - m_{h_0}^2\right)^2, \end{aligned} \tag{5.3}$$

where we used the compact form s_θ and c_θ for the sine and cosine of the mixing angle θ. The corresponding mass eigenvalues are

$$\begin{aligned} m_S^2 &= \tfrac{1}{2}\left(m_\phi^2 - m_{h_0}^2 - \Delta m^2\right), \\ m_h^2 &= \tfrac{1}{2}\left(m_\phi^2 - m_{h_0}^2 + \Delta m^2\right) \approx (125\,\text{GeV})^2 . \end{aligned} \tag{5.4}$$

Due to the mixing, both physical scalars couple to the SM fermions f and the dark fermion χ,

$$\mathcal{L}_y = y_\chi \left(s_\theta\, \bar{\chi}\chi h - c_\theta\, \bar{\chi}\chi S\right) - \sum_f \frac{m_f}{v}\left(c_\theta\, \bar{f} f h + s_\theta\, \bar{f} f S\right), \tag{5.5}$$

where m_f is the fermion mass and $v = 246\,\text{GeV}$ is the vacuum expectation value of the Higgs field.

From the Lagrangian in Equation (5.5), we see that S follows the flavor-hierarchical coupling structure of the SM Higgs boson. This feature will have important phenomenological consequences. The decay width of the new scalar is determined by its partial decay rates to the SM particles Γ_{SM} and to the dark fermion $\Gamma_{\chi\bar{\chi}}$,

$$\Gamma_S = s_\theta^2\, \Gamma_{\text{SM}} + c_\theta^2\, \Gamma_{\chi\bar{\chi}}, \tag{5.6}$$

where for presentation purposes we factored out θ-dependence in the above expression. We see that SM ("visible") decays are mixing-suppressed with respect to the "dark" ones. The corresponding branching ratios of S to SM leptons, ℓ, and dark fermions, χ, read[159]

$$\begin{aligned} \mathcal{B}(S \to \ell\bar{\ell}) &= \frac{s_\theta^2\, \Gamma_{\ell\bar{\ell}}}{\Gamma_S} = \frac{m_\ell^2 s_\theta^2}{8\pi v^2}\frac{m_S}{\Gamma_S}\left(1 - \frac{4m_\ell^2}{m_S^2}\right)^{3/2}, \\ \mathcal{B}(S \to \chi\bar{\chi}) &= \frac{c_\theta^2\, \Gamma_{\chi\bar{\chi}}}{\Gamma_S} = \frac{y_\chi^2 c_\theta^2}{8\pi}\frac{m_S}{\Gamma_S}\left(1 - \frac{4m_\chi^2}{m_S^2}\right)^{3/2}. \end{aligned} \tag{5.7}$$

Below the muon threshold, photon and electron channels become important. However, this

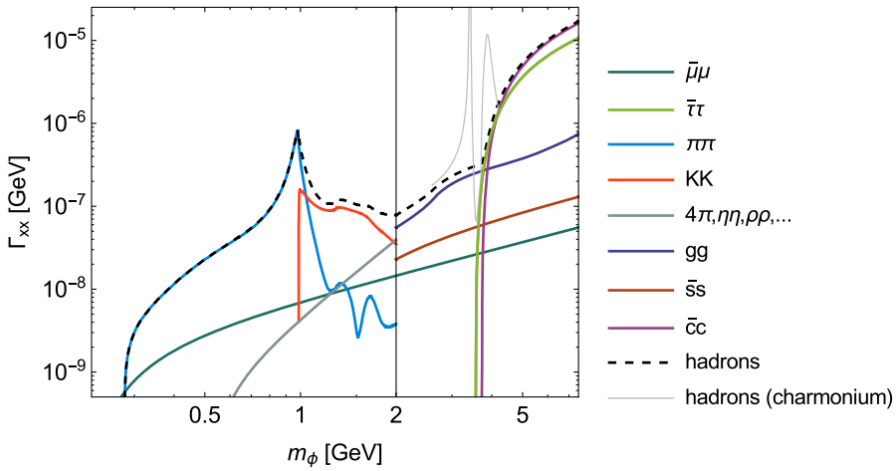

Figure 5.1: Decay modes of a new scalar taken from [160] for $s_\theta = 1$, m_ϕ here corresponds to m_S in the text. The vertical line indicates the change between the dispersive analysis (left) and the spectator model (right) treatments.

region is highly constrained from kaon decays experiments [160]. It also suffers from cosmological and astrophysical bounds. The latter include bounds from Big Bang nucleosynthesis (BBN), energy losses in supernovae (SN) and self-interaction constrains on the S-mediated forces between χ particles if they play role of DM [160, 161]. Therefore, we do not include this region in our analysis.

Calculating the new scalar's lifetime requires the inclusion of its hadronic decay modes. The latter is very challenging and is a subject of ongoing research (for more details, see [160] and references therein). Several approaches are on the market, tackling this problem in different kinematic regimes. At low masses of S, chiral perturbation theory (ChPT) is applicable. The corresponding form factors can be realistically estimated for $m_S \lesssim 0.5$ GeV. At high masses, the perturbative spectator model can be used reliably. The essence of this approach lies in treating decays of a specific quark within a hadron independently from the other quarks that act as "spectators". In our case, such approach is valid for $m_S > 2$ GeV. The intermediate-mass regime is the most challenging, and the best-performing theory of hadrons at these energy scales has not yet established. Currently, one of the most successful approaches is dispersive analysis. It is based on the causality and unitarity conditions on the processes' amplitudes. In this work, we adopt the calculations of Ref. [160] that uses dispersive analysis for $m_S < 2$ GeV and spectator model higher masses. However, in the region of 1.3 GeV $< m_S <$ 2 GeV large corrections are expected. This is due to multihadronic modes that are not taken into account the analysis. In Figure 5.1, we show the scalar's decay rates to the SM states. The mass at which the switch between the dispersive analysis and spectator model treatments happens is indicated by the vertical line. The possible charmonium resonances are not included in our calculations.

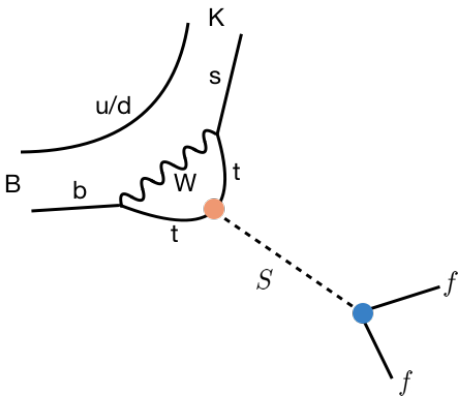

Figure 5.2: Dark scalar production in semi-mesonic decays of B mesons. The production rate relies on the scalar's coupling to the top quark (orange dot), the decay rate is controlled by the coupling (blue dot) that depends on the mass of the decay product f.

5.2. Dark scalars in B meson decays

In this section, we mainly focus on the physics of dark scalars at the so-called B *factories*. At these experiments, a very large number of B mesons is produced (for a review, see [162]). Optimized for the reconstruction of long-lived kaons in B decays, these experiments are also designed for high precision measurements of relatively light displaced particles, making their setup perfect for searches for GeV-scale dark sectors.

At B factories, light dark scalars are resonantly produced in meson decays. In the case of B_q mesons (where $q = s, d$), the scalar S is produced at the loop level through a penguin diagram, see Figure 5.2, upper part [3]. The corresponding effective interaction reads

$$\mathcal{L}_{\text{eff}} = \frac{C_{bq}}{v} \left(m_b \, \overline{q}_L b_R + m_q \, \overline{q}_R b_L \right) S \,, \tag{5.8}$$

where C_{bq} is the dimensionless Wilson coefficient. The latter is identical to the one of the Higgs boson (see e.g. [163]) with an additional suppression factor of $\sin\theta$,

$$C_{bq} = \frac{3\sqrt{2} G_F m_t^2}{16\pi^2} V_{tb} V_{tq}^* \, s_\theta + \mathcal{O}\left(\frac{m_S^2}{m_W^2} \right) . \tag{5.9}$$

In the narrow-width approximation, the lepton/dark decay rates of S thus scale with coupling as

$$\begin{aligned} \mathcal{B}\big(B \to K S\big) \mathcal{B}\big(S \to \ell\bar{\ell}\big) &\propto s_\theta^4 \frac{\Gamma_{\ell\bar{\ell}}}{\Gamma_S} \,, \\ \mathcal{B}\big(B \to K S\big) \mathcal{B}\big(S \to \chi\bar{\chi}\big) &\propto s_\theta^2 c_\theta^2 \frac{\Gamma_{\chi\bar{\chi}}}{\Gamma_S} \,. \end{aligned} \tag{5.10}$$

If $m_S > 2m_\chi$ and $y_\chi c_\theta > m_\ell s_\theta / v$, invisible decays dominate. In the case where dark decays are kinematically forbidden, i.e. for $m_S < 2m_\chi$, only decays to SM particles take place. As

[3] Note that the tree-level contribution is absent since flavor-changing fundamental couplings are absent in our model.

mentioned in the previous section, the latter is more favorable if χ is meant to play role of DM. Strongly suppressed by the coupling, visible decays become displaced at collider scales, opening up a possibility to be tested at various collider and fixed-target experiments. If kinematically allowed, the outgoing meson can induce subsequent decays to S (for example, via the chain $B \to KS, K \to \pi S$).

Naturally, dark scalars can be probed at colliders in two ways: in searches for *missing energy* and in lepton/hadron *displaced searches*. While both of them provide intriguing results, in this thesis we mainly focus on the displaced visible decays, only briefly mentioning the potential of the missing energy signatures. The latter was explored in detail by Ruth Schäfer and can be found in [149].

Dark scalars in missing energy searches

Dark scalars that originate from B mesons provide two types of missing energy signatures: semi-invisible (e.g. $B \to K\not{E}$), and completely invisible ($B \to \not{E}$).

The first signature has been studied in the SM context at BaBar [164] and Belle [165, 166]. These searches rely on the tree-body topology of $\mathcal{B}(B \to K\nu\bar{\nu})$ and thus, can not be reinterpreted in our model. Therefore, we used the only available model-independent bounds on $B \to K\not{E}$ from the BaBar search [167] and found that even this non-optimized search excludes mixing angles $\theta \gtrsim 0.006$ and masses $m_S \lesssim 4.5$ GeV at 95% CL. Our projection for Belle II at 50/ab based on [168] shows the potential of excluding regions down to $\theta \simeq 10^{-3}$. To increase the sensitivity, we suggest to perform a dedicated search that relies on the two-body kinematics of $B \to KS(\to \chi\bar{\chi})$ in the on-shell regime, $m_S < m_B - m_K$. In the low mass region, semi-visible kaon decays also become relevant. The currently strongest bound of $\theta \lesssim 0.22$ on $\mathcal{B}(K^+ \to \pi^+\not{E})$ by E949 [169] can be extended to $\theta \lesssim 0.01$ at NA62[170, 171].

Searches of the fully invisible decays $B_q \to \chi\bar{\chi}$ have high sensitivity around the resonance $m_S = m_{B_q}$. The currently strongest bound on invisible decays $\mathcal{B}(B_d \to \not{E}) < 1.4 \times 10^{-5}$ [172] derived by Belle Collaboration, excludes mixing angles down to $\theta \sim 0.02$ in a narrow region around the B_d mass. This result can be significantly improved at Belle II [168], reaching $\theta \simeq 0.03$. Studying an additional signature, $B_s \to \not{E}$, could extend this region down to $\theta \simeq 0.008$.

The invisible scalar decay rate is also bounded from above by invisible Higgs decay measurements [173], as well as from the bounds on the Higgs coupling strength to visible matter[174]. Their projections at the HL-LHC provide the strongest bounds in the high-mass region, $m_S \gtrsim 5.7$ GeV, which we estimate as $\theta \lesssim 0.005$ and $\theta \lesssim 0.008$ correspondingly.

In summary, the invisible decays are sensitive to mixing angles down to $\theta \simeq 10^{-3}$. Interestingly, assuming dark decays of S being suppressed, displaced searches probe much smaller mixings.

5.3. Long-lived dark scalars in displaced searches

In the case dark decays $S \to \chi\bar{\chi}$ are negligible or kinematically forbidden, S lifetime is determined by the decay modes to the SM, shown in Figure 5.1. In Figure 5.4 we display the proper decay length[4] of S in the (m_S, θ)-plane. The scalar appears long-lived at detector scales already for $\theta \simeq 10^{-2}$ and its decay length scales quadratically with θ. Due to the flavor-hierarchical structure of the couplings (see Lagrangian in Equation (5.8)), the scalar's decays become displaced at mixings that still result in a decent production rate. For illustration, see Figure 5.2 where the blue (orange) point represents tiny (feasible) interactions.

Let on now focus on the cleanest, the semi-leptonic displaced decay modes of B mesons. Such decays can be studied at both proton-proton and electron-positron colliders. The former is characterized by the high center-of-mass collision energy, the latter benefits from much lower backgrounds.

At the LHC, searches for such signatures were performed by LHCb Collaboration. There, the analysis for the process $B^+ \to K^+ S(\to \mu\bar{\mu})$ [175] and $B^0 \to K^{*0} S(\to \mu\bar{\mu})$ [176] was done at collision energy $\sqrt{s} = 7$ and 8 TeV and integrated luminosity $\mathcal{L} = 3/\text{fb}$. We use the bound on the branching ratio of the charged B-meson at 95% derived in the former study to draw the corresponding exclusion regions in the (m_S, θ)-plane in Figure 5.3. The white vertical gaps in this plot correspond to the cut-out in the original analysis areas. There, due to high backgrounds, regions around K^0_S, J/ψ, $\psi(2S)$ and $\psi(3770)$ resonances are fully vetoed, and from ϕ and $\psi(4160)$ ones are partially-vetoed. Adding the neutral meson decays from the second study closes the gaps in the low-mass region, $m_S < 1$ GeV, excluding similar mixing angles (see e.g. [160]).

Importantly, the mixing angles excluded are about an order of magnitude smaller compared to prompt searches [178] (see [160] for details). Thus, similarly to the electroweak-scale Higgs portal case discussed in Chapter 4, displacement information is essential in searches for weakly coupled few-GeV-scale Higgs portal dark sectors at colliders.

Following Ref. [161], we estimated the reach of the same LHCb search at HL-LHC (HL-LHCb). The details of the calculation can be found in Appendix C. The estimate is based on rescaling the number of events due to increased B production cross section at $\sqrt{s} = 13$ TeV and $\mathcal{L} = 300/fb$, taking into account differences between prompt and displaced regions. The resulting projection predicts almost a factor of 5 improvement at small mixing angles and is shown as a blue line in Figure 5.3.

To date, semi-leptonic/semi-hadronic decays of B mesons at e^+e^- colliders were studied only in the context of inclusive searches of $\mathcal{B}(B \to X_s S)\mathcal{B}(S \to f)$ at BaBar [177]. There, decays to any s-containing final state, X_s, as well as to various displaced lepton and light meson final states were considered. The resulting upper limits on the mentioned branching ratio are provided for five values of the scalar's lifetime in range 1 cm $< c\tau <$ 1 m. We reinterpret their results for $f = \mu,\ \pi$, interpolating between the mentioned lifetimes. Nevertheless, the results are very patchy (see Figure 5.3, yellow and orange regions). We

[4] The proper decay length is defined as $c\tau_S$ where τ_S is the scalar's lifetime.

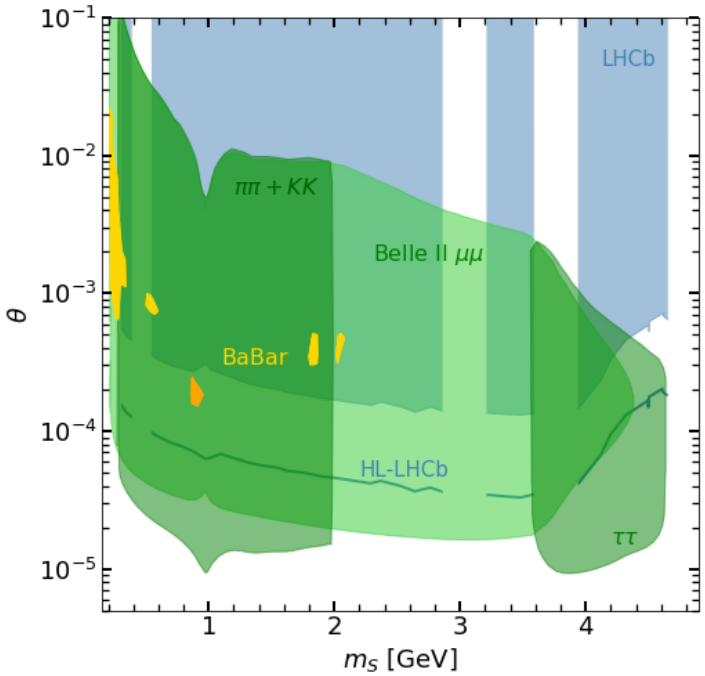

Figure 5.3: Searches for dark scalars at B factories. In blue, we show the 95% CL bounds from $B^+ \to K^+ S(\to \mu\bar{\mu})$ searches at LHCb [175]. The 90% CL bounds from the inclusive search by BaBar [177] is shown in yellow for $\mathcal{B}(B \to X_s S)\mathcal{B}(S \to f)$ with $f = \mu^+\mu^-$, and in orange – for $\pi^+\pi^-$. In green, we present the regions with 3 or more signal events at Belle II with 50/ab for $B \to KS(\to f)$ with $f = \mu^+\mu^-$, $\pi^+\pi^- + K^+K^-$ and $\tau^+\tau^-$. For comparison, we show projections for $B \to K\mu\bar{\mu}$ for the high-luminosity phase of LHCb (blue curve).

expect the patches would become bigger if more lifetime points were provided[5].

The result of BaBar already indicates that a dedicated search for displaced leptons/mesons at e^+e^- colliders would be at least competitive with similar searches at LHCb, and might even be able to go beyond the reach of the latter. Therefore, let us focus on the Belle II experiment that has just recently started operating.

Displaced signatures at Belle II

At Belle II, $B\bar{B}$ pairs are abundantly produced from decays of $\Upsilon(4S)$ resonance. In the center of mass frame (CMF) of the resonance, B mesons are almost at rest. However, due to an asymmetry of the beam energies (4 vs. 7 GeV), the mesons are boosted to the right of Figure 5.5. B mesons decay via $B \to KS(\to f)$ with K being either K^0, K^+, or K^*. Promising final states are $f = \pi^+\pi^-$, K^+K^- and $\mu^+\mu^-$ for scalar masses $m_S \lesssim 2\,\text{GeV}$ and $\tau^-\tau^+$, D^+D^- or 4π for heavier scalars. By detecting both the kaons and the final states f, the B meson momentum can be fully reconstructed, leading to strong background suppression. For its decay products to be detected with good precision, the scalar should decay at a radius between the vertex resolution and within the Central Drift Chamber (CDC), $500\,\mu\text{m} < \rho < 113$ cm. The latter can be in principle extended since the

[5] the break in the yellow region below $m_S = 0.5$ GeV is due to the cut-out in the original study mass values where high hadronic backgrounds are expected

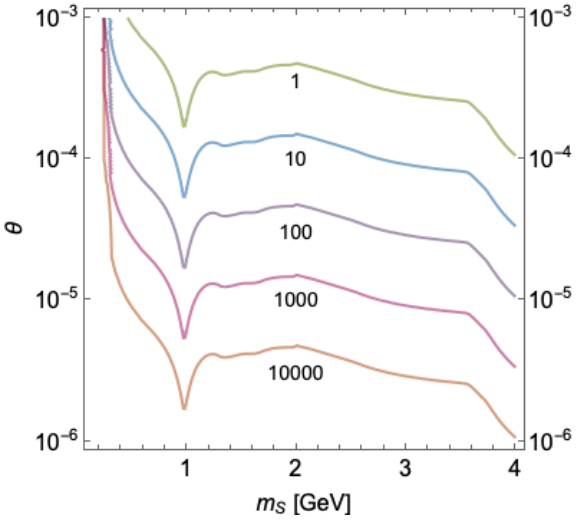

Figure 5.4: Proper decay length ($c\tau_S$) of dark scalar S in cm in the (m_S, θ) plane. Zero branching ration to dark fermions is assumed.

Electromagnetic Calorimeter (ECL) has tracking potential as well. However, we found only negligible improvements if the ECL is included in our analysis[6]. Scalars with larger lifetime freely escape the detector, creating a missing energy signal. The searches discussed in the previous section apply to them. The detector acceptance is limited to $17° < \vartheta < 150°$ in the polar angle (see Figure 5.5) and -125 cm $< z < 224$ cm around the collision point in the beam direction [168].

Considering the muon final state, we can calculate the expected number of muon pairs produced within this detector region as

$$N_{\mu\bar{\mu}} = N_{B\bar{B}} \times 1.93\, \mathcal{B}(B \to KS)\mathcal{B}(S \to \mu\bar{\mu}) \times \frac{1}{2} \int d\vartheta_0 \, \frac{\sin\vartheta_0}{d_S} \int dr \, e^{-\frac{r}{d_S}}, \tag{5.11}$$

where r is the radial distance from the e^+e^- interaction point (such that $\rho = r\sin\theta$), ϑ_0 is the polar angle of the scalar's momentum in the rest frame of the B meson and d_S is its decay length in the lab frame. The expected number of $B\bar{B}$ pairs (for both B^+ and B^0) at 50/ab is $N_{B\bar{B}} = 5 \times 10^{10}$, and the corresponding boost factor of the B meson is $\langle\gamma_B\rangle \approx 1.04$ [168]. The factor of 1.93 accounts for the different lifetimes of B^+ and B^0 [179].

Let us now focus on the calculations of the $\mathcal{B}(B \to KS)$ branching ratio. It differs for outgoing K mesons of different Lorentz structures. As an example, we provide the expression for B^+ and K^+ mesons:

$$\mathcal{B}(B^+ \to K^+S) = \frac{\sqrt{2}G_F\,|C_{bs}|^2}{64\pi\Gamma_{B^+}m_B^3} \frac{(m_b+m_s)^2}{(m_b-m_s)^2} f_0^2\big(m_S^2\big)\big(m_B^2-m_K^2\big)^2 \times \big[(m_B^2-m_K^2-m_S^2)^2 - 4m_K^2m_S^2\big]^{\frac{1}{2}}. \tag{5.12}$$

Here Γ_{B^+} is the total decay width of the B^+ meson and $f_0(m_S^2)$ is the scalar hadronic form

[6] Detecting particles inside the ECL end capsules would however significantly increase the detector's acceptance which would have a more pronounced effect.

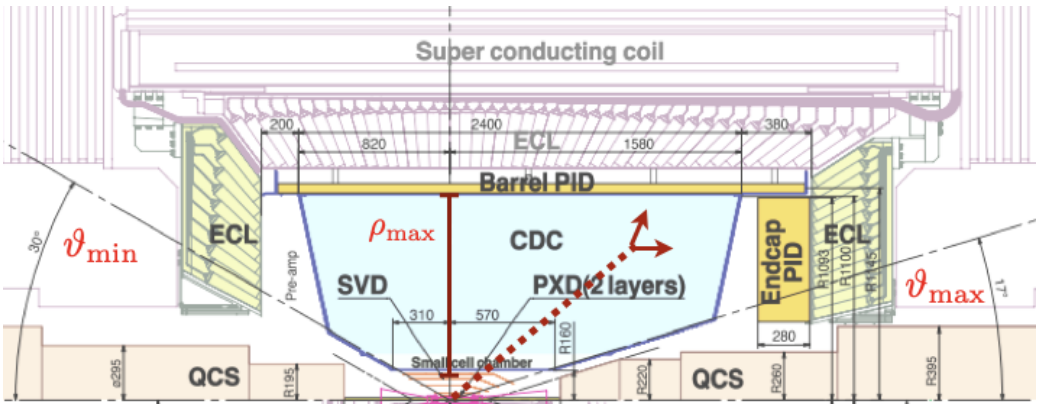

Figure 5.5: Illustration of the displaced scalar decay at Belle II. For more details on the experimental design, see [168].

factor at momentum transfer $q^2 = m_S^2$ [180]. Depending on the outgoing kaon, we use the general expressions derived in Ref. [179, 181] and adopt the currently most precise, to our knowledge, calculations of the corresponding $B \to K$ hadronic form factors. We use the input from lattice calculations [180] for the pseudo-scalar kaons, light-cone sum rules [182] for the vector resonance K^*_{892} and the approach of Ref. [179] for other kaons. The resulting branching ratios are shown in Figure 5.6[7]. In our analysis, we sum over all the contributions, gaining approximately a factor of two in sensitivity if compared to only one kaon state (see Appendix B of [149]). If, in addition to the displaced particles, the final-state kaon is detected, the B momentum can be reconstructed and the proposed search is expected to be almost background-free. Therefore, the parameter space of at least $N_{\mu\bar{\mu}} = 3$ displaced muon pairs from $B \to KS(\to \mu\bar{\mu})$ decays at Belle II that we show in Figure 5.3 corresponds to the rejection of the background-only hypothesis at 95% CL. Here we assume $\epsilon = 100\%$ efficiency[8], the significances of the search are expected to depend on ϵ as $S \propto (\epsilon)^{-1/2}$. The upper edge of the light green area is defined by the smallest distance from the collision point at which the muons are detected. The lower and right edges are due to small branching fractions to muons.[9] The overall slope of the area shows that smaller angles are better probed at high scalar masses (and thus shorter decay length) since a larger fraction of them decays within the detector.

We also show the same predictions for the $\pi^+\pi^- + K^+K^-$ and $\tau^+\tau^-$ final states since they improve the coverage for small and heavy scalars. Pion and kaon final states extend the reach to small angles for masses $m_S \simeq 1$ GeV, where the corresponding partial decay rates peak (see Figure 5.1). The sharp cut at $m_S = 2$ GeV is due to the non-reliability of the meson description at higher masses (see discussion at the end of Section 5.1). The smallest

[7] Note that measured masses of some of the kaons shown in Figure 5.6 slightly differ from the ones used in the naming convention. For details, see [4].

[8] The presence of background affects our results only mildly. For instance, by assuming three or fewer background events the sensitivity is reduced by at most a factor of two in θ. Systematic uncertainties on the signal and/or background could affect the sensitivity further, but can only be determined in a dedicated experimental analysis.

[9] For very light (and thus boosted) scalars, the lower edge is set by the maximum detectable distance.

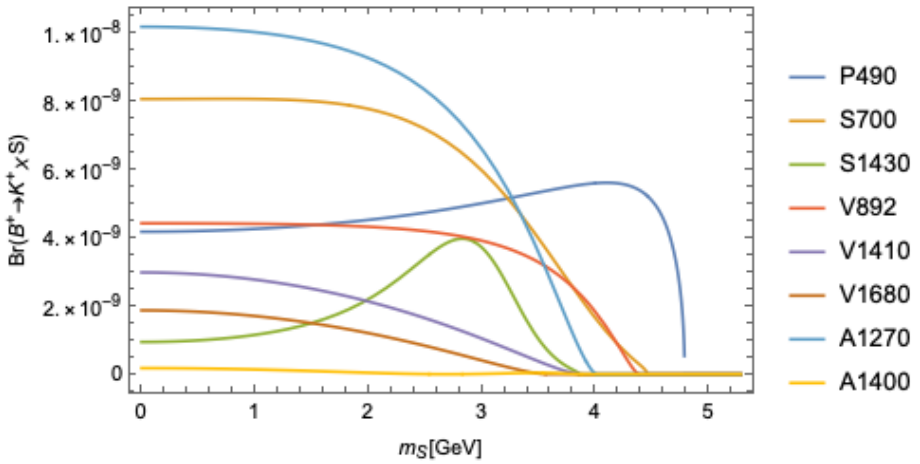

Figure 5.6: Branching ratios of the charged B meson to a kaon and the scalar. The letters in the legend indicate scalar, pseudo-scalar, vector and axial-vector K mesons. The numbers indicate the corresponding masses of the kaons in MeV.

and largest masses accessible by the tau channel are defined by the kinematics.

All in all, we see that displaced signatures have the potential of probing the parameter space of light scalars beyond the possible reach of the LHC. Moreover, they are complementary to fixed-target experiments.

The latter are shown in Figure 5.7. Here we compare the reach of Belle II and HL-LHCb to the future searches for displaced muons at NA62 in the beam-dump mode [160, 183], FASER [184] and FASER 2 [184, 185]. We would like to emphasize that Belle II has a similar sensitivity while having a much shorter baseline. We also show the projections for SHiP [186], CODEX-b [187] and MATHUSLA [188] which are sensitive to even smaller couplings.

5.4. Discussion

In this study, we proposed a new search for dark scalars of the few-GeV mass scale at Belle II. Similarly to the signatures proposed in Chapter 4, this search relies heavily on the displacement of the final products, leading to strong background suppression. In the present case, due to the additional measurement of the kaon in the final state and the subsequent reconstruction of the process, the signature is expected to be almost background-free. The results can be interpreted in a variety of DM models with scalar mediators that do not decay to other BSM particles. In the case scalar decays to DM are kinematically allowed, the limits should be rescaled with the appropriate branching ratio to the SM particles, $\mathcal{B}(S \to SM)$.

The mass range of S considered in this work is constrained by the kinematics of B-meson decays. However, long-lived particles in the mass region below our consideration suffer, in addition to the supernovae bounds mentioned in the previous section, from severe cosmological constraints [161, 189]. Scalars of very light mass, $m_S < 2m_e$, decay only to photons through a loop-suppressed coupling. They, therefore, act as relativistic DM, affecting BBN and CMB measurements. In the mass range $2m_e < m_S < 2m_\mu$ and at mixing angles

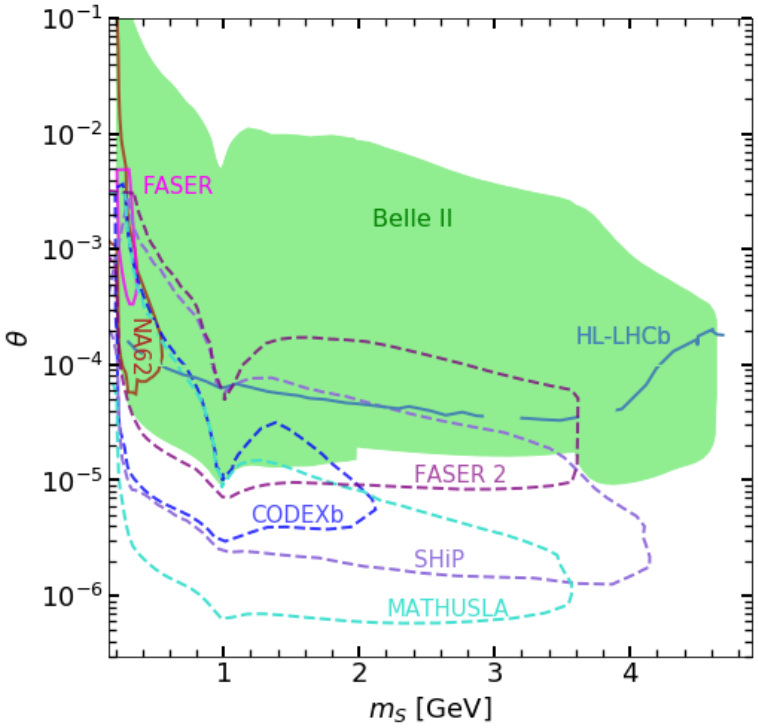

Figure 5.7: Comparison of the Belle II and LHCb and long-baseline experiments. The filled are is the combined sensitivity of the $\mu^+\mu^-$, $\pi^+\pi^-$, K^+K^- and $\tau^+\tau^-$ channels at Belle II. The lines show sensitivity projections for running or funded experiments (plain) and for proposed future experiments (dashed).

below $\theta \sim 10^{-5} - 10^{-4}$ (depending on the mass) the scalars decay around the BBN time. Thus, they both contribute to the energy density of the Universe and inject entropy into the SM sectors through decays.[10]. Regions with $m_S \lesssim 1$ GeV and $\theta \lesssim 10^{-5}$ require non-thermal mechanisms of DM production since such dark sectors never reach equilibrium with the SM plasma [161].

The simplest scenario with χ playing the role of thermal DM can be realized if $m_\chi > m_S$. In this case, the scalar decays away until the present time through its SM couplings, and χ (or another DM candidate) acts as CDM for an appropriate coupling y_χ. The calculation of the relic abundance, however, might require tracking number densities of both S and χ that are out of equilibrium. If $m_\chi < m_S$, thermal production of χ requires large couplings, excluded by current particle experiments [161, 190], so non-thermal mechanisms need to take place in order to ensure successful DM production.

Comparing LHCb and Belle II

Let us finally compare the performance of Belle II and LHCb in searching for the displaced muons in process $B^+ \to K^+ S(\to \mu\bar{\mu})$. The sensitivity to small couplings is dictated by the ability of scalars to decay within the detector volume of an experiment. This is the reason why the long-baseline experiments plotted in Figure 5.7 probe much smaller mixing angles.

[10]There is, however, a potential gap at $\theta \sim 10^{-4}$ that is not excluded from cosmological observation and is not yet covered by kaon experiments [160].

The LHCb analysis [175] requires scalar decays within 60 cm from the primary vertex (to get at least one hit inside the vertex detector), whereas at Belle II particles can fly longer than 1 m and still be detected. Moreover, due to larger boost, scalars tend to decay farther at the LHCb: at the end particles with the nominal decay length of $c\tau_S \lesssim 30$ cm are detected. To compare, at Belle II B mesons are produced almost at rest and decay length up to $c\tau_S \sim 10$ m leave a signal in the CDC. However, due to high integrated luminosity, LHCb can extend its reach dramatically (see Figure 5.3). An interesting conclusion is that experiments with low boosted particles can successfully compete with the long-baseline experiments in displaced searches.

6. Conclusion

Dark matter hunting is entering a new era due to ever stronger direct detection constraints. Viable DM candidates are forced to be lighter than the GeV scale, heavier than the TeV scale or to have extremely small couplings to the SM. Taking into account a combination of collider and, for lighter particles, astrophysical/cosmological constraints (see, Chapters 3 and 5), it might seem that thermal dark matter candidates, if existing, are beyond the reach of modern experiments.

In this thesis, we point out that while the experimental techniques that will allow probing the currently inaccessible DM masses are under development, it is important to revise the underlying physics assumption of the present experimental setup. The reason next-to-minimal thermal DM models have not been found yet might be the kinematic cuts used in the WIMP experimental analyses.

In Chapters 3 and 4, we showed that while simple WIMPs are indeed in tension with observations, extended dark sectors provide DM candidates that are in perfect agreement with current experiments. We further noticed that the observable DM relic abundance *unavoidably implies compressed dark spectra* for these models. This results in the presence of mediators that are long-lived at collider scales and *naturally leads to soft displaced signatures at colliders*. For example, in the electroweak-scale Higgs portal DM models, visible products of mediator decays have transverse momenta of $p_T \sim 10 - 50$ GeV meaning that most of these theories *can not be detected with the momentum cuts set by the triggers currently used at CMS and ATLAS*. Luckily, these models *could be tested with already existing techniques with appropriate adjustments to the analysis and trigger strategy*. The reason is small DM-SM couplings that play in our favor. By setting up an analysis that relies on the particles' displacements, the SM background can be significantly reduced. Already existing displaced searches support this hypothesis showing the potential for covering parameter space of the models of interest far beyond the reach of prompt searches. The singlet-triplet Higgs portal model, studied in Chapter 4 can serve as a minimalistic toy model for such searches since, depending on the area of the parameter space, it provides various displaced signatures.

Taking this model as an example, we also indicate an almost non-discussed in the literature DM production mechanism, *the co-scattering mechanism*. We point out that it appears in many models that feature co-annihilation if DM-SM couplings are further decreased. The accurate model-independent prediction of the DM relic abundance in the co-scattering regime is *currently an unsolved task* due to numerous technical complications discussed in Chapter 4. Importantly, this scenario is most likely to require similar or even more compressed spectra than co-annihilation, making the LLP searches even more urgent. The co-scattering regime

can be viewed as a production mechanism in between of the conventional freeze-out and freeze-in scenarios. It belongs to the class of models in which kinetic decoupling of the dark sector can occur before the chemical one.

In Chapter 5 we test the power of displaced searches in probing few-GeV-scale dark sectors exploring the phenomenology of a BSM scalar that acts as a mediator to DM. We start from reinterpreting an analysis of displaced objects in rare B meson decays by BaBar which is not optimized to the considered model. The results already show promising sensitivity of displaced searches at e^+e^- colliders, comparable with some dedicated LLP experiments. We, therefore, study further the exclusion power of displaces analyses, focusing on the Belle II experiment and optimizing the search such that it becomes almost background-free. We show that this setup allows Belle II to compete with FASER, FASER 2 and NA62 in the beam-dump mode, as well as with some of the proposed experiments while having a much shorter baseline.

All in all, LLP searches provide new opportunities for the DM community. They make whole classes of phenomenologically motivated models experimentally accessible and hopefully will shed light on one of the biggest mysteries of our Universe, the dark matter.

7. Acknowledgments

As my doctoral studies are coming to end, I would like to use this opportunity to thank so many wonderful people without whom I would have never had so much courage and fun working on this thesis.

First of all, I would like to thank my advisor, Susanne Westhoff, for all the inspiration and support I started receiving from day one in Heidelberg. I would also like to express my gratitude for the freedom I had during this time which allowed me to develop my own vision of many aspects of particle physics. I am extremely grateful for the unique atmosphere where I would constantly learn so many things from her and, at the same time, would feel the excitement to share my ideas. I am also very thankful for the opportunity to take part in many conferences and give many seminar talks. It definitely helped me improve my presentation skills a lot, as well as expand my views on state-of-the-art research across the globe.

I would like to thank Joerg Jaeckel for refereeing this thesis, as well as Monica Dunford and Matthias Bartelmann for interesting physics discussions during these years and for completing my examination committee.

I furthermore gratefully acknowledge financial, scientific and social support from the Research Training Group "Particle Physics at the LHC" and the Heidelberg Graduate School for Physics. In particular, I would like to acknowledge the support of our female community for useful and fun social events and training programs. I would also like to personally thank Monica Dunford for her help with my postdoctoral application materials.

I thank my collaborators and many great scientists I had a pleasure to hold scientific discussions with. I am particularly thankful to all the experimental colleagues for their patience when explaining details of experimental analyses and designs.

I am extremely grateful to my proof-readers, Anke Biekötter (thank you also for the German translation!), Sebastian Bruggisser, Andrii Magalich, Peter Reimitz, Ruth Schäfer and Ramon Winterhalder for making this piece of text readable. All the remaining imperfections are exclusively on my account. A particularly big thank-you goes to Peter Reimitz and Ruth Schäfer who proofread major parts of this thesis.

I would like to thank Gonzalo Alonso-Álvarez, Marco Bellagente, Anke Biekötter, Sebastian Bruggisser, Anja Butter, Patrick Foldenauer, Renata Kopečná, Michel Luchmann, Peter Reimitz, Michael Russell, Sebastian Schenk, Jennie Thompson, Lennert Thormaehlen and Ramon Winterhalder for becoming my family during these three years. I am extremely happy to share with you the experience of seeing the Karlsruhe light show, playing Rundlauf, surviving Wasen, sledding, singing the "Hundi" song, learning to play Bosseln, exploring the

nightlife in Granada and dying hair. Our “usual” activities that taught me how to have fun “German-style” and made me learn lyrics of all the party songs (thanks, Ramon!) will always be in my heart. I would also like to thank my fellas Petar Andrejić, Daniel Bakucz-Canario, Kamil Dzikowski, Anja Kunz, and Archana Sampath for all the fun we had in Heidelberg and its surroundings. I was very lucky to find good friends here, and I really hope to keep our friendship trough space and time.

At this point, I would like to acknowledge my Alma mater, the Chair of Quantum Field Theory of the Taras Shevchenko National University of Kyiv and the Scientific and Educational Center of Bogolyubov Institute for Theoretical Physics in Kyiv. I am very grateful to the outstanding lecturers who laid the foundation of my physical thinking. I am particularly grateful to Vitaly Shadura for organizing so many interesting seminars that triggered my passion for physics. I would also like to thank Alexey Boyarsky and Oleg Ruchaiskiy for introducing me to the world of astroparticle phenomenology, as well as Kyrylo Bondarenko and Andrii Magalich for teaching me many aspects of particle physics and cosmology.

I am very grateful to all my friends with whom we started our journey in science. I am very lucky that even now, being in different parts of the world, we continue our journey together. I am also thankful to my dear friends outside science for keeping my mind open and for being so inspiring.

Finally, I would never be able to finish this thesis without the support and faith of my parents, Natalia and Stanislav, as well as my grandparents, Maria and Borys. I cannot express my gratitude to Vitya who was always there for me, motivating and having my back at all times, sharing with me the scientific journey and supporting the craziest of my ideas.

Bibliography

[1] B. Kelvin, *Baltimore lectures on molecular dynamics and the wave theory of light (1904)*.

[2] H. Poincaré and J. Royce, "The milky way and the theory of gases," in *The Foundations of Science: Science and Hypothesis, The Value of Science, Science and Method*, G. B. Halsted, Ed., ser. Cambridge Library Collection - History of Science. Cambridge University Press, 2014, 523–534. DOI: 10.1017/CBO9781107252950.043.

[3] H. Andernach and F. Zwicky, "English and Spanish Translation of Zwicky's (1933) The Redshift of Extragalactic Nebulae," *arXiv e-prints*, arXiv:1711.01693, arXiv:1711.01693, Nov. 2017. arXiv: 1711.01693 [astro-ph.IM].

[4] M. Tanabashi *et al.*, "Review of Particle Physics," *Phys. Rev. D*, vol. 98, no. 3, p. 030 001, 2018. DOI: 10.1103/PhysRevD.98.030001.

[5] Y. Sofue and V. Rubin, "Rotation curves of spiral galaxies," *Ann. Rev. Astron. Astrophys.*, vol. 39, pp. 137–174, 2001. DOI: 10.1146/annurev.astro.39.1.137. arXiv: astro-ph/0010594 [astro-ph].

[6] V. C. Rubin, W. K. Ford Jr., and N. Thonnard, "Extended rotation curves of high-luminosity spiral galaxies. IV. Systematic dynamical properties, Sa through Sc," *Astrophys. J.*, vol. 225, pp. L107–L111, 1978. DOI: 10.1086/182804.

[7] M. Lisanti, "Lectures on Dark Matter Physics," in *Proceedings, Theoretical Advanced Study Institute in Elementary Particle Physics: New Frontiers in Fields and Strings (TASI 2015): Boulder, CO, USA, June 1-26, 2015*, 2017, pp. 399–446. DOI: 10.1142/9789813149441_0007. arXiv: 1603.03797 [hep-ph].

[8] M. L. Mateo, "Dwarf Galaxies of the Local Group,", vol. 36, pp. 435–506, Jan. 1998. DOI: 10.1146/annurev.astro.36.1.435. arXiv: astro-ph/9810070 [astro-ph].

[9] D. Gorbunov and V. Rubakov, *Introduction to the Theory of the Early Universe: Cosmological Perturbations and Inflationary Theory*, ser. Introduction to the Theory of the Early Universe: Cosmological Perturbations and Inflationary Theory. World Scientific, 2011, ISBN: 9789814322225. [Online]. Available: https://books.google.de/books?id=BeFF7zzrx_wC.

[10] M. Walker, "Dark matter in the galactic dwarf spheroidal satellites," in *Planets, Stars and Stellar Systems: Volume 5: Galactic Structure and Stellar Populations*, T. D. Oswalt and G. Gilmore, Eds. Dordrecht: Springer Netherlands, 2013, pp. 1039–1089,

ISBN: 978-94-007-5612-0. DOI: 10.1007/978-94-007-5612-0_20. [Online]. Available: https://doi.org/10.1007/978-94-007-5612-0_20.

[11] E. Battaner and E. Florido, "The Rotation curve of spiral galaxies and its cosmological implications," *Fund. Cosmic Phys.*, vol. 21, pp. 1–154, 2000. arXiv: astro-ph/0010475 [astro-ph].

[12] S. Giodini, L. Lovisari, E. Pointecouteau, S. Ettori, T. H. Reiprich, and H. Hoekstra, "Scaling relations for galaxy clusters: properties and evolution," *Space Sci. Rev.*, vol. 177, pp. 247–282, 2013. DOI: 10.1007/s11214-013-9994-5. arXiv: 1305.3286 [astro-ph.CO].

[13] A. D. Lewis, D. A. Buote, and J. T. Stocke, "Chandra observations of Abell 2029: The Dark matter profile at < 0.01 R(VIR) in an unusually relaxed cluster," *Astrophys. J.*, vol. 586, pp. 135–142, 2003. DOI: 10.1086/367556. arXiv: astro-ph/0209205 [astro-ph].

[14] R. Massey *et al.*, "Dark matter maps reveal cosmic scaffolding," *Nature*, vol. 445, p. 286, 2007. DOI: 10.1038/nature05497. arXiv: astro-ph/0701594 [astro-ph].

[15] S. Tulin and H.-B. Yu, "Dark Matter Self-interactions and Small Scale Structure," *Phys. Rept.*, vol. 730, pp. 1–57, 2018. DOI: 10.1016/j.physrep.2017.11.004. arXiv: 1705.02358 [hep-ph].

[16] K. Bondarenko, A. Boyarsky, T. Bringmann, and A. Sokolenko, "Constraining self-interacting dark matter with scaling laws of observed halo surface densities," *JCAP*, vol. 04, p. 049, 2018. DOI: 10.1088/1475-7516/2018/04/049. arXiv: 1712.06602 [astro-ph.CO].

[17] N. Aghanim *et al.*, "Planck 2018 results. VI. Cosmological parameters," 2018. arXiv: 1807.06209 [astro-ph.CO].

[18] V. A. Rubakov and A. D. Vlasov, "What do we learn from CMB observations," *Phys. Atom. Nucl.*, vol. 75, pp. 1123–1141, 2012. DOI: 10.1134/S1063778812090116. arXiv: 1008.1704 [astro-ph.CO].

[19] A. Magalich, "Probing the properties of dark matter particles with astrophysical observations," PhD thesis, Leiden University, 2019. [Online]. Available: http://hdl.handle.net/1887/82071.

[20] M. Milgrom, "A modification of the Newtonian dynamics as a possible alternative to the hidden mass hypothesis.", vol. 270, pp. 365–370, Jul. 1983. DOI: 10.1086/161130.

[21] J. D. Bekenstein, "Relativistic gravitation theory for the MOND paradigm," *Phys. Rev.*, vol. D70, p. 083 509, 2004, [Erratum: Phys. Rev.D71,069901(2005)]. DOI: 10.1103/PhysRevD.70.083509,10.1103/PhysRevD.71.069901. arXiv: astro-ph/0403694 [astro-ph].

[22] M. Lisanti, M. Moschella, N. J. Outmezguine, and O. Slone, "Testing Dark Matter and Modifications to Gravity using Local Milky Way Observables," *Phys. Rev.*, vol. D100, no. 8, p. 083 009, 2019. DOI: 10.1103/PhysRevD.100.083009. arXiv: 1812.08169 [astro-ph.GA].

[23] J. Zuntz, T. G Zlosnik, F. Bourliot, P. G. Ferreira, and G. D. Starkman, "Vector field models of modified gravity and the dark sector," *Phys. Rev.*, vol. D81, p. 104 015, 2010. DOI: 10.1103/PhysRevD.81.104015. arXiv: 1002.0849 [astro-ph.CO].

[24] C. Skordis, D. F. Mota, P. G. Ferreira, and C. Boehm, "Large Scale Structure in Bekenstein's theory of relativistic Modified Newtonian Dynamics," *Phys. Rev. Lett.*, vol. 96, p. 011 301, 2006. DOI: 10.1103/PhysRevLett.96.011301. arXiv: astro-ph/0505519 [astro-ph].

[25] K. Griest, *Wimps and machos*, Encyclopedia of Astronomy and Astrophysics.

[26] M. Scodeggio and G. Gavazzi, "21 Centimeter Study of Spiral Galaxies in Clusters. III. Neutral Gas Content, Star Formation, and Radio Continuum Properties,", vol. 409, p. 110, May 1993. DOI: 10.1086/172645.

[27] C. Carignan and K. C. Freeman, "DDO 154: A "Dark" Galaxy?", vol. 332, p. L33, Sep. 1988. DOI: 10.1086/185260.

[28] T. D. Brandt, "Constraints on MACHO Dark Matter from Compact Stellar Systems in Ultra-Faint Dwarf Galaxies," *Astrophys. J.*, vol. 824, no. 2, p. L31, 2016. DOI: 10.3847/2041-8205/824/2/L31. arXiv: 1605.03665 [astro-ph.GA].

[29] J. García-Bellido and S. Clesse, "Constraints from microlensing experiments on clustered primordial black holes," *Phys. Dark Univ.*, vol. 19, pp. 144–148, 2018. DOI: 10.1016/j.dark.2018.01.001. arXiv: 1710.04694 [astro-ph.CO].

[30] S. Tremaine and J. E. Gunn, "Dynamical role of light neutral leptons in cosmology," *Phys. Rev. Lett.*, vol. 42, pp. 407–410, 6 1979. DOI: 10.1103/PhysRevLett.42.407. [Online]. Available: https://link.aps.org/doi/10.1103/PhysRevLett.42.407.

[31] A. Boyarsky, O. Ruchayskiy, and D. Iakubovskyi, "A Lower bound on the mass of Dark Matter particles," *JCAP*, vol. 0903, p. 005, 2009. DOI: 10.1088/1475-7516/2009/03/005. arXiv: 0808.3902 [hep-ph].

[32] M. Aker *et al.*, "Improved Upper Limit on the Neutrino Mass from a Direct Kinematic Method by KATRIN," *Phys. Rev. Lett.*, vol. 123, no. 22, p. 221 802, 2019. DOI: 10.1103/PhysRevLett.123.221802. arXiv: 1909.06048 [hep-ex].

[33] L. Canetti, M. Drewes, T. Frossard, and M. Shaposhnikov, "Dark Matter, Baryogenesis and Neutrino Oscillations from Right Handed Neutrinos," *Phys. Rev. D*, vol. 87, p. 093 006, 2013. DOI: 10.1103/PhysRevD.87.093006. arXiv: 1208.4607 [hep-ph].

[34] M. Aoki, S. Kanemura, and O. Seto, "Neutrino mass, Dark Matter and Baryon Asymmetry via TeV-Scale Physics without Fine-Tuning," *Phys. Rev. Lett.*, vol. 102, p. 051 805, 2009. DOI: 10.1103/PhysRevLett.102.051805. arXiv: 0807.0361 [hep-ph].

[35] W.-M. Yang, "A model of neutrino mass, baryon asymmetry, and asymmetric dark matter with $SU(2)_D \otimes U(1)_{D'}$ dark sector," *Nucl. Phys.*, vol. B, p. 114 643, 2019. DOI: 10.1016/j.nuclphysb.2019.114643. arXiv: 1807.03036 [hep-ph].

[36] K. Kadota, T. Sekiguchi, and H. Tashiro, "A new constraint on millicharged dark matter from galaxy clusters," 2016. arXiv: 1602.04009 [astro-ph.CO].

[37] A. Boyarsky, *Lecture notes on dark matter*, http://wwwhome.lorentz.leidenuniv.nl/~boyarsky/media/PPEU-2015-DM-lecture7.pdf.

[38] M. Davis, G. Efstathiou, C. S. Frenk, and S. D. M. White, "The evolution of large-scale structure in a universe dominated by cold dark matter,", vol. 292, pp. 371–394, May 1985. DOI: 10.1086/163168.

[39] D. H. Weinberg, J. S. Bullock, F. Governato, R. Kuzio de Naray, and A. H. G. Peter, "Cold dark matter: controversies on small scales," *Proc. Nat. Acad. Sci.*, vol. 112, pp. 12 249–12 255, 2015. DOI: 10.1073/pnas.1308716112. arXiv: 1306.0913 [astro-ph.CO].

[40] M. R. Lovell, W. Hellwing, A. Ludlow, J. Zavala, A. Robertson, A. Fattahi, C. S. Frenk, and J. Hardwick, "Local Group star formation in warm and self-interacting dark matter cosmologies," 2020. arXiv: 2002.11129 [astro-ph.GA].

[41] M. R. Lovell, C. S. Frenk, V. R. Eke, A. Jenkins, L. Gao, and T. Theuns, "The properties of warm dark matter haloes," *Mon. Not. Roy. Astron. Soc.*, vol. 439, pp. 300–317, 2014. DOI: 10.1093/mnras/stt2431. arXiv: 1308.1399 [astro-ph.CO].

[42] J. Baur, N. Palanque-Delabrouille, C. Yèche, C. Magneville, and M. Viel, "Lyman-alpha Forests cool Warm Dark Matter," *JCAP*, vol. 1608, no. 08, p. 012, 2016. DOI: 10.1088/1475-7516/2016/08/012. arXiv: 1512.01981 [astro-ph.CO].

[43] A. Garzilli, O. Ruchayskiy, A. Magalich, and A. Boyarsky, "How warm is too warm? Towards robust Lyman-α forest bounds on warm dark matter," 2019. arXiv: 1912.09397 [astro-ph.CO].

[44] M. Dine, "TASI lectures on the strong CP problem," in *Flavor physics for the millennium. Proceedings, Theoretical Advanced Study Institute in elementary particle physics, TASI 2000, Boulder, USA, June 4-30, 2000*, Jun. 2000, pp. 349–369. arXiv: hep-ph/0011376.

[45] Z.-z. Xing, "Quark Mass Hierarchy and Flavor Mixing Puzzles," *Int. J. Mod. Phys. A*, vol. 29, p. 1 430 067, 2014. DOI: 10.1142/S0217751X14300671. arXiv: 1411.2713 [hep-ph].

[46] M. Shaposhnikov and A. Shkerin, "Gravity, Scale Invariance and the Hierarchy Problem," *JHEP*, vol. 10, p. 024, 2018. DOI: 10.1007/JHEP10(2018)024. arXiv: 1804.06376 [hep-th].

[47] D. B. Kaplan, "Five lectures on effective field theory," Oct. 2005. arXiv: nucl-th/0510023.

[48] A. M. Hillas, "Cosmic Rays: Recent Progress and some Current Questions," in *Conference on Cosmology, Galaxy Formation and Astro-Particle Physics on the Pathway to the SKA*, Jul. 2006. arXiv: astro-ph/0607109.

[49] L. A. Anchordoqui, "Ultra-High-Energy Cosmic Rays," *Phys. Rept.*, vol. 801, pp. 1–93, 2019. DOI: 10.1016/j.physrep.2019.01.002. arXiv: 1807.09645 [astro-ph.HE].

[50] B. Batell, M. Pospelov, and A. Ritz, "Exploring Portals to a Hidden Sector Through Fixed Targets," *Phys. Rev.*, vol. D80, p. 095 024, 2009. DOI: 10.1103/PhysRevD.80.095024. arXiv: 0906.5614 [hep-ph].

[51] A. V. Manohar, "Introduction to Effective Field Theories," in *Les Houches summer school: EFT in Particle Physics and Cosmology*, Apr. 2018. arXiv: 1804.05863 [hep-ph].

[52] I. Brivio and M. Trott, "The Standard Model as an Effective Field Theory," *Phys. Rept.*, vol. 793, pp. 1–98, 2019. DOI: 10.1016/j.physrep.2018.11.002. arXiv: 1706.08945 [hep-ph].

[53] S. Weinberg, *The Quantum theory of fields. Vol. 1: Foundations*. Cambridge University Press, Jun. 2005, ISBN: 978-0-521-67053-1, 978-0-511-25204-4.

[54] P. Foldenauer, "Phenomenology of Extra Abelian Gauge Symmetries," PhD thesis, U. Heidelberg (main), 2019-07-03. DOI: 10.11588/heidok.00026777. [Online]. Available: http://archiv.ub.uni-heidelberg.de/volltextserver/26777/.

[55] J. Jaeckel and A. Ringwald, "The Low-Energy Frontier of Particle Physics," *Ann. Rev. Nucl. Part. Sci.*, vol. 60, pp. 405–437, 2010. DOI: 10.1146/annurev.nucl.012809.104433. arXiv: 1002.0329 [hep-ph].

[56] M. Raggi and V. Kozhuharov, "Results and perspectives in dark photon physics," *Riv. Nuovo Cim.*, vol. 38, no. 10, pp. 449–505, 2015. DOI: 10.1393/ncr/i2015-10117-9.

[57] J. Beacham *et al.*, "Physics Beyond Colliders at CERN: Beyond the Standard Model Working Group Report," *J. Phys.*, vol. G47, no. 1, p. 010 501, 2020. DOI: 10.1088/1361-6471/ab4cd2. arXiv: 1901.09966 [hep-ex].

[58] M. Bauer, P. Foldenauer, and J. Jaeckel, "Hunting All the Hidden Photons," *JHEP*, vol. 07, p. 094, 2018, [JHEP18,094(2020)]. DOI: 10.1007/JHEP07(2018)094. arXiv: 1803.05466 [hep-ph].

[59] V. A. Rubakov and D. S. Gorbunov, *Introduction to the Theory of the Early Universe*. Singapore: World Scientific, 2017, ISBN: 9789813209879, 9789813209886, 9789813220058. DOI: 10.1142/10447. [Online]. Available: http://www.DESY.eblib.com/patron/FullRecord.aspx?p=737614.

[60] R. Jacobsson, "Search for heavy sterile neutrinos with SHiP," CERN, Geneva, Tech. Rep. CERN-SHiP-PROC-2016-007, 2016. [Online]. Available: https://cds.cern.ch/record/2130433.

[61] V. Barger, P. Langacker, M. McCaskey, M. J. Ramsey-Musolf, and G. Shaughnessy, "LHC Phenomenology of an Extended Standard Model with a Real Scalar Singlet," *Phys. Rev.*, vol. D77, p. 035 005, 2008. DOI: 10.1103/PhysRevD.77.035005. arXiv: 0706.4311 [hep-ph].

[62] M. Kumar, S. von Buddenbrock, N. Chakrabarty, A. S. Cornell, D. Kar, T. Mandal, B. Mellado, B. Mukhopadhyaya, and R. G. Reed, "The impact of additional scalar bosons at the LHC," *J. Phys. Conf. Ser.*, vol. 802, no. 1, p. 012 007, 2017. DOI: 10.1088/1742-6596/802/1/012007. arXiv: 1603.01208 [hep-ph].

[63] T. Robens, T. Stefaniak, and J. Wittbrodt, "Two-real-scalar-singlet extension of the SM: LHC phenomenology and benchmark scenarios," *Eur. Phys. J.*, vol. C80, no. 2, p. 151, 2020. DOI: 10.1140/epjc/s10052-020-7655-x. arXiv: 1908.08554 [hep-ph].

[64] S. W. Ham, Y. S. Jeong, and S. K. Oh, "Electroweak phase transition in an extension of the standard model with a real Higgs singlet," *J. Phys.*, vol. G31, no. 8, pp. 857–871, 2005. DOI: 10.1088/0954-3899/31/8/017. arXiv: hep-ph/0411352 [hep-ph].

[65] T. Lin, "Dark matter models and direct detection," *PoS*, vol. 333, p. 009, 2019. DOI: 10.22323/1.333.0009. arXiv: 1904.07915 [hep-ph].

[66] M. Bauer and T. Plehn, "Yet Another Introduction to Dark Matter," *Lect. Notes Phys.*, vol. 959, pp.–, 2019. DOI: 10.1007/978-3-030-16234-4. arXiv: 1705.01987 [hep-ph].

[67] L. Hui, J. P. Ostriker, S. Tremaine, and E. Witten, "Ultralight scalars as cosmological dark matter," *Phys. Rev. D*, vol. 95, no. 4, p. 043 541, 2017. DOI: 10.1103/PhysRevD.95.043541. arXiv: 1610.08297 [astro-ph.CO].

[68] G. Gelmini and C. E. Yaguna, "Constraints on Minimal SUSY models with warm dark matter neutralinos," *Phys. Lett.*, vol. B643, pp. 241–245, 2006. DOI: 10.1016/j.physletb.2006.10.063. arXiv: hep-ph/0607012 [hep-ph].

[69] W. Buchmuller, "Gravitino Dark Matter," *AIP Conf. Proc.*, vol. 1200, no. 1, pp. 155–164, 2010. DOI: 10.1063/1.3327554. arXiv: 0910.1870 [hep-ph].

[70] A. Boyarsky, M. Drewes, T. Lasserre, S. Mertens, and O. Ruchayskiy, "Sterile Neutrino Dark Matter," *Prog. Part. Nucl. Phys.*, vol. 104, pp. 1–45, 2019. DOI: 10.1016/j.ppnp.2018.07.004. arXiv: 1807.07938 [hep-ph].

[71] J. Baur, N. Palanque-Delabrouille, C. Yeche, A. Boyarsky, O. Ruchayskiy, [U+FFFD] Armengaud, and J. Lesgourgues, "Constraints from Ly-α forests on non-thermal dark matter including resonantly-produced sterile neutrinos," *JCAP*, vol. 12, p. 013, 2017. DOI: 10.1088/1475-7516/2017/12/013. arXiv: 1706.03118 [astro-ph.CO].

[72] A. Boyarsky, J. Franse, D. Iakubovskyi, and O. Ruchayskiy, "Checking the Dark Matter Origin of a 3.53 keV Line with the Milky Way Center," *Phys. Rev. Lett.*, vol. 115, p. 161 301, 2015. DOI: 10.1103/PhysRevLett.115.161301. arXiv: 1408.2503 [astro-ph.CO].

[73] G. Bertone, D. Hooper, and J. Silk, "Particle dark matter: Evidence, candidates and constraints," *Phys. Rept.*, vol. 405, pp. 279–390, 2005. DOI: 10.1016/j.physrep.2004.08.031. arXiv: hep-ph/0404175.

[74] L. Roszkowski, E. M. Sessolo, and S. Trojanowski, "WIMP dark matter candidates and searches—current status and future prospects," *Rept. Prog. Phys.*, vol. 81, no. 6, p. 066 201, 2018. DOI: 10.1088/1361-6633/aab913. arXiv: 1707.06277 [hep-ph].

[75] J.-C. Park and S. C. Park, "A testable scenario of WIMPZILLA with Dark Radiation," *Phys. Lett. B*, vol. 728, pp. 41–44, 2014. DOI: 10.1016/j.physletb.2013.11.027. arXiv: 1305.5013 [hep-ph].

[76] E. W. Kolb and A. J. Long, "Superheavy dark matter through Higgs portal operators," *Phys. Rev. D*, vol. 96, no. 10, p. 103 540, 2017. DOI: 10.1103/PhysRevD.96.103540. arXiv: 1708.04293 [astro-ph.CO].

[77] Y. Bai, A. J. Long, and S. Lu, "Dark Quark Nuggets," *Phys. Rev.*, vol. D99, no. 5, p. 055 047, 2019. DOI: 10.1103/PhysRevD.99.055047. arXiv: 1810.04360 [hep-ph].

[78] S. Troitsky, "Supermassive dark-matter Q-balls in galactic centers?" *JCAP*, vol. 11, p. 027, 2016. DOI: 10.1088/1475-7516/2016/11/027. arXiv: 1510.07132 [hep-ph].

[79] C. Rott, "Status of Dark Matter Searches (Rapporteur Talk)," *PoS*, vol. ICRC2017, p. 1119, 2018, [35,1119(2017)]. DOI: 10.22323/1.301.1119. arXiv: 1712.00666 [astro-ph.HE].

[80] M. Boudaud *et al.*, "What do Galactic electrons and positrons tell us about dark matter?" *PoS*, vol. ICRC2017, p. 915, 2018. DOI: 10.22323/1.301.0915.

[81] M. G. Aartsen *et al.*, "Search for Neutrinos from Dark Matter Self-Annihilations in the center of the Milky Way with 3 years of IceCube/DeepCore," *Eur. Phys. J.*, vol. C77, no. 9, p. 627, 2017. DOI: 10.1140/epjc/s10052-017-5213-y. arXiv: 1705.08103 [hep-ex].

[82] J. Billard, L. Strigari, and E. Figueroa-Feliciano, "Implication of neutrino backgrounds on the reach of next generation dark matter direct detection experiments," *Phys. Rev.*, vol. D89, no. 2, p. 023 524, 2014. DOI: 10.1103/PhysRevD.89.023524. arXiv: 1307.5458 [hep-ph].

[83] G. Belanger, F. Boudjema, A. Pukhov, and A. Semenov, "Dark matter direct detection rate in a generic model with micrOMEGAs 2.2," *Comput. Phys. Commun.*, vol. 180, pp. 747–767, 2009. DOI: 10.1016/j.cpc.2008.11.019. arXiv: 0803.2360 [hep-ph].

[84] E. Aprile *et al.*, "The XENON1T Dark Matter Experiment," *Eur. Phys. J.*, vol. C77, no. 12, p. 881, 2017. DOI: 10.1140/epjc/s10052-017-5326-3. arXiv: 1708.07051 [astro-ph.IM].

[85] T. Bringmann and M. Pospelov, "Novel direct detection constraints on light dark matter," *Phys. Rev. Lett.*, vol. 122, no. 17, p. 171 801, 2019. DOI: 10.1103/PhysRevLett.122.171801. arXiv: 1810.10543 [hep-ph].

[86] R. Essig, M. Fernandez-Serra, J. Mardon, A. Soto, T. Volansky, and T.-T. Yu, "Direct Detection of sub-GeV Dark Matter with Semiconductor Targets," *JHEP*, vol. 05, p. 046, 2016. DOI: 10.1007/JHEP05(2016)046. arXiv: 1509.01598 [hep-ph].

[87] S. Derenzo, R. Essig, A. Massari, A. Soto, and T.-T. Yu, "Direct Detection of sub-GeV Dark Matter with Scintillating Targets," *Phys. Rev.*, vol. D96, no. 1, p. 016 026, 2017. DOI: 10.1103/PhysRevD.96.016026. arXiv: 1607.01009 [hep-ph].

[88] C. McCabe, "New constraints and discovery potential of sub-GeV dark matter with xenon detectors," *Phys. Rev.*, vol. D96, no. 4, p. 043 010, 2017. DOI: 10.1103/PhysRevD.96.043010. arXiv: 1702.04730 [hep-ph].

[89] R. Essig, J. Pérez-Ríos, H. Ramani, and O. Slone, "Direct Detection of Spin-(In)dependent Nuclear Scattering of Sub-GeV Dark Matter Using Molecular Excitations," 2019, [Phys. Rev. Research.1,033105(2019)]. DOI: 10.1103/PhysRevResearch.1.033105. arXiv: 1907.07682 [hep-ph].

[90] M. Battaglieri *et al.*, "US Cosmic Visions: New Ideas in Dark Matter 2017: Community Report," in *U.S. Cosmic Visions: New Ideas in Dark Matter College Park, MD, USA, March 23-25, 2017*, 2017. arXiv: 1707.04591 [hep-ph]. [Online]. Available: http://lss.fnal.gov/archive/2017/conf/fermilab-conf-17-282-ae-ppd-t.pdf.

[91] M. Schumann, "Direct Detection of WIMP Dark Matter: Concepts and Status," *J. Phys.*, vol. G46, no. 10, p. 103 003, 2019. DOI: 10.1088/1361-6471/ab2ea5. arXiv: 1903.03026 [astro-ph.CO].

[92] O. Abramoff *et al.*, "SENSEI: Direct-Detection Constraints on Sub-GeV Dark Matter from a Shallow Underground Run Using a Prototype Skipper-CCD," *Phys. Rev. Lett.*, vol. 122, no. 16, p. 161 801, 2019. DOI: 10.1103/PhysRevLett.122.161801. arXiv: 1901.10478 [hep-ex].

[93] N. Sabti, A. Magalich, and A. Filimonova, "An extended analysis of Heavy Neutral Leptons during Big Bang Nucleosynthesis," *in preparation for publication*, 2020.

[94] P. Gondolo and G. Gelmini, "Cosmic abundances of stable particles: Improved analysis," *Nucl. Phys.*, vol. B360, pp. 145–179, 1991. DOI: 10.1016/0550-3213(91)90438-4.

[95] M. Cannoni, "Relativistic $< \sigma v_{\rm rel} >$ in the calculation of relics abundances: a closer look," *Phys. Rev.*, vol. D89, no. 10, p. 103 533, 2014. DOI: 10.1103/PhysRevD.89.103533. arXiv: 1311.4494 [astro-ph.CO].

[96] L. G. van den Aarssen, T. Bringmann, and Y. C. Goedecke, "Thermal decoupling and the smallest subhalo mass in dark matter models with Sommerfeld-enhanced annihilation rates," *Phys. Rev. D*, vol. 85, p. 123 512, 2012. DOI: 10.1103/PhysRevD.85.123512. arXiv: 1202.5456 [hep-ph].

[97] T. Binder, T. Bringmann, M. Gustafsson, and A. Hryczuk, "Early kinetic decoupling of dark matter: when the standard way of calculating the thermal relic density fails," *Phys. Rev. D*, vol. 96, no. 11, p. 115 010, 2017. DOI: 10.1103/PhysRevD.96.115010. arXiv: 1706.07433 [astro-ph.CO].

[98] G. Steigman, B. Dasgupta, and J. F. Beacom, "Precise Relic WIMP Abundance and its Impact on Searches for Dark Matter Annihilation," *Phys. Rev.*, vol. D86, p. 023 506, 2012. DOI: 10.1103/PhysRevD.86.023506. arXiv: 1204.3622 [hep-ph].

[99] L. J. Hall, K. Jedamzik, J. March-Russell, and S. M. West, "Freeze-In Production of FIMP Dark Matter," *JHEP*, vol. 03, p. 080, 2010. DOI: 10.1007/JHEP03(2010)080. arXiv: 0911.1120 [hep-ph].

[100] V. A. Mitsou, "Overview of searches for dark matter at the LHC," vol. 651, p. 012 023, 2015. DOI: 10.1088/1742-6596/651/1/012023. [Online]. Available: https://doi.org/10.1088%2F1742-6596%2F651%2F1%2F012023.

[101] M. Escudero, A. Berlin, D. Hooper, and M.-X. Lin, "Toward (Finally!) Ruling Out Z and Higgs Mediated Dark Matter Models," *JCAP*, vol. 12, p. 029, 2016. DOI: 10.1088/1475-7516/2016/12/029. arXiv: 1609.09079 [hep-ph].

[102] A. Beniwal, F. Rajec, C. Savage, P. Scott, C. Weniger, M. White, and A. G. Williams, "Combined analysis of effective Higgs portal dark matter models," *Phys. Rev.*, vol. D93, no. 11, p. 115 016, 2016. DOI: 10.1103/PhysRevD.93.115016. arXiv: 1512.06458 [hep-ph].

[103] J. L. Feng, M. Kaplinghat, H. Tu, and H.-B. Yu, "Hidden Charged Dark Matter," *JCAP*, vol. 0907, p. 004, 2009. DOI: 10.1088/1475-7516/2009/07/004. arXiv: 0905.3039 [hep-ph].

[104] K. Griest and D. Seckel, "Three exceptions in the calculation of relic abundances," *Phys. Rev.*, vol. D43, pp. 3191–3203, 1991. DOI: 10.1103/PhysRevD.43.3191.

[105] M. Ibe, S. Matsumoto, S. Shirai, and T. T. Yanagida, "Wino Dark Matter in light of the AMS-02 2015 Data," *Phys. Rev.*, vol. D91, no. 11, p. 111 701, 2015. DOI: 10.1103/PhysRevD.91.111701. arXiv: 1504.05554 [hep-ph].

[106] M. Cirelli, T. Hambye, P. Panci, F. Sala, and M. Taoso, "Gamma ray tests of Minimal Dark Matter," *JCAP*, vol. 1510, no. 10, p. 026, 2015. DOI: 10.1088/1475-7516/2015/10/026. arXiv: 1507.05519 [hep-ph].

[107] R. T. D'Agnolo and J. T. Ruderman, "Light Dark Matter from Forbidden Channels," *Phys. Rev. Lett.*, vol. 115, no. 6, p. 061 301, 2015. DOI: 10.1103/PhysRevLett.115.061301. arXiv: 1505.07107 [hep-ph].

[108] J. L. Feng and J. Smolinsky, "Impact of a resonance on thermal targets for invisible dark photon searches," *Phys. Rev.*, vol. D96, no. 9, p. 095 022, 2017. DOI: 10.1103/PhysRevD.96.095022. arXiv: 1707.03835 [hep-ph].

[109] M. Tanabashi et al., "Review of particle physics," *Phys. Rev. D*, vol. 98, p. 030 001, 3 2018. DOI: 10.1103/PhysRevD.98.030001. [Online]. Available: https://link.aps.org/doi/10.1103/PhysRevD.98.030001.

[110] A. Filimonova and S. Westhoff, "Long live the Higgs portal!" *JHEP*, vol. 02, p. 140, 2019. DOI: 10.1007/JHEP02(2019)140. arXiv: 1812.04628 [hep-ph].

[111] R. Mahbubani and L. Senatore, "The Minimal model for dark matter and unification," *Phys. Rev.*, vol. D73, p. 043 510, 2006. DOI: 10.1103/PhysRevD.73.043510. arXiv: hep-ph/0510064 [hep-ph].

[112] A. Dedes and D. Karamitros, "Doublet-Triplet Fermionic Dark Matter," *Phys. Rev.*, vol. D89, no. 11, p. 115 002, 2014. DOI: 10.1103/PhysRevD.89.115002. arXiv: 1403.7744 [hep-ph].

[113] A. Freitas, S. Westhoff, and J. Zupan, "Integrating in the Higgs Portal to Fermion Dark Matter," *JHEP*, vol. 09, p. 015, 2015. DOI: 10.1007/JHEP09(2015)015. arXiv: 1506.04149 [hep-ph].

[114] T. M. P. Tait and Z.-H. Yu, "Triplet-Quadruplet Dark Matter," *JHEP*, vol. 03, p. 204, 2016. DOI: 10.1007/JHEP03(2016)204. arXiv: 1601.01354 [hep-ph].

[115] L. Lopez Honorez, M. H. G. Tytgat, P. Tziveloglou, and B. Zaldivar, "On Minimal Dark Matter coupled to the Higgs," *JHEP*, vol. 04, p. 011, 2018. DOI: 10.1007/JHEP04(2018)011. arXiv: 1711.08619 [hep-ph].

[116] L. Lopez-Honorez, T. Schwetz, and J. Zupan, "Higgs portal, fermionic dark matter, and a Standard Model like Higgs at 125 GeV," *Phys. Lett.*, vol. B716, pp. 179–185, 2012. DOI: 10.1016/j.physletb.2012.07.017. arXiv: 1203.2064 [hep-ph].

[117] A. Djouadi, O. Lebedev, Y. Mambrini, and J. Quevillon, "Implications of LHC searches for Higgs–portal dark matter," *Phys. Lett.*, vol. B709, pp. 65–69, 2012. DOI: 10.1016/j.physletb.2012.01.062. arXiv: 1112.3299 [hep-ph].

[118] M. Cirelli, F. Sala, and M. Taoso, "Wino-like Minimal Dark Matter and future colliders," *JHEP*, vol. 10, p. 033, 2014, [Erratum: JHEP01,041(2015)]. DOI: 10.1007/JHEP10(2014)033,10.1007/JHEP01(2015)041. arXiv: 1407.7058 [hep-ph].

[119] S. Baum, M. Carena, N. R. Shah, and C. E. M. Wagner, "Higgs portals for thermal Dark Matter. EFT perspectives and the NMSSM," *JHEP*, vol. 04, p. 069, 2018. DOI: 10.1007/JHEP04(2018)069. arXiv: 1712.09873 [hep-ph].

[120] N. Arkani-Hamed, A. Delgado, and G. F. Giudice, "The Well-tempered neutralino," *Nucl. Phys.*, vol. B741, pp. 108–130, 2006. DOI: 10.1016/j.nuclphysb.2006.02.010. arXiv: hep-ph/0601041 [hep-ph].

[121] E. Ma and D. Suematsu, "Fermion Triplet Dark Matter and Radiative Neutrino Mass," *Mod. Phys. Lett.*, vol. A24, pp. 583–589, 2009. DOI: 10.1142/S021773230903059X. arXiv: 0809.0942 [hep-ph].

[122] M. Ibe, S. Matsumoto, and R. Sato, "Mass Splitting between Charged and Neutral Winos at Two-Loop Level," *Phys. Lett.*, vol. B721, pp. 252–260, 2013. DOI: 10.1016/j.physletb.2013.03.015. arXiv: 1212.5989 [hep-ph].

[123] A. Bharucha, F. Brümmer, and N. Desai, "Next-to-minimal dark matter at the LHC," *JHEP*, vol. 11, p. 195, 2018. DOI: 10.1007/JHEP11(2018)195. arXiv: 1804.02357 [hep-ph].

[124] S. Choubey, S. Khan, M. Mitra, and S. Mondal, "Singlet-Triplet Fermionic Dark Matter and LHC Phenomenology," *Eur. Phys. J.*, vol. C78, no. 4, p. 302, 2018. DOI: 10.1140/epjc/s10052-018-5785-1. arXiv: 1711.08888 [hep-ph].

[125] J. Bramante, N. Desai, P. Fox, A. Martin, B. Ostdiek, and T. Plehn, "Towards the Final Word on Neutralino Dark Matter," *Phys. Rev.*, vol. D93, no. 6, p. 063 525, 2016. DOI: 10.1103/PhysRevD.93.063525. arXiv: 1510.03460 [hep-ph].

[126] E. Aprile *et al.*, "Dark Matter Search Results from a One Ton-Year Exposure of XENON1T," *Phys. Rev. Lett.*, vol. 121, no. 11, p. 111 302, 2018. DOI: 10.1103/PhysRevLett.121.111302. arXiv: 1805.12562 [astro-ph.CO].

[127] G. Bélanger, F. Boudjema, A. Goudelis, A. Pukhov, and B. Zaldivar, "micrOMEGAs5.0 : Freeze-in," *Comput. Phys. Commun.*, vol. 231, pp. 173–186, 2018. DOI: 10.1016/j.cpc.2018.04.027. arXiv: 1801.03509 [hep-ph].

[128] P. A. R. Ade *et al.*, "Planck 2015 results. XIII. Cosmological parameters," *Astron. Astrophys.*, vol. 594, A13, 2016. DOI: 10.1051/0004-6361/201525830. arXiv: 1502.01589 [astro-ph.CO].

[129] J. Abdallah *et al.*, "Searches for supersymmetric particles in e+ e- collisions up to 208-GeV and interpretation of the results within the MSSM," *Eur. Phys. J.*, vol. C31, pp. 421–479, 2003. DOI: 10.1140/epjc/s2003-01355-5. arXiv: hep-ex/0311019 [hep-ex].

[130] R. T. D'Agnolo, D. Pappadopulo, and J. T. Ruderman, "Fourth Exception in the Calculation of Relic Abundances," *Phys. Rev. Lett.*, vol. 119, no. 6, p. 061 102, 2017. DOI: 10.1103/PhysRevLett.119.061102. arXiv: 1705.08450 [hep-ph].

[131] M. Garny, J. Heisig, B. Lülf, and S. Vogl, "Coannihilation without chemical equilibrium," *Phys. Rev.*, vol. D96, no. 10, p. 103 521, 2017. DOI: 10.1103/PhysRevD.96.103521. arXiv: 1705.09292 [hep-ph].

[132] R. T. D'Agnolo, C. Mondino, J. T. Ruderman, and P.-J. Wang, "Exponentially Light Dark Matter from Coannihilation," *JHEP*, vol. 08, p. 079, 2018. DOI: 10.1007/JHEP08(2018)079. arXiv: 1803.02901 [hep-ph].

[133] H.-C. Cheng, L. Li, and R. Zheng, "Coscattering/Coannihilation Dark Matter in a Fraternal Twin Higgs Model," *JHEP*, vol. 09, p. 098, 2018. DOI: 10.1007/JHEP09(2018)098. arXiv: 1805.12139 [hep-ph].

[134] S. Junius, L. Lopez-Honorez, and A. Mariotti, "A feeble window on leptophilic dark matter," *JHEP*, vol. 07, p. 136, 2019. DOI: 10.1007/JHEP07(2019)136. arXiv: 1904.07513 [hep-ph].

[135] H. Kim and E. Kuflik, "Superheavy Thermal Dark Matter," *Phys. Rev. Lett.*, vol. 123, no. 19, p. 191 801, 2019. DOI: 10.1103/PhysRevLett.123.191801. arXiv: 1906.00981 [hep-ph].

[136] R. T. D'Agnolo, D. Pappadopulo, J. T. Ruderman, and P.-J. Wang, "Thermal Relic Targets with Exponentially Small Couplings," 2019. arXiv: 1906.09269 [hep-ph].

[137] M. Drees and M. M. Nojiri, "The Neutralino relic density in minimal $N = 1$ supergravity," *Phys. Rev.*, vol. D47, pp. 376–408, 1993. DOI: 10.1103/PhysRevD.47.376. arXiv: hep-ph/9207234 [hep-ph].

[138] N. Nagata, H. Otono, and S. Shirai, "Probing Bino-Wino Coannihilation at the LHC," *JHEP*, vol. 10, p. 086, 2015. DOI: 10.1007/JHEP10(2015)086. arXiv: 1506.08206 [hep-ph].

[139] M. Ibe, T. Moroi, and T. T. Yanagida, "Possible Signals of Wino LSP at the Large Hadron Collider," *Phys. Lett.*, vol. B644, pp. 355–360, 2007. DOI: 10.1016/j.physletb.2006.11.061. arXiv: hep-ph/0610277 [hep-ph].

[140] M. R. Buckley, L. Randall, and B. Shuve, "LHC Searches for Non-Chiral Weakly Charged Multiplets," *JHEP*, vol. 05, p. 097, 2011. DOI: 10.1007/JHEP05(2011)097. arXiv: 0909.4549 [hep-ph].

[141] R. Mahbubani, P. Schwaller, and J. Zurita, "Closing the window for compressed Dark Sectors with disappearing charged tracks," *JHEP*, vol. 06, p. 119, 2017, [Erratum: JHEP10,061(2017)]. DOI: 10.1007/JHEP06(2017)119,10.1007/JHEP10(2017)061. arXiv: 1703.05327 [hep-ph].

[142] M. Aaboud *et al.*, "Search for long-lived charginos based on a disappearing-track signature in pp collisions at $\sqrt{s} = 13$ TeV with the ATLAS detector," *JHEP*, vol. 06, p. 022, 2018. DOI: 10.1007/JHEP06(2018)022. arXiv: 1712.02118 [hep-ex].

[143] A. M. Sirunyan *et al.*, "Search for new physics in events with two soft oppositely charged leptons and missing transverse momentum in proton-proton collisions at $\sqrt{s} = 13$ TeV," *Phys. Lett.*, vol. B782, pp. 440–467, 2018. DOI: 10.1016/j.physletb.2018.05.062. arXiv: 1801.01846 [hep-ex].

[144] M. Aaboud *et al.*, "Search for electroweak production of supersymmetric states in scenarios with compressed mass spectra at $\sqrt{s} = 13$ TeV with the ATLAS detector," *Phys. Rev.*, vol. D97, no. 5, p. 052 010, 2018. DOI: 10.1103/PhysRevD.97.052010. arXiv: 1712.08119 [hep-ex].

[145] CMS Collaboration, "Search for displaced leptons in the e-mu channel," Aug. 2016.

[146] V. Khachatryan *et al.*, "Search for Displaced Supersymmetry in events with an electron and a muon with large impact parameters," *Phys. Rev. Lett.*, vol. 114, no. 6, p. 061 801, 2015. DOI: 10.1103/PhysRevLett.114.061801. arXiv: 1409.4789 [hep-ex].

[147] G. Aad *et al.*, "Search for massive, long-lived particles using multitrack displaced vertices or displaced lepton pairs in pp collisions at $\sqrt{s} = 8$ TeV with the ATLAS detector," *Phys. Rev. D*, vol. 92, no. 7, p. 072 004, 2015. DOI: 10.1103/PhysRevD.92.072004. arXiv: 1504.05162 [hep-ex].

[148] D. Curtin *et al.*, "Long-Lived Particles at the Energy Frontier: The MATHUSLA Physics Case," *Rept. Prog. Phys.*, vol. 82, no. 11, p. 116 201, 2019. DOI: 10.1088/1361-6633/ab28d6. arXiv: 1806.07396 [hep-ph].

[149] A. Filimonova, R. Schäfer, and S. Westhoff, "Probing dark sectors with long-lived particles at BELLE II," 2019. arXiv: 1911.03490 [hep-ph].

[150] D. O'Connell, M. J. Ramsey-Musolf, and M. B. Wise, "Minimal Extension of the Standard Model Scalar Sector," *Phys. Rev. D*, vol. 75, p. 037 701, 2007. DOI: 10.1103/PhysRevD.75.037701. arXiv: hep-ph/0611014.

[151] F. Piazza and M. Pospelov, "Sub-eV scalar dark matter through the super-renormalizable Higgs portal," *Phys. Rev. D*, vol. 82, p. 043 533, 2010. DOI: 10.1103/PhysRevD.82.043533. arXiv: 1003.2313 [hep-ph].

[152] J. A. Casas, D. G. Cerdeño, J. M. Moreno, and J. Quilis, "Reopening the Higgs portal for single scalar dark matter," *JHEP*, vol. 05, p. 036, 2017. DOI: 10.1007/JHEP05(2017)036. arXiv: 1701.08134 [hep-ph].

[153] M. Pospelov, A. Ritz, and M. B. Voloshin, "Secluded WIMP Dark Matter," *Phys. Lett. B*, vol. 662, pp. 53–61, 2008. DOI: 10.1016/j.physletb.2008.02.052. arXiv: 0711.4866 [hep-ph].

[154] J. Espinosa and M. Quiros, "The Electroweak phase transition with a singlet," *Phys. Lett. B*, vol. 305, pp. 98–105, 1993. DOI: 10.1016/0370-2693(93)91111-Y. arXiv: hep-ph/9301285.

[155] S. Profumo, M. J. Ramsey-Musolf, and G. Shaughnessy, "Singlet Higgs phenomenology and the electroweak phase transition," *JHEP*, vol. 08, p. 010, 2007. DOI: 10.1088/1126-6708/2007/08/010. arXiv: 0705.2425 [hep-ph].

[156] D. Croon, J. N. Howard, S. Ipek, and T. M. Tait, "QCD baryogenesis," *Phys. Rev. D*, vol. 101, no. 5, p. 055 042, 2020. DOI: 10.1103/PhysRevD.101.055042. arXiv: 1911.01432 [hep-ph].

[157] F. Bezrukov and D. Gorbunov, "Light inflaton Hunter's Guide," *JHEP*, vol. 05, p. 010, 2010. DOI: 10.1007/JHEP05(2010)010. arXiv: 0912.0390 [hep-ph].

[158] O. Lebedev and H. M. Lee, "Higgs Portal Inflation," *Eur. Phys. J. C*, vol. 71, p. 1821, 2011. DOI: 10.1140/epjc/s10052-011-1821-0. arXiv: 1105.2284 [hep-ph].

[159] R. R. Schäfer, "Searching for light dark sectors in rare meson decays," Master's thesis, U. Heidelberg, 2019. DOI: 10.11588/heidok.00026777. [Online]. Available: http://archiv.ub.uni-heidelberg.de/volltextserver/26777/.

[160] M. W. Winkler, "Decay and detection of a light scalar boson mixing with the Higgs boson," *Phys. Rev.*, vol. D99, no. 1, p. 015 018, 2019. DOI: 10.1103/PhysRevD.99.015018. arXiv: 1809.01876 [hep-ph].

[161] K. Bondarenko, A. Boyarsky, T. Bringmann, M. Hufnagel, K. Schmidt-Hoberg, and A. Sokolenko, "Direct detection and complementary constraints for sub-GeV dark matter," *JHEP*, vol. 03, p. 118, 2020, [JHEP20,118(2020)]. DOI: 10.1007/JHEP03(2020)118. arXiv: 1909.08632 [hep-ph].

[162] A. Bevan *et al.*, "The Physics of the B Factories," *Eur. Phys. J. C*, vol. 74, p. 3026, 2014. DOI: 10.1140/epjc/s10052-014-3026-9. arXiv: 1406.6311 [hep-ex].

[163] R. Willey and H. Yu, "Neutral Higgs Boson From Decays of Heavy Flavored Mesons," *Phys. Rev. D*, vol. 26, p. 3086, 1982. DOI: 10.1103/PhysRevD.26.3086.

[164] P. del Amo Sanchez *et al.*, "Search for the Rare Decay $B \to K\nu\bar{\nu}$," *Phys. Rev.*, vol. D82, p. 112 002, 2010. DOI: 10.1103/PhysRevD.82.112002. arXiv: 1009.1529 [hep-ex].

[165] O. Lutz *et al.*, "Search for $B \to h^{(*)}\nu\bar{\nu}$ with the full Belle $\Upsilon(4S)$ data sample," *Phys. Rev.*, vol. D87, no. 11, p. 111 103, 2013. DOI: 10.1103/PhysRevD.87.111103. arXiv: 1303.3719 [hep-ex].

[166] J. Grygier *et al.*, "Search for $\boldsymbol{B \to h\nu\bar{\nu}}$ decays with semileptonic tagging at Belle," *Phys. Rev.*, vol. D96, no. 9, p. 091 101, 2017, [Addendum: Phys. Rev.D97,no.9,099902(2018)]. DOI: 10.1103/PhysRevD.97.099902, 10.1103/PhysRevD.96.091101. arXiv: 1702.03224 [hep-ex].

[167] J. P. Lees *et al.*, "Search for $B \to K^{(*)}\nu\bar{\nu}$ and invisible quarkonium decays," *Phys. Rev.*, vol. D87, no. 11, p. 112 005, 2013. DOI: 10.1103/PhysRevD.87.112005. arXiv: 1303.7465 [hep-ex].

[168] W. Altmannshofer *et al.*, "The Belle II Physics Book," *PTEP*, vol. 2019, no. 12, E. Kou and P. Urquijo, Eds., p. 123C01, 2019, [erratum: PTEP2020,no.2,029201(2020)]. DOI: 10.1093/ptep/ptz106,10.1093/ptep/ptaa008. arXiv: 1808.10567 [hep-ex].

[169] A. V. Artamonov *et al.*, "New measurement of the $K^+ \to \pi^+\nu\bar{\nu}$ branching ratio," *Phys. Rev. Lett.*, vol. 101, p. 191 802, 2008. DOI: 10.1103/PhysRevLett.101.191802. arXiv: 0808.2459 [hep-ex].

[170] E. Cortina Gil *et al.*, "First search for $K^+ \to \pi^+\nu\bar{\nu}$ using the decay-in-flight technique," *Phys. Lett.*, vol. B791, pp. 156–166, 2019. DOI: 10.1016/j.physletb.2019.01.067. arXiv: 1811.08508 [hep-ex].

[171] N. Lurkin, "Latest results from the NA62 experiment at CERN," in *An Alpine LHC Physics Summit 2019 (ALPS 2019) Obergurgl, Austria, April 22-27, 2019*, 2019. arXiv: 1907.12955 [hep-ex].

[172] C. L. Hsu *et al.*, "Search for B^0 decays to invisible final states," *Phys. Rev.*, vol. D86, p. 032 002, 2012. DOI: 10.1103/PhysRevD.86.032002. arXiv: 1206.5948 [hep-ex].

[173] A. M. Sirunyan *et al.*, "Combined measurements of Higgs boson couplings in proton–proton collisions at $\sqrt{s} = 13\,\text{TeV}$," *Eur. Phys. J.*, vol. C79, no. 5, p. 421, 2019. DOI: 10.1140/epjc/s10052-019-6909-y. arXiv: 1809.10733 [hep-ex].

[174] M. Cepeda *et al.*, "Report from Working Group 2," *CERN Yellow Rep. Monogr.*, vol. 7, pp. 221–584, 2019. DOI: 10.23731/CYRM-2019-007.221. arXiv: 1902.00134 [hep-ph].

[175] R. Aaij *et al.*, "Search for long-lived scalar particles in $B^+ \to K^+\chi(\mu^+\mu^-)$ decays," *Phys. Rev.*, vol. D95, no. 7, p. 071 101, 2017. DOI: 10.1103/PhysRevD.95.071101. arXiv: 1612.07818 [hep-ex].

[176] R. Aaij *et al.*, "Search for hidden-sector bosons in $B^0 \to K^{*0}\mu^+\mu^-$ decays," *Phys. Rev. Lett.*, vol. 115, no. 16, p. 161 802, 2015. DOI: 10.1103/PhysRevLett.115.161802. arXiv: 1508.04094 [hep-ex].

[177] J. P. Lees *et al.*, "Search for Long-Lived Particles in e^+e^- Collisions," *Phys. Rev. Lett.*, vol. 114, no. 17, p. 171 801, 2015. DOI: 10.1103/PhysRevLett.114.171801. arXiv: 1502.02580 [hep-ex].

[178] R Aaij *et al.*, "Differential branching fraction and angular analysis of the $B^+ \to K^+\mu^+\mu^-$ decay," *JHEP*, vol. 02, p. 105, 2013. DOI: 10.1007/JHEP02(2013)105. arXiv: 1209.4284 [hep-ex].

[179] I. Boiarska, K. Bondarenko, A. Boyarsky, V. Gorkavenko, M. Ovchynnikov, and A. Sokolenko, "Phenomenology of GeV-scale scalar portal," *JHEP*, vol. 11, p. 162, 2019. DOI: 10.1007/JHEP11(2019)162. arXiv: 1904.10447 [hep-ph].

[180] J. A. Bailey *et al.*, "$B \to Kl^+l^-$ Decay Form Factors from Three-Flavor Lattice QCD," *Phys. Rev.*, vol. D93, no. 2, p. 025 026, 2016. DOI: 10.1103/PhysRevD.93.025026. arXiv: 1509.06235 [hep-lat].

[181] J. F. Kamenik and C. Smith, "FCNC portals to the dark sector," *JHEP*, vol. 03, p. 090, 2012. DOI: 10.1007/JHEP03(2012)090. arXiv: 1111.6402 [hep-ph].

[182] N. Gubernari, A. Kokulu, and D. van Dyk, "$B \to P$ and $B \to V$ Form Factors from B-Meson Light-Cone Sum Rules beyond Leading Twist," *JHEP*, vol. 01, p. 150, 2019. DOI: 10.1007/JHEP01(2019)150. arXiv: 1811.00983 [hep-ph].

[183] G. Lanfranchi, "Search for Hidden Sector particles at NA62," *PoS*, vol. EPS-HEP2017, p. 301, 2017. DOI: 10.22323/1.314.0301.

[184] A. Ariga *et al.*, "FASER's physics reach for long-lived particles," *Phys. Rev.*, vol. D99, no. 9, p. 095 011, 2019. DOI: 10.1103/PhysRevD.99.095011. arXiv: 1811.12522 [hep-ph].

[185] J. L. Feng, I. Galon, F. Kling, and S. Trojanowski, "Dark Higgs bosons at the ForwArd Search ExpeRiment," *Phys. Rev.*, vol. D97, no. 5, p. 055 034, 2018. DOI: 10.1103/PhysRevD.97.055034. arXiv: 1710.09387 [hep-ph].

[186] S. Alekhin *et al.*, "A facility to Search for Hidden Particles at the CERN SPS: the SHiP physics case," *Rept. Prog. Phys.*, vol. 79, no. 12, p. 124 201, 2016. DOI: 10.1088/0034-4885/79/12/124201. arXiv: 1504.04855 [hep-ph].

[187] V. V. Gligorov, S. Knapen, M. Papucci, and D. J. Robinson, "Searching for Long-lived Particles: A Compact Detector for Exotics at LHCb," *Phys. Rev.*, vol. D97, no. 1, p. 015 023, 2018. DOI: 10.1103/PhysRevD.97.015023. arXiv: 1708.09395 [hep-ph].

[188] J. A. Evans, "Detecting Hidden Particles with MATHUSLA," *Phys. Rev.*, vol. D97, no. 5, p. 055 046, 2018. DOI: 10.1103/PhysRevD.97.055046. arXiv: 1708.08503 [hep-ph].

[189] A. Fradette and M. Pospelov, "BBN for the LHC: constraints on lifetimes of the Higgs portal scalars," *Phys. Rev. D*, vol. 96, no. 7, p. 075 033, 2017. DOI: 10.1103/PhysRevD.96.075033. arXiv: 1706.01920 [hep-ph].

[190] G. Krnjaic, "Probing Light Thermal Dark-Matter With a Higgs Portal Mediator," *Phys. Rev. D*, vol. 94, no. 7, p. 073 009, 2016. DOI: 10.1103/PhysRevD.94.073009. arXiv: 1512.04119 [hep-ph].

[191] S. Choi, H. Haber, J. Kalinowski, and P. Zerwas, "The Neutralino sector in the U(1)-extended supersymmetric standard model," *Nucl. Phys. B*, vol. 778, pp. 85–128, 2007. DOI: 10.1016/j.nuclphysb.2007.04.019. arXiv: hep-ph/0612218.

[192] H. E. Haber, "A tale of three diagonalizations," 2019.

[193] V. Beylin, V. Kuksa, R. Pasechnik, and G. Vereshkov, "Diagonalization of the neutralino mass matrix and boson-neutralino interaction," *Eur. Phys. J. C*, vol. 56, pp. 395–405, 2008. DOI: 10.1140/epjc/s10052-008-0660-0. arXiv: hep-ph/0702148.

[194] A. Djouadi, Y. Mambrini, and M. Muhlleitner, "Chargino and neutralino decays revisited," *Eur. Phys. J. C*, vol. 20, pp. 563–584, 2001. DOI: 10.1007/s100520100679. arXiv: hep-ph/0104115.

[195] R. Aaij *et al.*, "Search for violations of Lorentz invariance and CPT symmetry in $B^0_{(s)}$ mixing," *Phys. Rev. Lett.*, vol. 116, no. 24, p. 241 601, 2016. DOI: 10.1103/PhysRevLett.116.241601. arXiv: 1603.04804 [hep-ex].

A. Technical aspects of the singlet-triplet model

This appendix is devoted to clarification of some technical details of the singlet-triplet model that is the focus of Chapter 4.

A.1. The singlet-triplet model in four-component notation

In this section, we would like to provide the Lagrangians of Chapter 4 in the four-component notation. Let us now focus on the scalar scenario and introduce the four-component Dirac spinors as

$$\psi_0 = \chi_0 + (\chi_0)^c, \quad \psi_T^+ = \chi_T^+ + (\chi_T^+)^c, \tag{A.1}$$

where χ_0 is the neutral singlet or triplet. The kinetic terms in Lagrangian in Equation (4.2) can written down as

$$\begin{aligned}\mathcal{L}_{\text{kin}} =& \overline{\chi}_S i\partial\!\!\!/ \chi_S + \text{Tr}[\overline{\chi}_T i D\!\!\!/ \chi_T] \\ =& \overline{\chi}_S i\partial\!\!\!/ \chi_S + \overline{\chi_T^+} i\partial\!\!\!/ \chi_T^+ \overline{\chi_T^-} i\partial\!\!\!/ \chi_T^- + \overline{\chi_T^0} i\partial\!\!\!/ \chi_T^0 \\ &+ g(\overline{\chi_T^0} W\!\!\!/^+ \chi_T^- - \overline{\chi_T^+} W\!\!\!/^+ \chi_T^0 + \overline{\chi_T^-} W\!\!\!/^- \chi_T^0 - \overline{\chi_T^0} W\!\!\!/^- \chi_T^+) \\ &+ g(\overline{\chi_T^+}[\cos\theta_w Z\!\!\!/ - \sin\theta_w A\!\!\!/]\, \chi_T^+ - \overline{\chi_T^-}[\cos\theta_w Z\!\!\!/ - \sin\theta_w A\!\!\!/]\chi_T^-),\end{aligned} \tag{A.2}$$

where θ_w is the Weinberg $V\!\!\!/ = V_\mu \gamma^\mu$ for any vector boson V. In the four-component notations, the kinetic Lagrangian reads

$$\begin{aligned}\mathcal{L}_{\text{kin}} =& \frac{1}{2}\overline{\psi}_S i\partial\!\!\!/ \psi_S + \overline{\psi_T^+} i\partial\!\!\!/ \psi_T^+ + \frac{1}{2}\overline{\psi_T^0} i\partial\!\!\!/ \psi_T^0 \\ &- g(\overline{\psi_T^0} W\!\!\!/^- \psi_T^+ - \overline{\psi_T^+} W\!\!\!/^+ \psi_T^0 + \overline{\psi_T^+}[\cos\theta_w Z\!\!\!/ - \sin\theta_w A\!\!\!/]\psi_T^+),\end{aligned} \tag{A.3}$$

where for the W-containing term we used the following relations

$$g(\overline{\chi_T^0} W\!\!\!/^+ \chi_T^- - \overline{\chi_T^+} W\!\!\!/^+ \chi_T^0) = g(-\overline{\psi_T^+} W\!\!\!/^+ P_R\, \psi_T^0 - \overline{\psi_T^+} W\!\!\!/^+ P_L\, \psi_T^0) = -g\, \overline{\psi_T^+} W\!\!\!/^+ \psi_T^0 \tag{A.4}$$

with $P_{R/L} = (1 \pm \gamma_5)/2$ being the chiral projectors.

The scalar Lagrangian in Equation (4.5) after the EWSB can be expressed as (dropping

the h^2-containing terms and again setting $\kappa_S = \kappa_T = \kappa'_T = 0$)

$$\begin{aligned}\mathcal{L}_{\rm S} =& -\frac{m_S}{2}\overline{\chi}_S(\chi_S)^c - \frac{m_T}{2}\overline{\chi^0_T}(\chi^0_T)^c - \frac{\mu}{2}\Big(1+\frac{2h}{v}\Big)\Big[\overline{\chi^0_T}(\chi_S)^c + \overline{\chi}_S(\chi^0_T)^c\Big] + h.c. \\ =& -\frac{m_S}{2}\overline{\psi}_S\psi_S - \frac{\mu}{2}\Big(1+\frac{2h}{v}\Big)\Big[\overline{\psi^0_T}\psi_S + \overline{\psi}_S\psi^0_T\Big].\end{aligned} \tag{A.5}$$

In the above, we simplified the notations using $\chi^0_S = \chi_S$ and $\psi^0_S = \psi_S$. The transition to the mass basis is done in the similar manner as in Equation (4.5):

$$\begin{pmatrix}\chi_\ell \\ \chi_h\end{pmatrix} = \begin{pmatrix}\cos\theta\,\psi^0_S - \sin\theta\,\psi^0_T \\ \sin\theta\,\psi^0_S + \cos\theta\,\psi^0_T\end{pmatrix}, \quad \tan(2\theta) = \frac{2\mu}{m_T - m_S}, \quad 0 < \theta < \frac{\pi}{4}. \tag{A.6}$$

Correspondingly, the Lagrangian in Equation (4.9) in the new notation reads

$$\begin{aligned}\widehat{\mathcal{L}}_S =& -\frac{m_\ell}{2}\,\overline{\psi}_\ell\psi_\ell - \frac{m_h}{2}\,\overline{\psi}_h\psi_h \\ & -\frac{\mu}{v}h\Big[\cos(2\theta)\big(\overline{\psi}_\ell\psi_h + \overline{\psi}_h\psi_\ell\big) + \sin(2\theta)\big(-\overline{\psi}_\ell\psi_\ell + \overline{\psi}_h\psi_h\big)\Big] \\ & + g\,W^+_\mu\Big[\sin\theta\,\overline{\psi^+}\gamma^\mu\psi_\ell - \cos\theta\,\overline{\psi^+}\gamma^\mu\psi_h\Big] + h.c. \\ & + g\,(\cos\theta_w Z_\mu - \sin\theta_w A_\mu)\,\overline{\psi^+}\gamma^\mu\psi^+.\end{aligned} \tag{A.7}$$

In the pseudoscalar scenario, the expressions look exactly the same, accounting for the factors $i\gamma_5$.

A.2. The Autonne-Takagi diagonalization of the fermion mass matrix

The goal of this section is in providing some more details about the diagonalization procedure of the singlet-triplet mass matrix in Chapter 4. Let us fist discuss the general case of a 2×2 complex symmetric mass matrix

$$M = \begin{pmatrix}a & c \\ c & b\end{pmatrix}. \tag{A.8}$$

We will assume that none of a, b, c is zero and that $b > a$. We can diagonalize M by a unitary matrix U, such that

$$U^{-1}MU = \begin{pmatrix}\lambda_1 & 0 \\ 0 & \lambda_2\end{pmatrix}. \tag{A.9}$$

with $m_{1/2}$ being real nonnegative eigenvalues $0 \le m_1 \le m_2$ defined as

$$m^2_{1/2} = \frac{1}{2}\Big[|a|^2 + |b|^2 + 2|c|^2 \mp \sqrt{(|a|^2 + |b|^2 + 2|c|^2)^2 - 4|ab - c^2|}\Big]. \tag{A.10}$$

It can be shown [191, 192] that the matrix U is of the form

$$U = \begin{pmatrix} \cos\theta & e^{i\phi}\sin\theta \\ -e^{-i\phi}\sin\theta & \cos\theta \end{pmatrix} \begin{pmatrix} e^{-i\alpha} & 0 \\ 0 & e^{-i\beta} \end{pmatrix}, \quad \tan 2\theta = \frac{2|a^*c + bc^*|}{|b|^2 - |a|^2}, \tag{A.11}$$

where $0 \leq \theta \leq \pi/4$ and $0 \leq \alpha, \beta, \phi \leq 2\pi$. The complex phases of the second matrix are defined as

$$\alpha = \frac{1}{2}\arg a(|b|^2 - m_1^2) - b^*c^2, \tag{A.12}$$

$$\beta = \frac{1}{2}\arg b(m_2^2 - |a|^2) - a^*c^2. \tag{A.13}$$

In our model, these phases are zero in both scenarios. the remaining phase reads

$$e^{i\phi} = \epsilon\frac{a^*c + bc^*}{|a^*c + bc^*|}, \tag{A.14}$$

where $\epsilon = -1$ in our case. Let us now identify the form of the matrix U in the scalar and the pseudoscalar scenario in our singlet-triplet model. Relating the corresponding mass matrices with Equation (A.8) can be easily done in the chiral four-component notations used in Chapter 4[1].

In the scalar case, the mass matrix is

$$M_{\mathrm{S}} = \begin{pmatrix} m_S & \mu \\ \mu & m_T \end{pmatrix}, \tag{A.15}$$

the corresponding diagonalization matrix results in $\phi = \pi$ (see also Equation (4.7)).

In the pseudoscalar scenario, the off-diagonal terms of the mass matrix become complex. From Equation (4.11), we find that[2]

$$M_{\mathrm{P}} = \begin{pmatrix} -m_S & i\mu \\ i\mu & m_T \end{pmatrix}, \tag{A.16}$$

so that the complex phase is $\phi = \pi/2$ (see also Equation (4.12)).

[1] Alternatively, working in the two-component notations would be also convenient.

[2] The γ_5 martix in Equation (4.11) results in the relative minus sign between the terms containing the fields of the opposite chiralities.

B. Full decay rates of heavy fermions in singlet-triplet model

In this appendix, we provide the full expressions for the decay widths used in Section 4.5. With the correct coupling mapping that we derive in [110], they are also directly applicable to the wino-bino scenario in SUSY. Slight corrections to the corresponding isospin structure allow us to use them for general fermion multiplet decay rates through the same currents (see an example for the two-body decays in [123]). The definitions of the partial/full rates are taken from [109].

B.1. Two-body decay rates

Let us first consider the process $\chi^+ \to \chi_h \pi^+$. The decay rate of the charged mediator is defined as

$$\Gamma_{\chi_+ \to \chi_h \pi_+} = 4\pi \frac{1}{32\pi^2} \frac{|\mathbf{p}_\pi|}{m_c^2} |\bar{\mathcal{M}}_\pi^2|, \tag{B.1}$$

where $\mathbf{p}_\pi$ is the pion three-momenta vector and $\mathcal{M}$ is the matrix element of the considered process. The latter is the same in the scalar and the pseudoscalar scenarios and reads (see Lagrangian in Equation (4.9))

$$\mathcal{M}_\pi = g \cos\theta \left[\bar{U}_h \gamma^\mu U_c\right] \frac{g_{\mu\nu} - q_\mu q_\nu / m_W^2}{q^2 - m_W^2} g \frac{f_\pi V_{ud}}{2\sqrt{2}} p_\pi^\nu. \tag{B.2}$$

where U_i stand for the spinor of particle i[1], $f_\pi \simeq 130$ MeV is the pion decay constant, p_π is the momentum of pion and $q^\mu = p_c^\mu - p_h^\mu = p_\pi^\mu$ is the momentum transfer (p_c^μ and p_h^μ are the momenta of χ_c and χ_h). After applying the energy-momentum conservation laws, the decay rate (B.1) bacomes

$$\Gamma_{\chi_+ \to \chi_h \pi_+} = \frac{G_F^2 f_\pi^2}{2\pi m_c^2} |V_{ud}|^2 \cos^2\theta (m_c - m_h)^2 ((m_c + m_h)^2 - m_\pi^2) \times \left(\frac{(m_c^2 + m_\pi^2 - m_h^2)^2}{4 m_c^2} - m_\pi^2 \right)^{1/2}. \tag{B.3}$$

[1] Spinors V_i correspond to antiparticles.

In the limit $m_h - m_h \gg m_\pi$, $m_c + m_h \gg m_\pi$ and $m_c - m_h \ll m_c$ (such that $m_c + m_h \simeq 2m_c$), the expression under the square root can be approximated as

$$\left(\frac{(m_c+m_h)(m_c-m_h)}{2m_c} + \frac{m_\pi^2}{2m_c}\right)^2 - m_\pi^2 \simeq \Delta m_{ch}^2 - m_\pi^2. \tag{B.4}$$

where $\Delta m_{ch} = m_c - m_h$. Plugging this into Equation (B.3), we obtain the expression widely used in literature (see, e.g. [123, 141]),

$$\Gamma_{\chi_+ \to \chi_h \pi_+} = \frac{G_F^2 f_\pi^2}{2\pi m_c^2} |V_{ud}|^2 \cos^2\theta \Delta m_{ch}^2 (m_c + m_h)^2 \tag{B.5}$$

$$\times \left(1 - \frac{m_\pi^2}{(m_c+m_h)^2}\right) \Delta m_{ch} \left(1 - \frac{m_\pi^2}{(\Delta m_{ch})^2}\right)^{1/2} \tag{B.6}$$

$$= \frac{2G_F^2}{\pi} |V_{ud}|^2 f_\pi^2 \cos^2\theta |\Delta m_{ch}|^3 \left(1 - \frac{m_\pi^2}{(\Delta m_{ch})^2}\right)^{1/2}.$$

B.2. Three-body decay rates

Since in our model three-body decay rates differ in the scalar and pseudoscalar cases, we provide here calculations for a general case. The all the expressions below, the scalar (pseudoscalar) scenario is obtained for $a_f = 0$, $v_f = 1$ ($v_f = 0$, $a_f = 1$).

B.2.1. Vector mediated leptonic decays: $\chi_+ \to \chi_\ell l^+ \nu_l$

Here we consider leptonic decays of the charged state χ^+ via $\chi_+ \to \chi_\ell W_+^*$, $W_+^* \to l^+ \nu_l$. The corresponding matrix element reads

$$\mathcal{M}_{lept} = \left[\bar{U}_\ell G_W (v_f \gamma_\mu + a_f i \gamma_\mu \gamma_5) U_c\right] \frac{g^{\mu\nu} - q^\mu q^\nu / m_W^2}{m_W^2} G_e \left[\bar{U}_\nu \gamma_\nu V_L\right], \tag{B.7}$$

where $G_W = g \sin\theta$ and $G_e = g/\sqrt{2}$; $U_{\ell/c/\nu}$ and V_L are the spinors of $\chi_{\ell/c}$, the neutrino and the charged lepton correspondingly; $q^\mu = p_c^\mu - p_\ell^\mu - p_\nu^\mu - p_L^\mu$ where p_ℓ^μ, p_ν^μ and p_L^μ are the momenta of χ_ℓ, the neutrino and the charged lepton correspondingly.

Differential rate

The averaged over the spin states of χ_c differential decay rate of the considered process is thus

$$\frac{d\Gamma_{\chi_+ \to \chi_\ell l_+ \nu_l}}{dE_l dE_\nu} = \frac{1}{(2\pi)^3 8 m_c} |\bar{\mathcal{M}}_{\text{lept}}^2| \tag{B.8}$$

$$= \frac{1}{(2\pi)^3 8 m_c} \frac{G_l^2 G_W^2}{m_W^4} ((a_f^2 + v_f^2)(p_c\ p_\nu)(p_e\ p_l)$$

$$+ (a_f^2 + v_f^2)(p_c\ p_e)(p_l\ p_\nu) + m_c m_\ell (a_f^2 - v_f^2)(p_e\ p_\nu)).$$

Using the kinematic relations and neglecting the lepton mass, we obtain

$$\begin{aligned}\frac{d\Gamma_{\chi_+\to\chi_\ell l_+\nu_l}}{dE_l dE_\nu} = &-\frac{1}{16\pi^3 m_W^4} G_e^2 G_W^2 (a_f + v_f)(a_f(m_c(2(E_e^2 + E_\nu^2) \\ &- m_c(E_e + E_\nu)) + m_c m_\ell (m_c - 2(E_e + E_\nu)) \\ &+ m_\ell^2 (E_e + E_\nu) - m_\ell^3) + v_f(2E_e^2 m_c \\ &+ E_e(-m_c^2 + 2m_c m_\ell + m_\ell^2) + (E_\nu + m_\ell)(2E_\nu m_c - m_c^2 + m_\ell^2))).\end{aligned} \tag{B.9}$$

As discussed in Chapter 4, the rates in the scalar and the pseudoscalar scenarios are related by the sign flip of the χ_ℓ mass,

$$d\Gamma_{\chi_+\to\chi_\ell l_+\nu_l}(a_f = 0, v_f = 1) = d\Gamma_{\chi_+\to\chi_\ell l_+\nu_l}(v_f = 0, a_f = 1, m_\ell \to -m_\ell). \tag{B.10}$$

This is a general feature of vector (pseudo-vector) and scalar (pseudoscalar) interactions (see, e.g. [193]).

Integrated rate Let us now perform the integration of the Equation (B.9) using the limits from Equation (3.15) in [194],

$$\begin{aligned} 0 < &E_\nu < \frac{m_c}{2} - \frac{m_\ell^2}{2m_c}, \\ \frac{m_c}{2} - E_\nu - \frac{m_\ell^2}{2m_c} < &E_e < \frac{m_c}{2} - \frac{m_\ell^2}{2(m_c - 2E_\nu)}, \end{aligned} \tag{B.11}$$

where E_ν is the neutrino energy. The integrated rate then reads

$$\begin{aligned}\Gamma_{\chi_+\to\chi_\ell l_+\nu_l} = &\frac{G_e^2 G_W^2 (a_f + v_f)}{768\pi^3 m_c^3 m_W^4}[12 m_c^3 m_\ell^3 \log(m_\ell^2/m_c^2) \\ &\times (a_f(m_c^2 - m_c m_\ell + m_\ell^2) - v_f(m_c^2 + m_c m_\ell + m_\ell^2)) \\ &+ (m_c^2 - m_\ell^2)(a_f(m_c^6 + 2m_c^5 m_\ell - 7m_c^4 m_\ell^2 + 20 m_c^3 m_\ell^3 \\ &- 7m_c^2 m_\ell^4 + 2m_c m_\ell^5 + m_\ell^6) + v_f(m_c^6 - 2m_c^5 m_\ell - 7m_c^4 m_\ell^2 \\ &- 20 m_c^3 m_\ell^3 - 7m_c^2 m_\ell^4 - 2m_c m_\ell^5 + m_\ell^6))]\end{aligned} \tag{B.12}$$

and the scalar-pseudoscalar relation as in Equation (B.10) holds.

Limit $\Delta m_{cl} \ll m_c$

Equation (B.12) is quite cumbersome so let us look at the limit $\Delta m_{cl} = m_c - m_\ell \ll m_c$ in the scalar (S) and pseudoscalar (P) cases separately,

$$\begin{aligned}\Gamma^{\text{approx, S}}_{\chi_+\to\chi_\ell l_+\nu_l} &= \frac{G_e^2 G_W^2 \Delta m_{cl}^5}{120 m_W^4 \pi^3} = \frac{2G_F^2}{15\pi^3}\sin^2\theta(\Delta m_{c\ell})^5, \\ \Gamma^{\text{approx, P}}_{\chi_+\to\chi_\ell l_+\nu_l} &= \frac{G_e^2 G_W^2 \Delta M_{cl}^5}{40 m_W^4 \pi^3} = \frac{2G_F^2}{5\pi^3}\sin^2\theta(\Delta m_{c\ell})^5,\end{aligned} \tag{B.13}$$

where we used the explicit form of $G_{e/W}$. The latter expressions we provided in Equation (4.29).

B.2.2. Scalar mediated leptonic decays: $\chi_h \to \chi_\ell b\bar{b}$

Here we consider leptonic decays of the heavy neutral state χ_h via $\chi_h \to \chi_\ell h^*,\ h^* \to b\bar{b}$. The corresponding matrix element is

$$\mathcal{M}_b = \left[\bar{U}_\ell G_H (v_f + a_f i\gamma_5) U_h\right] \frac{1}{q^2 - M_H^2} \left[\bar{U}_b G_b V_b\right], \tag{B.14}$$

where $G_H = \mu \cos 2\theta / v$, $G_b = g\ m_b/2m_W$ (m_b is the b quark mass), $q^\mu = p_h^\mu - p_\ell^\mu - p_b^\mu - p_{\bar{b}}^\mu$ with p_b^μ and $p_{\bar{b}}^\mu$ being the momenta of the b and $\bar{b}$ quarks. Indices h, H correspond to the heavy neutral state and the Higgs boson. The differential decay rate of this process reads

$$\begin{aligned}\frac{d\Gamma_{\chi_h \to \chi_\ell b\bar{b}}}{dE_l dE_\nu} = \frac{N_c}{(2\pi)^3 8 m_c} |\bar{\mathcal{M}}_b^2| = \frac{N_c}{(2\pi)^3 8 m_c} \frac{G_b^2 G_H^2}{M_H^4} (m_b^2 - p_b p_{\bar{b}}) \\ \times \left(m_h m_\ell (a_f^2 - v_f^2) - (a_f^2 + v_f^2)\left(p_l \left(p_b + p_{\bar{b}} + p_l\right)\right)\right),\end{aligned} \tag{B.15}$$

where $N_c = 3$ is the color factor. Applying the energy-momentum conservation laws, we obtain

$$\begin{aligned}\frac{d\Gamma_{\chi_h \to \chi_\ell b\bar{b}}}{dE_b dE_{\bar{b}}} = \frac{N_c G_b^2 G_H^2}{16\pi^3 M_H^4} (m_h (m_h - 2(E_b + E_{\bar{b}})) + 4m_b^2 - m_\ell^2) \\ \times (a_f^2 (E_b + E_{\bar{b}} - m_h + m_\ell) + v_f^2 (E_b + E_{\bar{b}} - m_h - m_\ell)).\end{aligned} \tag{B.16}$$

Integrated rate

In the approximation of zero b quark mass, the integration limits of Equation (B.16) read [194]

$$\begin{aligned} 0 < E_b < \frac{m_h}{2} - \frac{m_\ell^2}{2m_h}, \\ \frac{m_h}{2} - E_b - \frac{m_\ell^2}{2m_h} < E_{\bar{b}} < \frac{m_h}{2} - \frac{m_\ell^2}{2(m_h - 2E_b)}, \end{aligned} \tag{B.17}$$

where $E_{b/\bar{b}}$ are the energies of b and $\bar{b}$ quarks. The integrated rate of the Higgs-mediated process then reads

$$\begin{aligned}\Gamma_{\chi_h\to\chi_\ell b\bar{b}} = \frac{N_c G_b^2 G_H^2}{1536\pi^3 m_h^3 M_H^4}[&(m_h^2-m_\ell^2)(a_f^2(m_h^6-4m_h^5m_\ell-7m_h^4m_\ell^2 \\ &-40m_h^3m_\ell^3-7m_h^2m_\ell^4-4m_hm_\ell^5+m_\ell^6)+v_f^2(m_h^6+4m_h^5m_\ell \\ &-7m_h^4m_\ell^2+40m_h^3m_\ell^3-7m_h^2m_\ell^4+4m_hm_\ell^5+m_\ell^6)) \\ &-12m_h^3m_\ell^3\log(m_\ell^2/m_h^2)(a_f^2(2m_h^2+m_hm_\ell+2m_\ell^2) \\ &+v_f^2(-2m_h^2+m_hm_\ell-2m_\ell^2))].\end{aligned} \tag{B.18}$$

Limit $\Delta m_{hl} \ll m_h$

As for the W-mediated rate, let us look at Equation (B.18) in the limit $\Delta m_{hl} = m_h - m_\ell \ll m_h$ in scalar and pseudoscalar cases separately,

$$\begin{aligned}\Gamma^{\text{approx, S}}_{\chi_h\to\chi_\ell b\bar{b}} &= N_c\frac{G_b^2G_H^2\Delta m_{hl}^5}{60\pi^3M_H^4} = \frac{G_F}{10\sqrt{2}\pi^3}\frac{m_b^2}{M_H^4}\left(\frac{\mu}{v}\right)^2\cos^2(2\theta)(\Delta m_{h\ell})^5, \\ \Gamma^{\text{approx, P}}_{\chi_h\to\chi_\ell b\bar{b}} &= N_c\frac{G_b^2G_H^2\Delta m_{hl}^7}{560\pi^3M_H^4} = \frac{3G_F}{280\sqrt{2}\pi^3}\frac{m_b^2}{M_H^4}\left(\frac{\mu}{v}\right)^2\cos^2(2\theta)\frac{(\Delta m_{h\ell})^7}{m_h^2}.\end{aligned} \tag{B.19}$$

where we plugged in the explicit form of $G_{b/H}$ and N_c. The latter expressions we used in Equation (4.28)[2].

Finally, we would like to note the agreement of the expressions for the partial differential rates $d\Gamma_{\chi_+\to\chi_\ell l_+\nu_l}/(dE_l dE_\nu)$ and $d\Gamma_{\chi_h\to\chi_\ell b\bar{b}}/(dE_l dE_\nu)$ with [194] where the same processes were studied in the context of SUSY.

[2] As expected, the scalar-pseudoscalar relation holds for this decay mode as well.

C. High-luminosity LHCb projections for dark scalars

In this appendix, we describe the approach used to draw the projection of the LHCb performance in searching for $B^+ \to K^+ S(\to \mu\bar{\mu})$ in the high-luminosity phase (see Chapter 5). Here we follow the logic of [161] and base our estimates on the existing LHCb search [175] that was performed for the same decay channel at $\sqrt{s} = 7$ and 8 TeV and $\mathcal{L} = 3/\text{fb}$.

The reach of the considered search in the HL phase is mostly due to the increased number of B mesons which can be estimated as [161]

$$\mathcal{R} = \frac{\mathcal{L}_{HL}\ \sigma_{13}}{\mathcal{L}_0\ \sigma_8}, \tag{C.1}$$

where $\mathcal{L}_0 = 3/\text{fb}$ is the luminocity used in the analysis [175], $\mathcal{L}_{13} = 300/\text{fb}$ is the estimated LHCb luminocity at the HL phase and $\sigma_{8/13}$ is the cross-section of the B^+ production in the direction of the LHCb detector.

In the analysis [175], the decay products of B mesons are detected in three search regions, depending on the dimuon lifetime:

1. A prompt region, $\tau_B < 1$ ps.
2. An intermediate region, 1 ps $< \tau_B <$ 10 ps.
3. A displaced region, $\tau_B > 10$ ps.

The first two signal regions are expected to have large and moderate number of background events correspondingly, the third region is almost background-free. We therefore consider two ranges of the scalar's lifetime and make the following assumptions:

1. $\tau_B < 10$ ps – background-only hypothesis.
2. $\tau_B > 10$ ps – zero background hypothesis.

In the first case, we can estimate the significance of a search as

$$s_{\text{prompt}} \sim \frac{n_s}{\sqrt{n_b}} \propto \frac{\theta^2}{n_b}, \tag{C.2}$$

where $n_{s/b}$ is the number of signal/background events. In the expression above, we used the explicit scaling of n_s with the scalar mixing angle (see Chapter 5). Requiring the same

significance from the new search, we obtain the sensitivity of the future search to mixing angles down to

$$\theta_{HL}^2 = \frac{\theta_0^2}{\sqrt{R}}, \tag{C.3}$$

where θ_0 is the smallest mixing angle the current search is sensitive. In the above, we assumed the number of background events to increase by $\mathcal{R}$ in the HL phase.

In the second case, we expect no background events. The search significance in this region can be estimated as

$$s_{\text{displaced}} \sim \sqrt{n_s} \propto \theta^2 P_d(\theta), \tag{C.4}$$

where $P_d(\theta)$ denotes the probability of the scalar to decay within the detectable volume,

$$P_d(\theta) = e^{-l_{\text{min}}/d_S} - e^{-l_{\text{max}}/d_S}. \tag{C.5}$$

Here d_S is the decay length of the scalar in the lab frame, in our calculations we set the average boost factor of a B meson at LHCb to $\langle \gamma_B \beta_B \rangle \approx 20$ [195]. The minimum and maximum distance at which displaced objects are detected are $l_{\text{min}} = 0.02$ cm, $l_{\text{max}} = 60$ cm [175], where the former is defined by the secondary vertex resolution. Requiring the same significance for the HL search results in

$$\theta_{\text{HL}}^2 P_d(\theta_{\text{HL}}) = \frac{1}{R}\theta_0^2 P_d(\theta_0), \tag{C.6}$$

where the factor R originates from the event number scaling. The resulting bound, shown in Figures 5.3 and 5.7, is obtained by checking the lifetime and applying the corresponding scaling for each scalar's mass point.